Novel Fluorescence Tools for the Discovery of Cardiac Calcium Pump Therapeutics

A Dissertation
SUBMITTED TO THE FACULTY OF
UNIVERSITY OF MINNESOTA
BY

Tory M. Schaaf

IN PARTIAL FULFILLMENT OF THE REQUIREMENTS
FOR THE DEGREE OF
DOCTOR OF PHILOSOPHY

Dr. David D. Thomas

February 2017

Acknowledgements

I was granted an incredible opportunity to pursue my graduate studies in the large and collaborative DDT lab. **Dr. David D. Thomas** is an amazing mentor and I would not be where I am today without his guidance and coaching. He always goes out of his way to make sure that I am challenging myself and using my time effectively. I've learned more than I imagined I would as graduate student because of his commitment to providing an excellent graduate education. I've never met anyone who works as hard as he does. Every day in the Thomas lab is adventure and I am incredibly grateful he is always there to guide me through it.

Simon Gruber brought me into the Thomas lab and showed me the lay of the land. I am very thankful for his support during my first years. He gave me great opportunity to be successful during my own thesis work due to him being a great example of a highly successful and productive senior grad student. My graduation was also driven by my thesis committee, which consisted of a heavyweight team of scientists **John Lipscomb**, **Do-Hyung Kim**, **James Ervasti**, and **R. Scott McIvor**. I would especially like to thank Scott McIvor who encouraged me to start this journey and apply to graduate school.

I am thankful for the opportunity to work with all the talented scientists in the Thomas lab. **Razvan Cornea** offered wisdom and insights about the lab and helped me along my way. **Joe Muretta** became a great mentor and was always willing to explore new ideas. Joe doesn't give up on an idea or a person because it may be tough, instead he sees it as a great exploration. I am thankful to work with **Robyn Rebbeck,** who is a rare type

of post doc with passion for her work. She is incredibly talented, which is seen through her hard work and continuous strive for excellence. **Mike Autry** has given me tremendous insights and knowledge especially when my experiments would not work out the way I had expected. He looks at problems from every angle and has motivated me to try harder. I would also like to show my gratitude to **Christine Karim**, **Ji Li**, **Karl Petersen**, **Jesse McCaffrey**, **Zach James**, **Ben Binder**, **Brett Colson**, **Naa-Adjeley Ablohr**, **Daphene Dong**, **John Lee**, **Bengt Svensson,** and **Rebecca Moen**. It was so much fun to interact with this team of scientists.

I also want to thank the DDT lab members that personally helped me along the way. I want to thank **Samantha Yuen** for being a talented scientist who was always willing to trouble shoot. I appreciate **Prachi Bawaskar's** industrial nature and ability to integrate ideas amongst the team. Prachi and Sam's support and encouragement were necessary to my success. **Chih-Hung Lo's** drive and enthusiasm for science raised my spirits on numerous occasions and made grad school enjoyable. I thank **Dan Stroik** for the many brainstorming sessions and willingness to explore new ideas with me. I appreciate **John Rohde's** keen scientific insight and eye for detail. I also want to make sure to thank the newest DDT lab members **Megan McCarthey, Peter Martin, Ang Li, Mike Fealey, Cheng Her, and Yahor Savich** for their help and support. Further, I am extremely thankful for the guidance and aid I received from **Sarah Blakely** and **Octavian Cornea**.

I would not have been able to pursue this thesis research without the inventions from Fluorescence Innovations. Thank you **Kurt Peterson**, **Benjamin Grant**, and **Greg Gillispie**. Greg, thank you for never giving up on me and always keeping your door open,

and the “moose head”. Thank you for treating me as your friend, sharing your latest ideas, and always analyzing the data. Kurt, thank you for always letting me use your latest inventions, staying late so many times, and flying helicopters. Ben, thank you for being FI’s enforcer, teaching me Matlab, and always listening to my ideas while sharing yours.

Finally, I want to thank my parents for pushing me to pursue my dreams, mom and dad I could not have done this without your support. Lastly, I want to thank the love of my life, my wife Christina, for supporting me and my children throughout this journey.

Dedication

To my loving wife Christina and my children Landen, Kailyn, Madilyn, and Aubrey.

Abstract

The sarco/endoplasmic reticulum calcium ATPase (SERCA) is the calcium pump responsible for maintaining cellular calcium homeostasis. Diminished SERCA function has been directly linked to numerous degenerative disease states, such as heart failure. The pathological progression of heart failure is associated with an elevated level of cytosolic calcium, and impairs the function of the muscle contraction-cycle. The overarching goal of this research is to discover novel small-molecule effectors, capable of enhancing SERCA's ability to pump and store calcium within the sarcoplasmic reticulum (SR). Drugs that increase the calcium pumping efficiency of SERCA will restore calcium homeostasis by reducing the calcium content in the cytosol, and enhance impaired cardiac function.

The process of drug discovery is a high-risk effort, and involves screening millions of small-molecules to fortuitously discover a lead compound with high-therapeutic potential. The precise placement of two fluorescent proteins at specific locations along SERCA's cytosolic headpiece, allows for the detection of fluorescence resonance energy transfer (FRET) between donor and acceptor fluorescent proteins. Human cell lines that overexpress this fluorescent fusion protein were generated, creating a live-cell biosensor. The rate of energy transfer (FRET) is dependent on the distance between the fluorescent probes and linked to the enzymatic activity of SERCA. FRET tracks SERCA's structural status, while it pumps calcium into the sarcoplasmic reticulum. These biosensors are grown in vast quantities, harvested, and utilized for high-throughput drug screening. The cells are dispensed into high-density microplates, where each well contains a different compound.

FRET is detected using proprietary fluorescence technology, capable of recording the nanosecond fluorescence decay rate (lifetime) and the full emission spectrum. Both lifetime and spectral modes offer incredibly fast speeds, with high resolution and precision. High-throughput screening by lifetime mode offers the advantage of resolving the structural status of the FRET biosensor because the mole fraction of each structural state is assessed, and candidate compounds found during the screening process can be characterized by their structural effect on the biosensor. High-throughput screening by spectral mode increases assays precision by taking into account the shape of the fluorescence emission spectrum. The shapes of these spectra are decomposed into the contribution of known components by a novel spectral unmixing method, and further used to accurately evaluate FRET. When coupled with lifetime mode, spectral-based drug screening increases assay precision and removes artifacts from cellular autofluorescence and fluorescent compounds. The complementary advantages of coupling spectral and lifetime fluorescence measurements significantly reduces the rate of false-positives from high-throughput drug screens. The development of the technology and FRET biosensor assay, drastically increases the probability of identifying a novel drug with great therapeutic potential.

Table of Contents

Contents

List of Tables

List of Figures

Chapter 1 – Introduction

1.1 Calcium Signaling

Calcium (Ca^{2+}) ions are an essential element for life. Cells are dependent on calcium. Nearly every cellular process is governed or influenced by the positively charged divalent cation [1]. Cells have developed multiple methods to regulate calcium including proteins to buffer calcium for storage within subcellular compartments, pumps and exchangers to create concentration gradients, ion channels to act quickly in response to certain stimuli, and various receptors with signaling mechanisms capable of initiating the complex process of exocytosis or muscle contraction. Calcium signals can be processed in the temporal and spatial domains. For example during muscle contraction, time-dependent fluctuations of calcium, are required in order to ensure that force is generated when needed. Other signals, such as the activation of particular transcription factors in the nucleus of neurons for memory storage, require localized calcium signaling networks [2].

The majority of complex cellular processes are regulated by calcium signaling, and allow for great functional diversity across cell types. One common component, is that cellular survival depends on maintaining low levels of calcium within the cytosolic space. Cells cannot tolerate calcium concentrations higher than 10 μM, as levels above this will lead to protein and DNA aggregation, precipitation of phosphates, and permeabilization of cellular membranes [3]. A complex network of calcium handling proteins ensures the cytosolic calcium content remains low, around 10-100 nM, and that any fluctuation is tightly controlled for a specific purpose [4]. When the homeostatic nature of the calcium signaling network fails, cells are able to respond and adapt, but prolonged dysregulation of

calcium handling is associated with, if not the cause of, many degenerative disease states [5].

Calcium homeostasis is controlled by regulating its influx, efflux, and availability (**Figure 1**). Calcium channels allow calcium to enter the cell and can be activated by voltage, ligand, or mechanical stimulation. Once inside the cell, a calcium transient can activate a plethora of signaling mechanisms, which depend on the type of cell or other environmental factors. Mechanisms which increase the amount of calcium within the cytosol are considered 'On' reactions and are capable of affecting a wide range of processes from exocytosis, muscle contraction, metabolism, transcription, or even fertilization [6]. Calcium buffers or sensors prolong or propagate the on reaction. The calcium sensors troponin C and calmodulin bind calcium through four EF-hand motifs, which produces a large conformational shift in the protein's structure. In the case of troponin C, this conformational shift moves the troponin complex away from actin, allowing myosin to bind and cause muscle contraction. For the muscle to properly relax, calcium must be efficiently removed so that it can be used again.

The removal of calcium from the cytosol is referred to as an 'off' mechanism in the calcium homeostasis model shown in **Figure 1**. Many exchangers and pumps have been described but the majority of calcium is either pumped out of the cell at the plasma membrane by the sodium/calcium exchanger (NCX) and the plasma membrane calcium pump (PMCA), or calcium is stored and sequestered within the endoplasmic or sarcoplasmic reticulum by the sarco/endoplasmic reticulum calcium ATPase (SERCA) [7]. SERCA is responsible for generating a 10,000 fold gradient of calcium across the ER

membrane. The calcium stores located within the endoplasmic reticulum are crucial for the production of new proteins but also for maintaining ample amounts of calcium. Calcium within the ER can be released for a multitude of signaling cascades as previously mentioned.

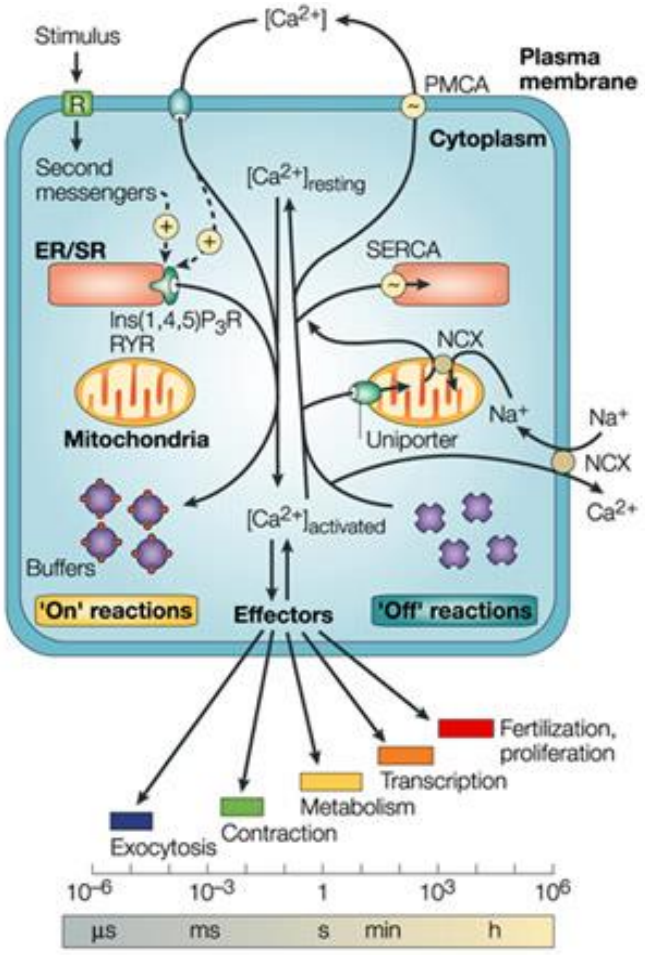

Figure 1. Calcium signaling requires 'on' and 'off' reactions to maintain calcium homeostasis. Calcium channels allow calcium to enter the cells ('on' reaction) and can be activated chemically, electrically, or mechanically. Membrane proteins such as the sodium-calcium exchanger (NCX) and the plasma membrane calcium ATPase (PMCA) contribute to the 'off' reaction by removing calcium from the cell. Calcium (red dots) can be buffered in the cytosol. The sarco/endoplasmic calcium ATPase (SERCA) pumps in the ER/SR generate calcium stores. Calcium is released from these stores by inositol 1,4,5-tripohosphate receptor or the ryanodine receptor and then signals numerous effectors involved in a vast array of processed from exocytosis to fertilization. Proper balance of the on and off calcium signaling pathways is necessary for preserving the health of cells. Reprinted from [6].

Calcium release channels (CRC) such as the inositol 1,4,5-triphosphate receptor (IP3R) and the ryanodine receptor (RYR) release calcium from the ER into the cytosol when activated by an appropriate signal or stimulus [8]. Proper timing and regulation of ER calcium release is essential for electrically-stimulated cell types such as cardiomyocytes, β-pancreatic cells, and neurons. RYR is the major calcium channel in these specialized cell types and specific isoforms such as RYR1 are expressed in skeletal myocytes and RYR2 in cardiomyocytes [9]. A notable distinction between these two

isoforms of the RYR calcium channel is that RYR1 is activated by depolarization through mechanical linkage with the dihydropyridine receptor (DHPR), whereas RYR2 is activated through a calcium-induced calcium release (CICR) mechanism. The RYR isoforms share 60% sequence homology and have tissue-specific expression and regulation. These differences and many others across the plethora of calcium-binding proteins, allow for fine control of the processes involved in maintaining calcium homeostasis [10].

The failure of these systems to properly handle calcium is linked to the progression of many diseases. For example, loss of calcium homeostasis is found in heart failure [11]. The regulation and function of many proteins along the calcium-signaling cascade are detrimentally affected, but the role of the calcium pump SERCA2a has been shown to be a primary culprit in cardiac malfunction. Therapeutic strategies with the goal of correcting these calcium signaling deficits by targeting SERCA or its regulators, have been found to ameliorate the symptoms of heart disease. Exploration of SERCA's role in calcium signaling will be essential for discovering new ways to treat cardiomyopathies [12].

1.2 The Calcium Pump SERCA

SERCA is a P-type ATPase that uses energy from adenosine triphosphate (ATP) to pump two calcium cations from the cytosol into the endoplasmic or sarcoplasmic reticulum. The four different types of ATPase transporters are the P-, F-, V-types and ABC transporter (Figure **2**)[13]. The P-type ATPases transport calcium through the formation of an aspartyl-phosphoenzyme intermediate, providing the energy required to actively pump calcium across the hydrophobic lipid membrane bilayer against a large calcium concentration gradient.

The F-type ATPase transporters are responsible for producing ATP in mitochondria and chloroplasts by using energy derived from an electrochemical gradient of protons established by the electron transport chain. ATP-binding cassette (ABC)-transporters shuttle many essential nutrients into and out of cells. Fifty different ABC-transporters have been identified in humans. Genetic mutations of the ABC transporters are the cause of debilitating diseases such as cystic fibrosis (CFTR) and changes in protein expression and substrate sensitivity are directly linked to development of drug-resistant metastatic cancers [14]. Less is known about the vacuolar V-type ATPases. They are responsible for generating proton gradients within intracellular vesicles and are involved in endo/exocytosis processes [15]. The four different classes of ATPase transporters work hard to maintain appropriate levels of ions and nutrients within the cell and the malfunction of any one of them, has been directly related to numerous diseases and

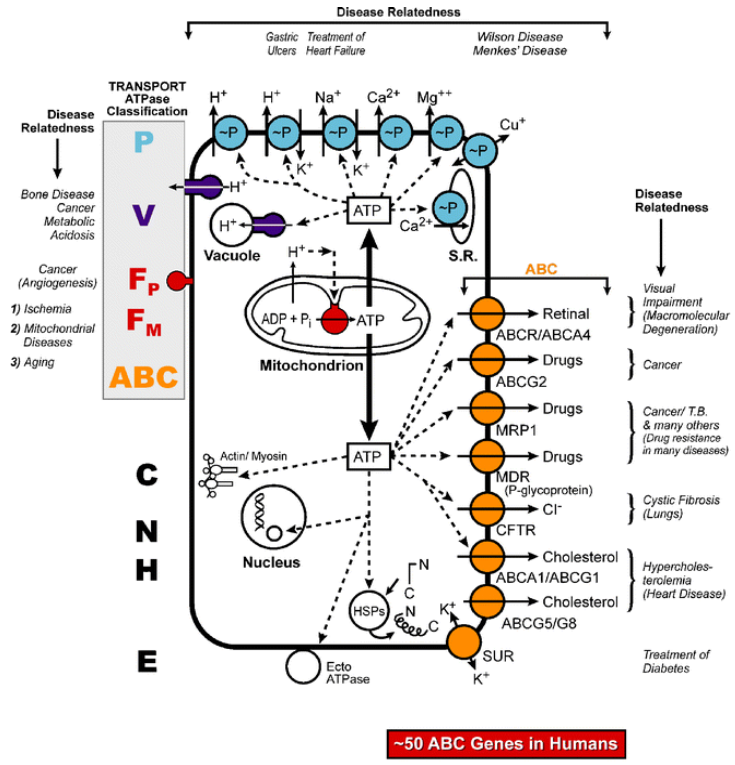

Figure 2. The P-, V-, F- type and ABC transporters make up the four categories of ATPases. The P-type ATPases utilize energy from ATP to actively pump ions out of cells or in SERCA's case pump calcium into the ER. V-type ATPases generate proton gradients in intracellular vesicles. The F-type transporters harness energy from the proton gradient produced by the electron transport chain to make ATP. The ABC-transporters move a wide variety of larger molecules into and out of cells. Numerous diseases states are linked to the dysfunction of each transporter type and described in the figure. Reprinted from [13]

disorders as shown in Figure **2**.

Cyclical calcium transport into the specialized calcium storage organelle, called the sarcoplasmic reticulum (SR) in muscle cells, is triggered by action potentials along the sarcolemma membrane. These action potentials originate from signals from the brain or pacemaker cells in the heart, causing the opening of voltage-sensitive calcium channels (L-type). An initial influx of calcium then causes the RYR calcium-release channels to open. Calcium is rapidly released into the cytosol, where it binds to the troponin complex and allows myosin to bind to actin, thereby causing muscles to contract and produce force. The calcium is then removed from the cytosol by SERCA and stored within the SR, so that it can be used during the next contraction cycle. Calcium must be removed efficiently and rapidly during the excitation-contraction process. Improper or delayed clearance of cytosolic calcium results in prolonged contraction and delayed muscle relaxation. The calcium pumping mechanism of SERCA is capable of keeping up with the demands of cardiac and skeletal muscles.

The reaction mechanism of SERCA follows the classic E1/E2 scheme [16]. During the high-calcium affinity E1 state, the calcium-binding sites of SERCA are exposed to the cytosol. In the low-calcium affinity E2 state, these sites are not available at the cytosolic face of SERCA, and face the lumen of the ER, where calcium is released. Under normal conditions, the energy from the hydrolysis of one ATP molecule is used to transport two calcium ions, and counter transport two-three protons across the ER membrane (Figure **3**). First, calcium ions bind to SERCA's calcium-binding sites. SERCA then undergoes a conformational shift, and allows ATP to bind at the nucleotide-binding domain. ATP is

then hydrolyzed, and rapidly autophosphorylates the aspartate at residue 351. A high-energy phosphoenzyme intermediate (E1-ATP-Ca^{2+} state) is formed, where calcium is occluded from the cytosolic face of SERCA. This state is very unstable. ADP is then released from the nucleotide-binding domain, and SERCA undergoes a large-scale conformational change. Calcium ions are transported through the membrane, and released them into the lumen of the ER. Finally, SERCA is dephosphorylated, and transitions from the E2P to E2 state. The cycle starts over with a transition back to the E1 state [15]. This reaction is highly efficient, and the coupling of energy consumption of ATP is expected to match the energy used to pump two calcium ions at 12 kcal/mol per cycle [17].

1.3 SERCA Structural Biology

SERCA is by far the most studied calcium ATPase, with over 50 published crystal structures, all of the SERCA1a isoform. SERCA1a is the fast-twitch skeletal muscle isoform [19]; but many crucial details about this membrane-bound enzyme remain to be

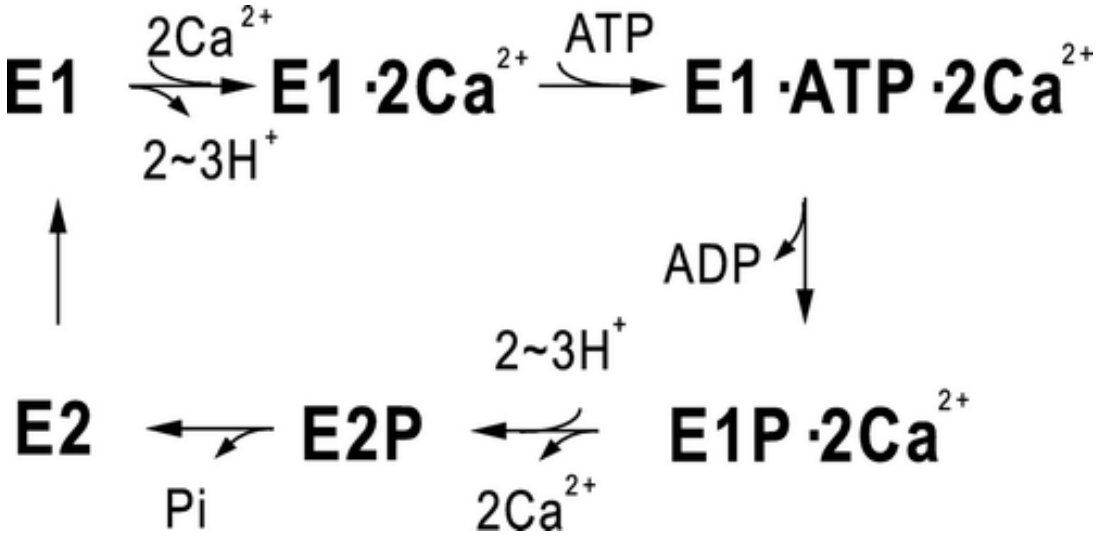

Figure 3. A simplified E1/E2 reaction of SERCA's enzymatic cycle. SERCA binds calcium in the high-affinity E1 state. A covalent interaction with ATP occurs at the nucleotide binding-domain of SERCA, and autophosphorylates the aspartate residue 351, forming an unstabe phosphoenzyme intermediate (E1-ATP-$2Ca^{2+}$). ADP is then released, and SERCA shifts towards the low-affinity E2 state. Calcium is subsequently released into the ER lumen, and phosphate dissociates from SERCA. Adapted from [18].

answered, and further exploited. SERCA is an integral membrane protein consisting of 10-11 transmembrane domains (depending on the isoform), with a large cytosolic headpiece; comprised of the actuator, nucleotide-binding, and phosphorylation domains (Figure **4**). This headpiece is predicted to exhibit large-scale (> 20 Å) molecular movements, based on crystal structures obtained under conditions, designed to trap SERCA at discrete points during its enzymatic cycle [19]. Emerging evidence, from crystallography [20], fluorescence resonance energy transfer [21, 22], and molecular dynamics simulations [23], suggests that SERCA's cytoplasmic headpiece undergoes large-scale transitions between compact and open structural states, that are functionally important.

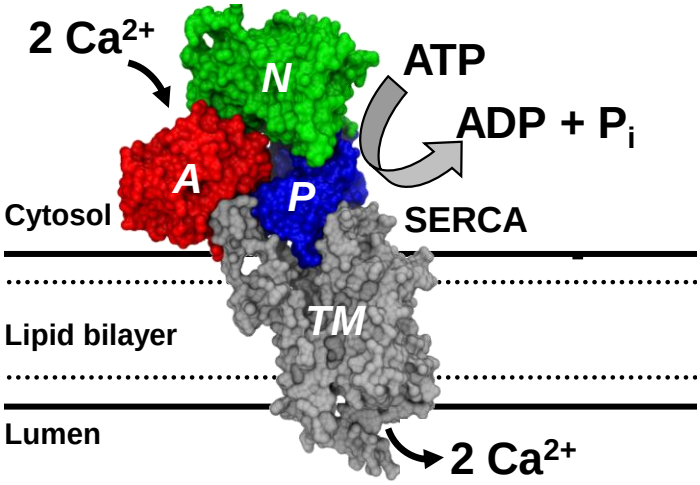

Figure 4. Structural model of SERCA. There are three cytosolic domains and 10-11 transmembrane (TM) helix regions. The actuator-domain (red), nucleotide-binding domain (green), and phosphorylation domain (blue) undergo large-scale structural rearrangement as calcium is transported across the lipid membrane at the expense of ATP hydrolysis. **[24, 25]**

The structural information obtained from x-ray crystallography studies have elucidated the role that each of the three cytosolic domains play throughout the E1-E2 reaction scheme. It is pertinent to note that crystal structures represent static pictures of SERCA's structural biology, and the methodologies used to form highly-ordered and well-diffracting crystals, rely on locking SERCA in one particular state. These methods include

$$E + Ca^{2+} \overset{1}{\leftrightarrow} ECa \overset{2}{\leftrightarrow} E'Ca + Ca^{2+} \overset{3}{\leftrightarrow} E''Ca_2$$

Figure 5. Sequential calcium reaction is cooperative (1 and 3), and dependent upon slow structural binding transition (2) [26].

the use of high protein concentrations of SERCA (derived from the skeletal muscles of rabbits), detergents, high calcium concentrations (greater than 10 mM), incubation with SERCA inhibitors, nucleotide and phosphate analogues, to investigate the intermediate states [15]. These conditions may perturb SERCA's structure in ways that are not physiologically relevant, but have consistently shown that structural rearrangement of the A-, N-, and P-domains is required for calcium transport.

The initiation of SERCA's enzymatic cycle, requires that calcium binding occurs before ATP binds to the nucleotide-binding domain [27]. Calcium binding occurs at two separate sites at the cytosolic side of lipid membrane. Calcium binding is sequential and cooperative, where site I is the low-affinity binding-site (10 μM). Calcium-binding at site I repositions Asp800, and causes the sixth transmembrane region (M6) to rotate, thereby rearranging the positions of oxygen atoms in the second calcium-binding site (site II). This creates a properly formed calcium-binding pocket, with high-affinity towards calcium (50 nM) [28, 29]. The binding signal from site II is then transmitted to the phosphorylation domain, nearly 50 angstroms away. This mechanical transmission occurs through structural changes linking the transmembrane helix 5 (M5), near site II to the P-domain, coupling the calcium pumping and ATPase hydrolysis activities of SERCA [24].

The cooperative interaction of SERCA's structural change and its two calcium binding sites is depicted by the reaction in **Figure 5**. Calcium binds rapidly at site I (1), inducing a slow conformational change (2). In this conformation (E'), SERCA is unable to utilize ATP until a second calcium binds, and occupies the newly formed calcium-binding site II. Conformation (E'') represents the activated enzyme, commonly referred to as the

high-affinity E1-state. Steady-state and transient kinetic intrinsic fluorescence studies revealed the slow calcium-dependent isomerization, with the following equilibrium constants (epxeriments performed at 25° C and buffered with media containing 50 mM buffer (Tris, pH 8.5, Mops, pH 6.8, or Mes, pH 6.0), 80 mM KCl, 10 mM MgCl,, 0.1 mg of SR protein/ml, and EGTA and Ca2+ to yield the required free Ca^{2+} concentrations: k_1 =4.25 x 10^7 M^{-1} s^{-1}, k_{-1} = 450 s^{-1}, k_2 = 15 $s^{-1,}$ k_{-2} = 33 s^{-1}, k_3 =1x 10^8 M^{-1} s^{-1}, k_{-3} = 18 s^{-1} [30, 31]. Studies using recombinately expressed SERCA mutants have also been performed to targeted residues specific for coordinating calcium ions at each binding site, as well as, the nucleotide binding site. Residues Glu771, Thr799, Asp800, and Glu908 were found to be critical for coordination of the calcium ion in the first binding site, providing stabilization of the entire Ca^{2+} binding domain, and were required to initiate the structural transition as modeled by the sequential binding equation [26].

Structural and functional studies demonstrate that SERCA undergoes large-scale structural rearrangements with a simplified mechanistic model, depicting at least two distinct E1 and E2 enzymatic states. A full model of the enzymatic cycle, based on experimental evidence and simulations, includes at least twelve partial reactions [30, 31]. Crystal structures have been solved for many of the states associated with these partial reactions, suggesting that a dynamic equilibrium of the structural states exists [19]. Understanding these structure-function relationships, and their rate-limiting steps will be valuable for discovery of small-molecules or peptide-regulators, which control SERCA's function.

1.4 SERCA Isoforms

The family of known SERCA isoforms has expanded in recent years, with over 11 known human mRNA transcripts and proteins now identified (**Figure 6**); each with its own distinct kinetic parameters and tissue-specific expression. The ATP2A (SERCA) gene products are members of the (E1-E2) P-type ATPase family [32]. The SERCA1a isoform has paved the way for structural comparisons to other isoforms, as it is easily obtained from rabbit skeletal muscle. Currently, crystal structures do not exist for any of the other SERCA isoforms. In humans, SERCA is encoded by three separate genes, located on different chromosomes (**Figure 6**). Sequence diversity is enhanced through alternative splicing, primarily at the 3' carboxy terminus. SERCA is highly conserved across its isoforms, with SERCA1 being 84% homologous to SERCA2, and 75% homologous to SERCA3 [33].

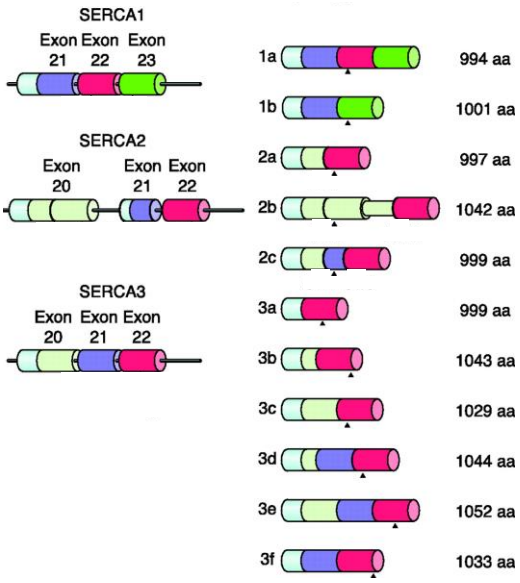

Figure 6. Alternative splicing of three SERCA genes (ATP2a1-3). Exons are colored cylinders and introns black lines. Thinner cylinder in SERCA2b is an untranslated pseudoexon. Black triangles indicate the position of the different stop. Reprinted and adapted from [34].

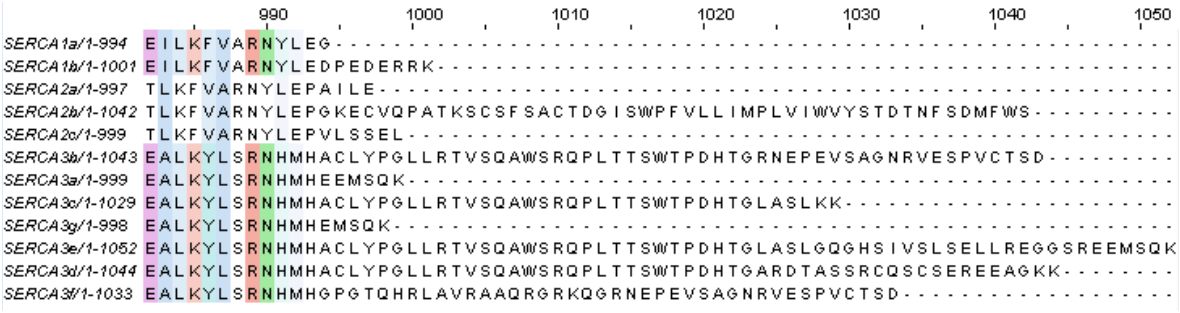

Figure 7. Alignment of human SERCA isoforms showing the difference in c-terminus due to alternative splicing.

SERCA2b is ubiquitously expressed in all tissue types, and is the most ancient isoform. The isoforms SERCA2c and SERCA3d, e, and f are unique to humans. Studies of mutant and chimeric proteins, suggest that the functional differences of calcium binding affinity and pumping rates, are due primarily to differences in the C-terminal segment of SERCA (**Figure 7**). In particular, the 2b isoform contains an additional 11^{th} C-terminal transmembrane domain. A series of chimeric SERCA1a proteins were engineered to add the additional C-terminal segment from SERCA2b. These studies generated a model in which the SERCA2b tail interacts with and displaces specific luminal domains (7 and 8), thereby stabilizing the high-affinity E1 state [35]. This model is consistent with the higher apparent calcium affinity ($1/K_{Ca}$) and slower catalytic turnover rate (V_{max}) of the SERCA2b isoform.

Kinetics of SERCA Isoforms

The kinetic parameters of the human SERCA isoforms are becoming more clearly defined. SERCA can now be expressed as a recombinant protein, and isolated through the fractionation of the ER or SR; where acid-quenched transient kinetic studies have resolved the rate constants throughout the E1-E2 enzymatic cycle. These methods have shown that the SERCA isoforms are distinguished by their turnover rate V_{max} at saturating calcium (2b, c <2a <3a, b, c <1a) (**Figure 8A**), and their affinity $1/K_{Ca}$ for calcium (2b> 2a>1a> 2c> 3) (**Figure 8B**) [36],[37],[38]. SERCA1a has the highest rate of catalytic activity (V_{max} ~130 s^{-1}), and the ubiquitously expressed 2b has the lowest (V_{max} ~35 s^{-1}). SERCA3 exhibits very low calcium affinity (approximately $1/10^{th}$ that of SERCA1a), but has a rapid

rate of catalytic activity (V_{max} ~100 s^{-1}) [37]. However, no direct comparison has been made of the human SERCA isoforms expressed or reconstituted in the similar membrane environments. Kinetics experiments have been compared to results for rabbit SERCA1a, which has 963/994 (97%) primary sequence homology to human SERCA1a, with 11/994 (1%) of the amino acid difference at the C-terminus [39].

The diverse enzymatic properties among the SERCA isoforms, allow for fine tuning and modulation of calcium handling, for specific physiological processes and cellular phenotypes. SERCA1a is primarily expressed in adult fast-twitch skeletal muscle, whereas the longer SERCA1b is found in fetal tissues. SERCA1a's high V_{max} and low ($1/K_{Ca}$) are ideal for the dynamic calcium cycling required for fast-twitch skeletal muscle contraction. Evidence exists that novel SERCA1 truncated variants (ST1s) are found in cardiac tissue, which may act to slow or even abolish calcium transport [40].

SERCA2 consists of four alternatively spliced variants. SERCA2a is found in cardiac tissue, under adrenergic control of small-peptide regulator phopholamban (PLB). SERCA2a exhibits the kinetic properties for rapid clearance of calcium from the cytosol, necessary for cardiac muscle relaxation. SERCA2b is ubiquitously expressed throughout all tissue types, with a higher apparent calcium-affinity ($1/K_{Ca}$), and lower turnover of ATP at saturating calcium (V_{max}), compared with SERCA2a. SERCA2b is usually found to be expressed along with other isoforms, which have

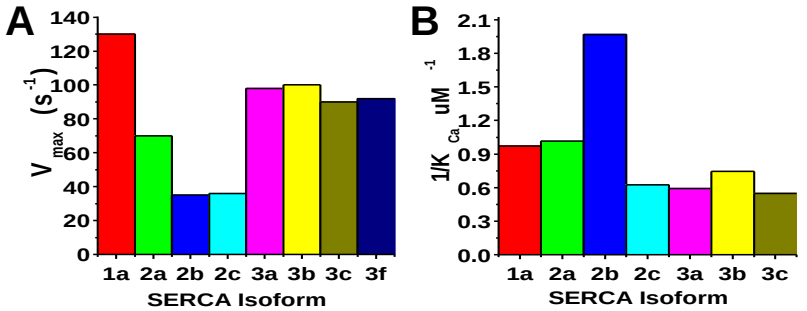

Figure 8. SERCA isoform kinetics **A.** Catalytic turnover (V_{max}) **B.** Calcium affinity ($1/K_{Ca}$) [36],[37],[38].

the appropriate enzymatic properties to finely tune calcium transport in combination with SERCA2b. For example, the human-specific SERCA2c isoform is found in cardiac muscle, skeletal muscle, and hematopoietic cells. SERCA2c displays enzymatic properties quite different from those of SERCA2a, with a lower calcium-affinity ($1/K_{Ca}$), and a much lower $V_{max.}$ In cardiac tissue, SERCA2c was found to be restricted to the subplasmalemmal area and intercalated disks [41], where the calcium concentration is high. In contrast, SERCA2a and 2b are located near T-tubules and longitudinal SR [42]. SERCA2c has a similar effect on the levels of cytosolic calcium as SERCA2a and 2b, but its activation only at high cytosolic calcium concentrations aids in the rapid removal of calcium [43]. The discovery of differential compartmentalization of SERCA isoforms within the ER or SR illustrates the complexity of SERCA's role in maintaining calcium homeostasis.

SERCA3's role in calcium transport is less well understood in comparison to SERCA1 and 2. Its low-calcium affinity, high-catalytic activity, and co-expression with SERCA2b suggests that it is a fine tuner of calcium transport [41]. Six 3'-carboxy terminal variants (a through f) of SERCA3 are found in humans, with SERCA3a found in all mammals. SERCA 3d and f are found only in humans (**Figure 6**). More SERCA3 isoforms have been discovered, and are specifically restricted to the rat and mouse. The SERCA3 variants are differentially expressed in a wide variety of muscle and non-muscle cells, with the highest expression found in hematopoietic cells. They further exhibit compartmentalization at discrete subcellular locations, with kinetics similar to that of SERCA2c, but with an even higher rate of catalytic turnover [43]. These kinetic parameters

make them suitable to exist in locations where calcium concentration is high, and allow them to remain inactive at resting cytosolic concentrations of 50-100 nM.

The SERCA3 variants all transport calcium differently, with SERCA3a, c, and e maintaining the lowest cytosolic concentrations, and SERCA3b, d, and f maintaining the highest ER concentrations [37]. In human embyronic kidney 293 (HEK) cells, where SERCA2b and SERCA3d are expressed [44], overexpression of human-specific SERCA3f induced apoptosis. Interestingly, SERCA3f expression was found to be upregulated in heart failure, in conjunction with SERCA2a being down-regulated. The rise in SERCA3f was further shown to be closely correlated with an increase in markers for endoplasmic reticulum (ER) stress, as the levels X-box-binding protein-1 (XBP-1) and glucose-regulated protein (GRP) were increased. SERCA's role in maintaining a high calcium reserve in the SR is important for the processes of cardiac excitation-contraction coupling and relaxation. This evidence sheds new light on how the malfunction of the ER leads to the pathophysiological processes of heart failure. In cardiomyocytes, SERCA3f is found at the same subcellular compartments (longitudinal SR) as SERCA2a, but no published rationale has been made for why heart failure is associated with an increase in 3f and a decrease in 2a [45]. The conclusion of this study demonstrated how species-specific SERCA splicing is important for the pump's enzymatic properties, and subcellular enzyme compartmentalization. Further, how these are aspects are linked to the induction of ER stress in human cardiomyopathies. This same pathological response has been found in numerous disease states, where the relevance of SERCA isoforms is only now starting to be investigated.

1.5 SERCA Regulators

PLB

The different SERCA isoforms are expressed in specific tissues types along with their regulators. In the human heart, the small 52 amino acid peptide phospholamban (PLB) regulates SERCA2a function. PLB is a sarcoplasmic reticulum (SR) membrane-bound peptide that is regulated by adrenergic stimulation. PLB inhibits SERCA by decreasing its apparent calcium-affinity, when the heart is not pumping blood at maximum capacity (bradycardia), and the cytosolic calcium concentrations are low. When the heart rate increases, and the heart needs to pump blood more efficiently, SERCA's inhibition by PLB is relieved through phosphorylation. PLB phosphorylation occurs at serine16 by PKA [46], or at threonine17 by Ca^{2+}/Calmodulin Kinase II (CAMKII) [47].

Phosphorylation of PLB relieves SERCA's inhibition, and is regulated through a structural transition of the cytoplasmic tail of PLB. Upon phosphorylation, PLB switches from a tense (T) to a relaxed (R) state [48]. This order-to-disorder structural transition, destabilizes PLB's cytoplasmic domain helix, and disrupts its inhibitory interactions with SERCA. The T and R states exist in a dynamic equilibrium, where phosphorylation is tightly-regulated through multiple pathways. This allows for fine-tuning of SERCA's activity, and further the contraction-relaxation properties of the heart muscle. This allosteric regulation of SERCA has become an attractive therapeutic target for gene-therapy, and small-molecule drug discovery. Both strategies have the goal of finding new ways to shift PLB toward the R state to increase SERCA's activity.

SLN

Sarcolipin (SLN) is another SR membrane-bound regulator of SERCA's activity. This 31 amino acid peptide is primarily expressed in the atrium of the heart and skeletal muscle. The differential expression of SERCA regulators in the heart (PLB in ventricles, SLN in atria), suggests that the contractile properties of these compartments are dependent on SERCA's ability to efficiently clear calcium from the cytosol. SERCA regulation is important for promoting muscle relaxation, by ensuring calcium is properly sequestered during each round of the contractile cycle [49]. In parallel to its homologue PLB, SLN was found to inhibit SERCA's function by decreasing its apparent calcium affinity. SERCA inhibition is relieved by SLN phosphorylation at serine5 [50]. SLN is also found in skeletal muscle, and regulates SERCA1a. Recently, SLN has been found to control thermogenesis by uncoupling SERCA's calcium transport from ATPase hydrolysis [51].

SLN's ability to produce heat through non-shivering thermogenesis, by altering SERCA's ability to utilize ATP hydrolysis for calcium transport, raises new questions

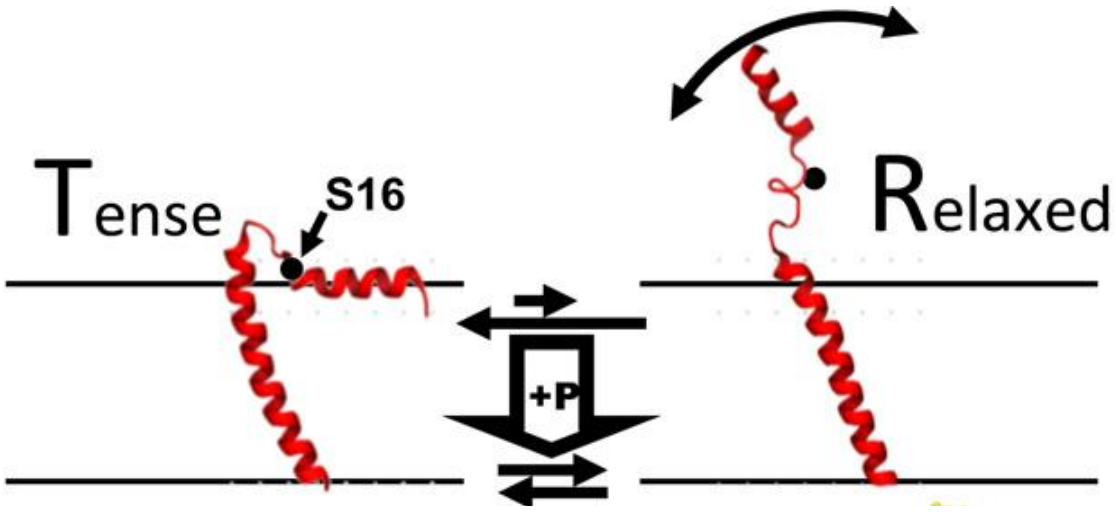

Figure 9. The 52 amino acid phosopeptide PLB (red) exists in an equilibrium of two structural states. In the tense state, PLB inhibits SERCA's function. Upon phosphorylation at serine16 by PKA, PLB's cytoplasmic domain becomes disordered, relieving SERCA inhibition. Adapted from **[48].**

about SERCA's enzymatic cycle. The crystal structure of SLN bound to SERCA shows that sarcolipin binds to the same site as PLB [19]. Unlike PLB, SLN was found to promote the high-affinity E1 structural state of SERCA. Recent evidence suggests that the cytosolic domain of SLN forms a covalent bond with the second calcium binding site on SERCA (residue E309), blocking the ability to bind the second calcium ion, but allowing SERCA to hydrolyze ATP [52]. The regulatory mechanisms of SERCA enzymatic cycle are becoming more and more complex, as the list of regulatory partners continues to grow, but continually offer new insights, and potentially therapeutic opportunities to control SERCA's malfunction during heart failure [53], type II diabetes, or obesity [54].

DWORF, ELN, and ALN

The most recent small-peptide SERCA regulators to be identified were previously annotated as long non-coding RNA sequences [55]. These sequences were shown to code for proteins which alter SERCA's function with tissue-specific expression. The 32 amino-acid sarcoplasmic reticulum membrane-bound protein named dwarf opening reading frame (DWORF) was discovered to be preferentially expressed in cardiac tissue, and activate SERCA by inhibiting binding of PLB. DWORF was not found to increase SERCA's activity on its own, and competitively inhibited the binding of PLB, SLN, and also the skeletal-muscle specific peptide regulator myoregulin. DWORF expression was found to be upregulated in models of heart disease, possibly by a compensatory mechanism to increase SERCA function.

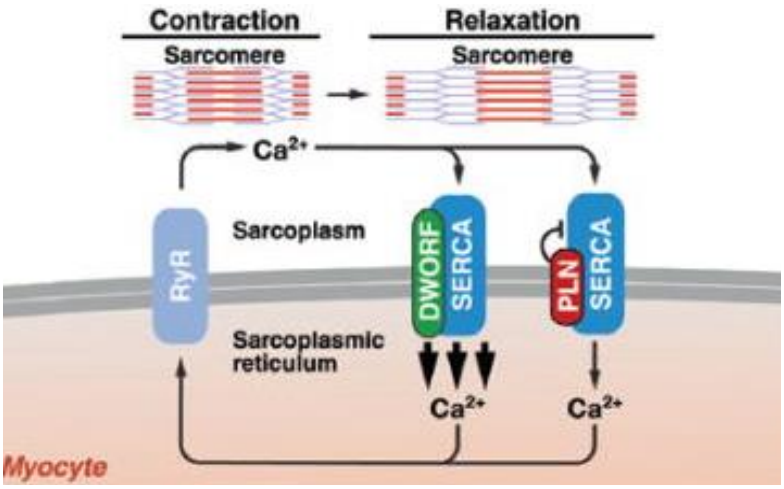

Figure 10. The recently identified SERCA regulator DWORF activates SERCA in the heart by competively inhibiting PLB. Adapted from **[55]**

The DWORF amino acid sequence is homologous to PLB and SLN. A key difference of the PLB and SLN sequences in comparison to DWORF, is that DWORF has a hydrophobic residue (I16) in place of the inhibitory polar residues N34 found on PLB, and N11 found on SLN. The most recently identified SERCA regulator homologues endoregulin (ELN) and another-regulin (ALN) also share functional similarities to PLB and SLN. Both ELN and ALN inhibit SERCA's function, except they expressed preferentially in non-muscle tissues, and were shown to inhibit the corresponding tissue-specific SERCA isoforms 2b and 3 [56]. These exciting discoveries of novel SERCA regulators have led to collaborative efforts to identify the structural basis of tissue-specific SERCA regulation.

Chapter 2 – Therapeutic Targets and Applications of SERCA Activators

The role of the calcium pump SERCA in maintaining calcium homeostasis, required for cells to function properly, has linked its malfunction or loss to diseases previously unconsidered [57]. As SERCA's enzymatic function has now become more clearly defined through structural studies and dynamic molecular simulations [23],there is a definite need to link these aspects to allosteric drug interactions and genomics. This approach will lead to new avenues in the pursuit to correct aberrant calcium signaling and handling, with the intention of mitigating cellular stress and apoptosis. The goals of stimulating SERCA's enzymatic capacity by simply increasing its abundance, through gene therapy, initially proved successful in clinical trials [58]. Unfortunately, the phase II clinical trial Calcium Upregulation by Percutaneous Administration of Gene Therapy in Cardiac Disease (CUPID) did not meet its primary end goals. SERCA2a was delivered directly into the hearts of patients experiencing advance heart failure, using single intracoronary infusion of adeno-associated virus I (AAV1). The trial was halted because the level of SERCA2a expression in patients was not sufficient to mimic the results found in large animal studies. Additionally, this therapeutic approach is limited because many patients with heart failure have neutralizing antibodies against the AAV vectors [59]. The development of more efficient cardiac-targeted vector delivery, and alternate targets such as SERCA's regulators [60] are currently being evaluated, holding promise for the future gene therapeutic treatments of heart failure.

Alternative strategies to gene therapy, by targeting regulators of SERCA through transcription factors, protein modulators, and allosteric small-molecules depict how

important target specificity will be for drug discovery. Maintenance of calcium at very precise levels within the cytosol of contractile cells is dependent on other ion channels and pumps, and for reasons still being revealed, interact with every currently identified SERCA modulator, in some way or another. Understanding the details of these mechanisms, may lead to the development of small-molecules or peptides, which do not have the harmful side effects of many of the discovered SERCA modulators to date.

Recent advances in high-throughput drug screening [61] have made it possible to identify novel compounds, which can alleviate altered calcium levels found in the cytosol of cells throughout numerous diseases such as Alzheimer's disease [62], diabetes [54], and heart failure. In these diseases, SERCA functions to restore calcium homeostasis by actively pumping Ca^{2+} from the cytosol into the sarcoplasmic reticulum (SR) or endoplasmic reticulum (ER), against its gradient. It is well known that when cells are under stress, expression of the calcium pump SERCA becomes down regulated, further disrupting calcium homeostasis, leading to apoptosis, and ultimately the uncontrolled progression of disease states [63]. The common feature of elevated calcium levels in the cytosol is found in a wide range of muscle and metabolic disorders. In cardiomyocytes, elevated calcium levels in the cytosol lead to impaired muscle relaxation during diastole, as calcium continuously signals myosin to attach and form crossbridges with actin. The prolonged effect of calcium extenuates systole [41]. In other non-muscle diseases, elevated cytosolic calcium levels have been linked to immunogenic, ER stress, and mitochondrial dysfunction. SERCA's ability to maintain homeostasis of calcium cycling, makes it a very attractive target for drug discovery and therapeutics.

It is paramount to find novel small-molecule activators of SERCA, which can mitigate elevated cellular cytosolic calcium concentrations. Novel drug screening assays and platforms are now making this endeavor possible, where a recent screen discovered six novel allosteric SERCA activators [61]. Activators of SERCA have long been sought after for the use of treating cardiac disease and malfunction [64]. There are many ways SERCA's function or activity can be altered. These include upregulation of the pump itself or its function. Allosteric modulators that alter SERCA's function may work by increasing the catalytic activity of the membrane bound enzyme or by increasing its binding-affinity for calcium.

2.1 SERCA Transcriptional Regulation

Thyroid Hormone

Many studies have elucidated the promoter of SERCA, and found specific transcriptional regulators with the ability to increase the overall expression of the various SERCA isoforms. It was first reported that the -284 to -72 bp proximal promoter region of the cardiac specific SERCA isoform is required for translational upregulation [65]. The thyroid response element was identified at the enhancer region, located directly upstream of SERCA promoter region. The thyroid hormone regulates many proteins in the heart, including the β-adrenergic receptors, α-MHC, titin, the Na^+/K^+ ATPase, the NCX exchanger, and SERCA2a [66]. Hypothyroidism precipitates the effects of heart disease, through the symptoms of bradycardia and hypertension. The fact that the thyroid hormone can bind to the enhancer region (regulatory element) and up-regulate transcription of

SERCA is exciting, because the thyroid hormones T4 and T3 would prove an easy therapeutic application for patients with heart disease. The off-target effects on the Na^+/K^+ ATPase, adrenergic receptor, cardiac troponin I, atrial natriuretic peptide, and MHC-P, have proven difficult to develop thyroid hormone therapeutics as a suitable long-term treatment [67]. The T_4 and T_3 thyroid hormone levels drop nearly 60% in patients experiencing heart failure. Clinical trials are underway and have shown that T_3 supplementation therapy improves cardiac function after cardiac bypass operations [68]. The thyroid hormone plays many physiological roles beyond regulating cardiac function, and may only be useful as short-term treatment for cardiac function. Therapeutics such as the thyroid hormone lack specificity for calcium signaling. An elusive goal for drug discovery has been to find compounds which reduce elevated cytosolic calcium levels and the symptoms of heart disease. This goal can be accomplished by the discovery of drugs which act at the level of transcription.

Hypoxia Induced Factor (HIF)

The HIF transcription factor regulates the processes of angiogenesis, metabolism, and oxygen transport. In hypoxic conditions such as those associated with heart disease and failure, HIF up-regulates genes at the hypoxia response element (HRE). HIF expression during cardiac malfunction has been shown to be crucial for successful recovery after a myocardial infarction, where there is a decrease in oxygen delivery. The HIF transcription factor regulates many genes in the heart that improve blood delivery and oxidative metabolism during stressful states. It is considered a potential target for heart failure therapeutics [69]. Recently, it was demonstrated in animal models that many of the

proteins involved in the excitation-contraction coupling required for cardiac contraction were down regulated by HIF. SERC2a mRNA level was reduced to nearly half of its normal abundance, after only 72 hours of induction by HIF. Many putative HRE binding sites for HIF have been identified in the promoter region of SERCA. This study also found that even though HIF has many targets, its effects are the most pronounced on SERC2a, where a single stimulus dramatically and rapidly reduces its expression.

SERC2a expression is decreased in both ischemia and heart failure, causing the heart to lose its contractile ability as calcium is not properly sequestered. The transcription factor HIF may be a key culprit to target when pursuing therapeutics for heart disease. The aforementioned study was not able to clearly identify that HIF was working at SERCA's promoter region. Chromatin immunoprecipitation studies suggest that HIF manipulates SERCA expression through other mechanisms. Finally, HIF impaired calcium flux in cardiomyocytes, and ventricular dysfunction occurred after only seven days of cardiac induction of HIF. HIF alters the expression of many proteins, but altered calcium handling is dependent on decreased SERCA2a expression. This may be the most important factor in the progression of heart failure and disease. HIF may also play similar roles in other diseased states such as Alzheimer's and diabetes, where it was previously shown to disrupt calcium signaling, causing both ER stress and mitochondrial dysfunction in β-pancreatic cells [70]. HIF's direct role in relation to SERCA expression was not studied thoroughly. Interestingly, the Alzheimer disease genes presillin-1 and -2 directly regulate the expression of HIF. The importance of maintaining proper calcium balance in the cytosol is critical for neurodegenerative disease states [71].

Peroxisome proliferator-activated receptors (PPAR-γ)

PPAR-γ is a heterodimer that binds with the retinoid X receptors at specific sequences within the promoters of genes and has been implicated in many disease states, where SERCA's function is required to maintain calcium homeostasis [72]. An agonist binds to the PPAR-γ heterodimers in order to induce cotranscription. Many endogenous agonists exist, and regulate the formation and coactivational properties of PPAR receptors, differentially with specificity to tissue types. In this regard, much effort has been taken in developing novel small-molecule agonists, which can selectively bind specific PPAR receptors, thereby activating particular genes in localized tissues for the treatment of Alzheimer's disease and diabetes [72].

One PPAR-γ agonist pioglitazone is currently used as the standard treatment for Type II diabetes [73]. Pioglitazone activates the transcription of genes involved in glucose control and lipid metabolism in muscle, fat, and pancreatic cell types. Recently, this FDA-approved drug was found to upregulate SERCA expression in diabetic animal models. This again links SERCA's function and calcium-cycling as a determinate or outcome of a disease state. Pioglitazone was found to interact with the promoter region of non-muscle SERCA2b isoform. Promoter-deletion studies identified one PPRE (PPAR-γ response element), the most proximal one to the gene, as being crucial for the upregulation of SERC2b (**Figure. 11).** The drug restored SERCA2b expression in pancreatic β-cells of a diabetic mouse model. SERCA2b expression has also been shown to be decreased in human patients with diabetes, just as SERCA2a is in heart failure. This FDA-approved drug is acting to restore calcium homeostasis by up-regulating the expression of SERCA

[63]. PPAR-γ agonists act on many targets, and are their upstream signaling effects are not specific for SERCA2. They have been restricted for use in Type II diabetes with comorbid heart failure [74]. Recently, therapeutic doses of pioglitazone were found to be harmless in canine cardiomyocytes. Higher doses altered the electrophysiological properties of the canine cardiomyocytes due to the inhibition of sodium, calcium and potassium currents. This raises real concerns for its use in diabetic patients with heart failure [75]. Unwanted drug side effects are a considerable problem for drug discovery, and in this case, the lack of drug specificity has restricted its use. PPAR-γ agonist's role in up-regulating SERCA may have immense implications for directly targeting SERCA for drug discovery, and hopefully overcoming the unwanted side effects of current FDA approved drugs.

Putative PPRE	Position	Sequence
5	-1713 to -1701	AGGCTGAGGTCAG
4	-1162 to -1150	ACAACTGAGGTGA
3	-571 to -559	AGGCGACAGATGA
2	-433 to -421	AGGACATCAGCCC
1	-48 to -36	CGGCGAAAGGGGA

Figure. 11 Five putative PPREs (PPAR-γ response element) were identified in the human SERCA2 promoter. The most proximal PPRE site was proven essential for the upregulation of SERC2b.Adapted from [63]

2.2 Protein Modulators of SERCA Activity

Ca^{2+}/calmodulin-dependent protein kinases II (CAMKII)

The most well-known protein modulators of the SERCA calcium pump are phospholamban (PLB) and sarcolipin (SLN). These small membrane-bound regulators have proven essential for the proper regulation of the SERCA enzymatic cycle throughout the cardiac cycle of systole and diastole [76]. Regulation of these proteins is through direct

phosphorylation via β-adrenergic signaling, and the cyclic AMP-dependent PKA cascade. The various SERCA isoforms are known to be ubiquitously expressed in nearly every cell type in the human body, with the SERCA2b isoform being the most predominant. Currently, PLB and SLN are only known to be expressed in a few tissue types. However, more and more protein modulators of SERCA, with possible cell type and SERCA isoform selectivity, are continued being identified [77].

CAMKII is a threonine/serine-specific kinase that is regulated by the calcium/calmodulin complex, and is an essential regulator for maintenance of calcium homeostasis (**Figure 12**). CAMKII is a key intermediate in numerous cell-signaling cascades involved in cardiomyocyte contraction, or the ability of a neuron to store information to form a memory. It was discovered that CAMKII has the ability to directly phosphorylate SERCA, and increase its activity in airway (pulmonary) smooth muscle cells. PLB was not found at detectable levels in these cells [78]. Increased SERCA expression in the lungs may decrease elevated cytosolic calcium levels found in diseases associated with airway inflammation and bronchoconstriction.

The well-known cytokine regulators of PLB (TNF-α and IL-13) did not increase the expression of PLB, as has been shown in skeletal and cardiac muscle. In fact, the absence of PLB expression was further confirmed by siRNA knockdown of PLB in airway smooth muscle. Inhibitors of CAMKII affected the enzymatic properties of SERCA, as demonstrated by decreased ATPase activity, and decreased calcium uptake across the SR. A CAMKII agonist had the opposite effect and stimulated the activity of the SERCA pump. Since CAMKII has been found to increase SERCA activation through phosphorylation at

Ser38 in other tissues, this same mechanism of regulation may occur in the smooth muscle of the lungs [78]. These exciting results demonstrate an important mode of regulation for SERCA in pulmonary smooth muscle, where diseases such as asthma lead to impaired calcium reuptake in the SR [79]. CAMKII may prove to be a therapeutic target for SERCA, as many isoforms exists with various tissue specificity and localization. However, CAMKII regulates many other proteins such as the myosin light chain kinase (MLCK) which causes smooth muscle to contract. Given its central location within signal cascade pathways, CAMKII may be prone to unwanted side effects, as discussed previously for SERCA regulation by transcription factors.

Protein Kinase C (PKC)

PKC is a threonine/serine kinase that is activated by diacylglycerol and calcium. This kinase is linked to the β-adrenergic G-protein coupled receptor (GPCR) signal cascade in cardiomyocytes. Recently, it was shown that an inhibitor of PKC causes the upregulation of SERCA2a via the nuclear factor of activated T-cells (NFAT) [80].

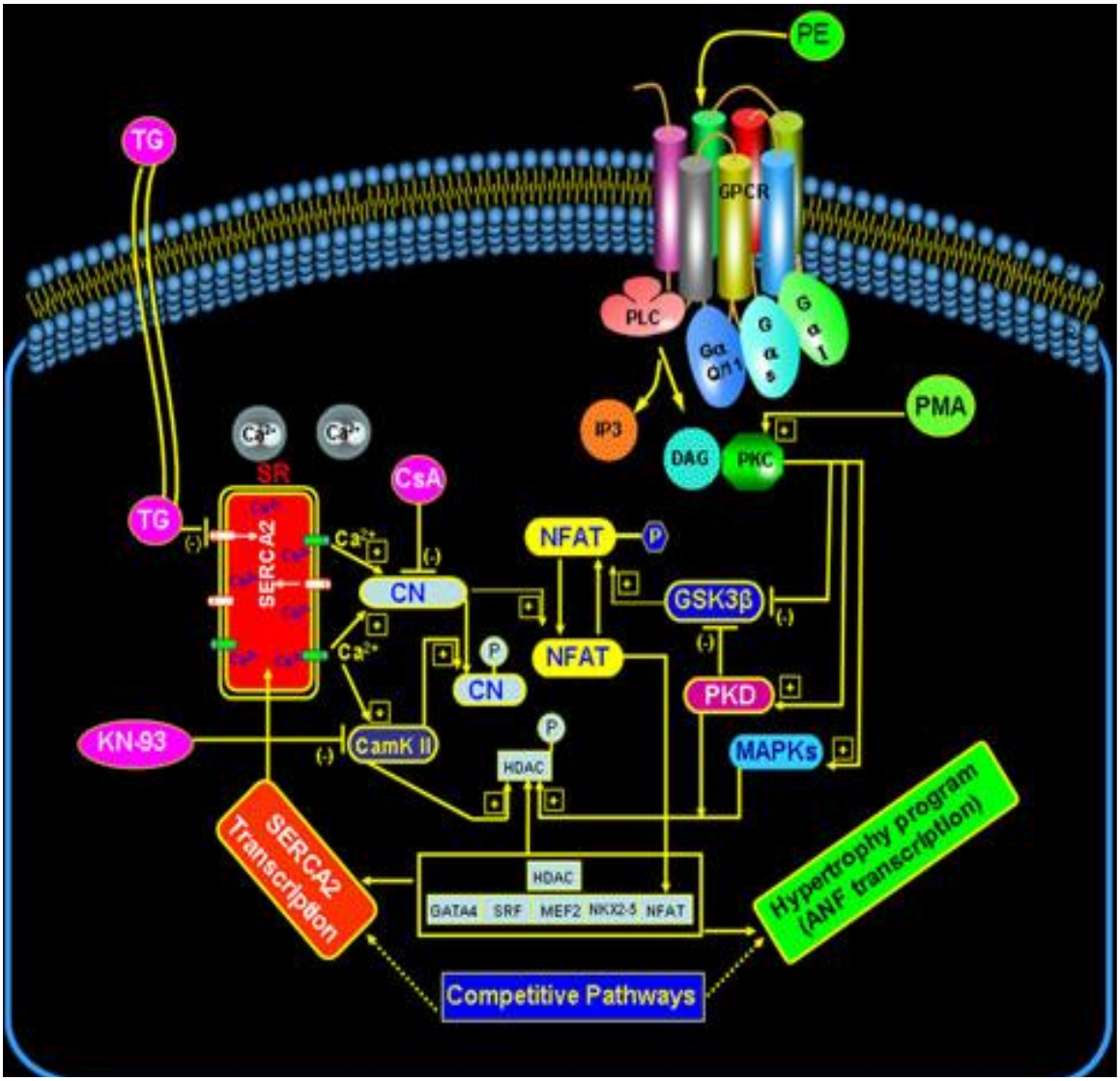

Figure 12. NFAT-calcineurin activation results in increased transcription of SERCA2**.**Thapsigargin (TG) inhibits SERCA and increases cytosolic calcium. Calcineurin (CN) phosphastase is activated in response to elevated cytosolic calcium and activates NFAT. A separate pathway depicts adrenergic stimulation of protein kinase C (PKC), thereby increasing transcription of genes which induce cardiac hypertrophy (downregulation of SERCA expression). Competitive NFAT recruitment from these divergent pathways, differentially alter SERCA content in the heart. Abbreviations: cyclosporine (CsA), diacylglycerol (DAG), Mitogen-activated protein kinase (MAPK), protein kinases D (PKD), histone deacetylases (HDAC), phorbol 12-myristate 13-acetate (PMA), phenylephrine (PE), Glycogen Synthase Kinase (GSK3β). Reprinted from [81].

NFAT is regulated by a phosphorylation from GSK3-beta. Dephosphorylation of NFAT by calcinuerin exposes a nuclear localization signal that shuttles the transcription factor to the nucleus. In the nucleus, NFAT binds regulatory elements at the promoter region of the SERCA2 gene, and up-regulates its expression. The PKC-specific activator

Go¨ 6983 alleviated hypertrophy in cultured neonate rat myocytes, signaling the transcriptional regulator NFAT. NFAT is considered a unique modulator as it is considered a calcium coincidence detector. Multiple upstream elements converge to regulate NFAT and guide its localization (**Figure 12**). This transcription factor has been implicated in numerous disease states such as obesity-linked diabetes. It also has been found to have profound roles in aging through studies on reactive oxidative species, exercise, and the antioxidant resveratrol. This particular PKC activator's role in relieving hypertrophy in cultured rat cardiomyocytes is exciting, suggesting the need for preclinical trials at the level of the whole heart. PKC is involved in numerous physiological processes all throughout the body, but in the heart it modifies the unitary conductance of the gap junction channels by phosphorylation of Ser368 on connexin48 [80]. As such, drug side effects may prove problematic for this particular PKC activator.

Nitric Oxide (NO^-)

NO^- is a small free radical molecule with important roles in the signal cascades within the heart, and has been implicated in many disease states [82]. This powerful vasodilator can pass through the cellular membrane with ease, and is known for its role in activating soluble cGMP, leading to the downstream effects of opening calcium-gated potassium channels. Subsequently, calcium levels are decreased, thereby stopping myosin light-chain kinase (MLCK) from phosphorylating myosin. This leads to extenuated muscle relaxation, and ultimately vasodilation. NO^- also causes S-nitrosylation on cysteine residues of certain proteins, which in turn alter the protein's function (**Figure 13A**). The nitric oxide synthase (NOS) 1 and 3 isoforms have been located to specific regions of the

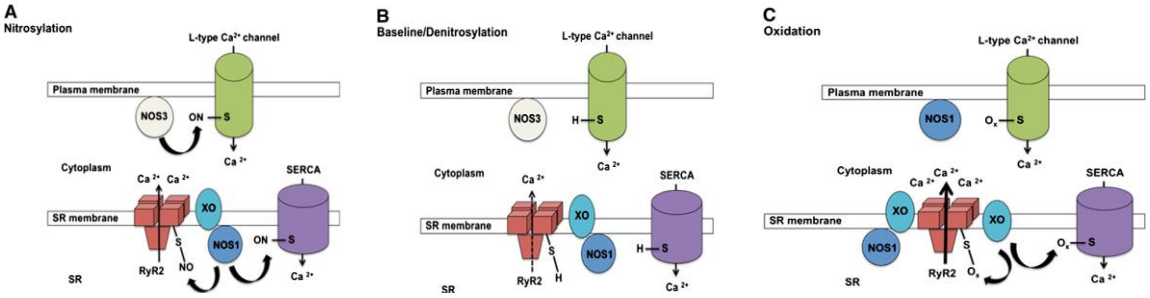

Figure 13. NOS and ROS post-translational modification of SERCA and RYR on SERCA and RYR2. During heart failure NOS is localized to the sarcolemma and causes cysteine nitrolysation on SERCA (activates) and RYR2. Accumulation of reactive oxygen species (ROS) causes xanthine oxidase (XO) to oxidize cysteines which inhibit RYR and SERCA. Reprinted and adapted from [83].

heart. During heart failure and ischemia in mouse models, NOS1 is preferentially localized to the sarcolemma, interacting with caveolin-1, whereas in non-disease states, NOS1 is found at the SR membrane (**Figure 13B**). Myocardial infarction causes NOS1 to localize to the sarcolemma, where it activates SERCA and RYR. As heart failure progress, reactive oxygen species (ROS) accumulate and irreversibly activate RYR2, causing calcium to leak from the SR. Cysteine residues on RYR and SERCA are eventually oxidized by xanthine oxidase and differentially alter their function in comparison to NOS denitrolysation. These powerful enzymes could lead to very specific drug targets, as differential expression between NOS-1 and -3 in particular disease states has also been observed [83].

NO^- is able to form S-nitrosylation reactions at particular cysteine residues on SERCA. These thiol-oxidation reactions have been shown to modify SERCA's function and increase its calcium pumping activity [84]. These reactions are reversible. More deleterious reactive oxygen species such as H_2O_2, O_2^-, NO, or GSNO, can also interact with the very same thiol groups, but irreversibly modify SERCA's pumping ability. It has been suggested that oxidant signaling crosstalk may be important in regulating crossbridge-cycling kinetics. The signaling interplay between ROS and NO^- may also play a pivotal role in maintaining a fine balance between SERCA and the calcium-gated calcium channel

ryanodine receptor (RYR2) in the heart. Fine tuning of the ratio of SERCA to RYR2 could be essential for allowing cardiomyocytes to survive stressful situations, as found in heart disease and failure, and the localization of NOS1 and 3 may aid in this regulation. Drug discovery of specific NOS activators or inhibitors may be particularly beneficial for short-term use to overcome heart failure, but long-term use may not prove to be a viable option. It is notable that NOS knockout mice had a decreased life expectancy after myocardial infarction.

2.3 Known Small Molecule SERCA Activators

Small-molecule activators that either increase SERCA's catalytic turnover rate, or increase the binding affinity of calcium, have been an allusive goal for drug discovery. As elevated calcium levels and altered calcium handling are implicated in numerous disease states, a drug specific for SERCA would be highly beneficial for therapeutics in many diseases where no suitable or highly effective drug currently exists. SERCA has well over 11 isoforms characterized to date, with divergent structural features and kinetic properties. Thus, it should feasible to find isoform specific activators. In fact, one of the most well-known and utilized SERCA inhibitors thapsigargin, displays differential affinity for SERCA's various isoforms [85]. Amongst the current literature only a few known activators exist. One was evaluated in clinical trials for heart failure, but failed to reach its end goals [86].

Disulfiram

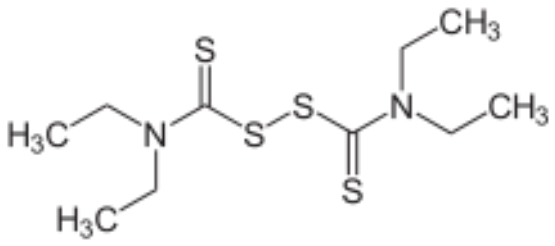

Figure 14. Chemical structure of disulfiram.

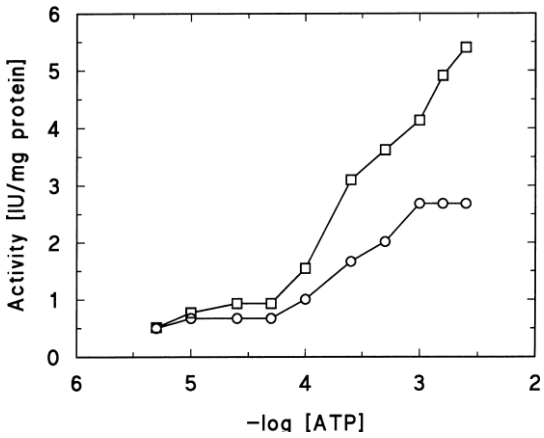

Figure 15. Disulfiram produces an ATP-dependent increase in SERCA's ATPase activity. (O) Control (No disulfiram) and (Squares) 125 μM disulfiram.

Disulfiram is an FDA-approved drug that goes by the name Antabuse, and is used for the treatment of chronic alcoholism (**Figure 14**). It is an acetaldehyde dehydrogenase inhibitor which causes an unpleasant reaction when taken in conjunction with ethanol. The body is not able to metabolize ethanol, leading to a buildup of acetaldehyde. Disulfiram was shown to activate the skeletal-specific SERCA1a, where the addition of 125 μM increased the activity of the enzyme by nearly twofold [87]. Disulfiram also has known interactions with caffeine, acetaminophen, and theophylline. Its FDA description indicates against use in patients with heart failure due to adverse drug interactions and toxicity [88].

Ellagic Acid and Gingerol

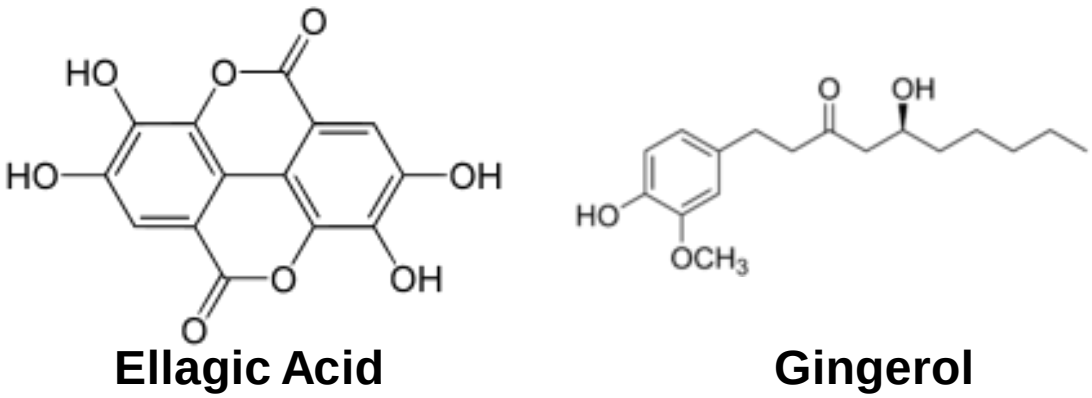

Figure 16. Chemical structures of ellagic acid and gingerol**.**

Ellagic acid is a phenolic constituent in certain fruits such as grapes, strawberries, and blackberries (**Figure 16**). It is an antiproliferative and antioxidative. Gingerol is a polyketide isolated from the rhizome of ginger. Gingerol has also been shown to induce hypothermia, reduce nausea, and alleviate migraines (**Figure 16**). These compounds were originally reported to activate SERCA in sarcoplasmic reticulum vesicles obtained from canine myocardium [89].

Table 1. Ellagic acid and gingerol SERCA ATPase activity

Microsomes	Addition	V_{max}		K_{Ca}		Hill Coefficient
		μmol Ca^{2+}/mg · min	*% Δ*	*μM*	*% Δ*	
Control		1.09 ± 0.10		0.48 ± 0.07		1.47 ± 0.14
Control	**Gingerol**	1.46 ± 0.171	**34**	0.47 ± 0.03	**−2**	1.48 ± 0.08
Control		1.16 ± 0.08		0.64 ± 0.06		1.34 ± 0.13
Control	**Ellagic acid**	1.62 ± 0.181	**40**	0.69 ± 0.09	**8**	1.43 ± 0.07

Gingerol was shown to increase the SERCA's V_{max} by 34%. Ellagic acid increased its V_{max} by 40%, and decreased calcium-affinity (K_{Ca}) by 8% (**Table 1**). A recent study on these compounds, demonstrated that they accelerate the rates of cardiac relaxation and calcium transient decay in the myocardium of mice. These effects were even more pronounced in the myocardium of streptozotocin (diabetes-induced) mouse model. All tests from this study were performed on isolated cardiomyocytes, and currently no data exist on the cross reactivity of the compounds with other channels or ATPases important in heart disease [90]. These compounds have since received a lot of attention, and there is a flurry of preliminary data using these compounds for a wide range of disorders. The two

aforementioned studies highlight the major findings in regard to SERCA and their activator role in various calcium dysregulation-dependent diseases.

According to the American Cancer Society, ellagic acid may reduce the effect of estrogen in promoting the growth of breast cancer cells in tissue cultures. It may also help to remove or break down some cancer-causing substances found in the blood, reduce heart disease, liver problems, birth defects, and even promote wound healing. Gingerol has been shown to suppress colorectal cancer cell growth by inducing apoptosis [91]. Gingerol is an agonist for the TRPV1 and TRPA1 receptors. TRPV1 are known as the vanillinoid receptors, which respond to capsaicin. There are many on-going clinical trials of related synthetic analogues for their use as analgesics in neuromuscular pain and migraines. Gingerol is an ancient herbal medicine which has the ability to activate SERCA [92]. Further validation of gingerol and other synthetic derivative compounds may lead to drugs with specificity for SERCA. Studies need to be performed analyzing their cross reactivity with other ion channels, as non-specific targets could prove problematic for therapeutic use.

Endocannabinoids

A few preliminary studies have demonstrated that endocannabinoids may act as SERCA activators, but most do not discuss the importance of this finding in their studies [93]. Endocannabinoids and synthetically engineered cannabinoids have been shown to be potent neuromodulators with roles in motor learning, appetite, memory formation, and pain sensation. One elegant study on the cross reactivity of iontropic modulators and the RyR1 receptors in skeletal muscle showed that the cannabinoid anandamide (**Figure 17**) induced

a 20% increase in SERCA ATPase activity, which was abolished upon addition of the SERCA inhibitor cyclopianzonic acid (CPA) [94]. The rationale of this study was that these compounds were not able to interfere with CPA's ability to inhibit SERCA, but may be important for mitigating SR leak caused by the RYR1 receptors. This particular study tested the ability of 30 putative modulators of either the plasma membrane K^+, Na^+, or transient receptor potential (TRP) channels to cross-react with intracellular Ca^{2+}-release channels. 43% of the compounds tested were cross reactive with the RYR1 receptors.

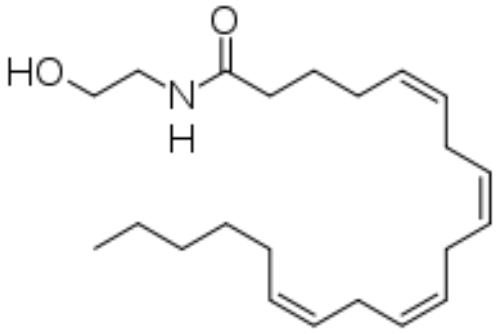

Figure 17. Chemical structure of the endocannabinoid anandamide.

The cannabinoid capsaicin was also found to activate SERCA activity by 13%. Another cannabinoid called Anandamide was found to be a TRP channel modulator, an RyR1 antagonist, modulate other Ca^{2+} channels and play important roles in the mitochondria. It was important to thoroughly investigate the cross-reactivity amongst the many different components important for maintaining calcium homeostasis. Nearly 43% of their findings may have been misinterpreted had the cross-reactivity not been tested [94]. The investigation of K^+ currents by means of patch clamping experiments in rat neuronal cell cultures, showed that ethanolamine (cannabinoid receptor modulator) effected SERCA through a possible stimulatory mechanism. This affect was blocked by the inhibitor thapsigargin [93]. These studies make no claims of the importance of SERCA activation by endocannabinoids, but this mechanism may be relevant for development or maintenance

of many pathological states. These compounds' role in maintaining calcium homeostasis is only now coming to light.

A novel and exciting cannabinoid, the endogenous lipid metabolite *N*-arachidonoyl dopamine (NADA) has been discovered to uncouple SERCA ATPase activity from its calcium pumping ability [95]. This may prove to be an important mechanism that could potentially be a post-mitochondrial strategy to reduce ATP concentrations. Mutations in the RYR1 calcium channel cause excessive heat generation through SERCA stimulation, which is the cause malignant hyperthermia. The role of SERCA in non-shivering thermogenesis through heat dissipation, is only beginning to be understood. This study also makes the conclusion that NADA shifts SERCA toward the structural E1 state, where the SR luminal pathway is closed. They further suggest that NADA decreases Ca^{2+} interaction with the luminal site by directly affecting the luminal sites, or shifting the conformation of SERCA towards the E1 conformation (**Figure 18**). They also tested structurally similar compounds, and described that the requirement of a long chain polyunsaturated fatty acid is needed to achieve an optimal interaction with the pump. The author's primary proposal was that SERCA uncoupling, occurring under conditions of low cytoplasmic Ca^{2+} concentration, may represent an important mechanism for energy interconversion in resting muscle [95].

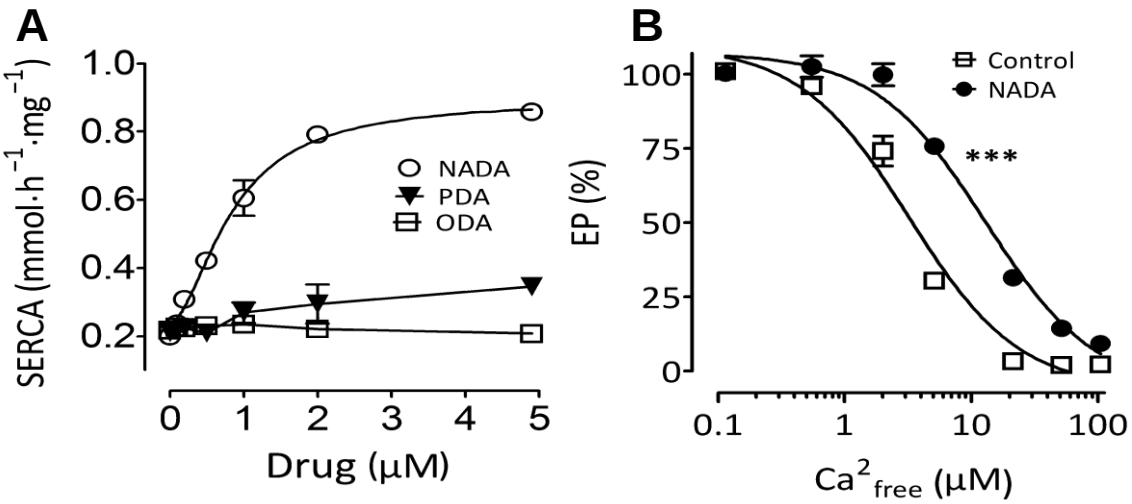

Figure 18. The cannabinoid NADA stimulates SERCA ATP hydrolysis and decreases calcium-affinity**. A.** $Ca2^{+}$-dependent SERCA-mediated ATP hydrolysis was measured in the presence of the indicated concentrations of NADA, *N*-palmitoyl dopamine (PDA), or *N*-oleoyl dopamine (ODA). **B.** NADA reduces interaction of Ca^{2+} with the luminal sites. EP is the amount of SERCA radioactive-labeled phosophoenzyme. Adapted from [95].

These findings on the novel thermogenic drug NADA and the fact that the regulatory protein SLN has also been implicated in uncoupling the ATPase activity of SERCA, demonstrate that SERCA's regulatory mechanisms require more extensive exploration. A recent SLN publication showed that when SLN was lost in high-fat fed mice, they become predisposed to obesity [95]. This knowledge may have implications for Type II diabetes, as obesity is thought to be a crucial factor for its development and progression. The newfound ability of SERCA to produce heat and rapidly deplete the concentration of ATP in the cytosol, shows that it may play important and unexpected roles in a wide range of muscle and metabolic disorders.

Caldaret

The small-molecule caldaret (5-methyl-2-[piperazine-1-yl] benzenesulfonic acid monohydrate; MCC-135) was found to increase SR Ca^{2+} uptake in diabetic rats. It was also shown to decrease SR Ca^{2+} leakage (presumably through the RYR2 receptors), but not in wild-type rats (n=6) [96]. Caldaret (**Figure 19**) exhibited positive lusitropic effects which

could relieve the impaired diastolic function of the heart during failure. Caldaret improved cardiac function during the Langendorff procedure, likely through inhibition of Ca^{2+} overload after an ischemic state. The drug was evaluated in phase I clinical trials. Caldaret showed a good safety profile, but no effect was found on a sample of 387 patients who had experienced a myocardial infarction [97]. The drug was also tested in another clinical trial on 387 patients with severe left-ventricle dysfunction, after myocardial infarction with intervention, and again showed no benefit to the patients [86].

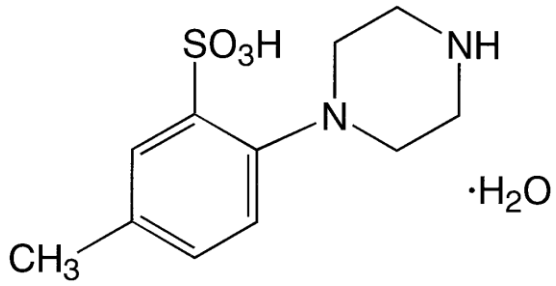

Figure 19. Chemical structure of caldret.

Istaroxime

Istaroxime is a positive inotropic agent that activates RYR2 receptors, inhibits L-Type voltage gated potassium channels, inhibits the Na/K pump, and activates SERCA2a [98]. The inhibition of the Na^+/K^+ pump leads to increased cytosolic $[Ca^{2+}]$. SERCA2a activation improves sequestration of calcium into the SR, causing a corresponding increase in the release of calcium during muscle contraction. This drug holds great promise for the treatment of heart failure as it acts as a luso-inotropic agent, and can simultaneously enhance the diastolic and systolic phases of heart contraction [98]. An increase in the contractility of the heart can be achieved without increasing the heart's energy expenditure. The drug digoxin has similar inotropic properties. Digoxin also

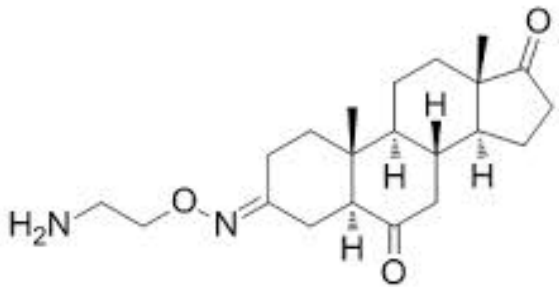

Figure 20. Chemical structure of istaroxime.

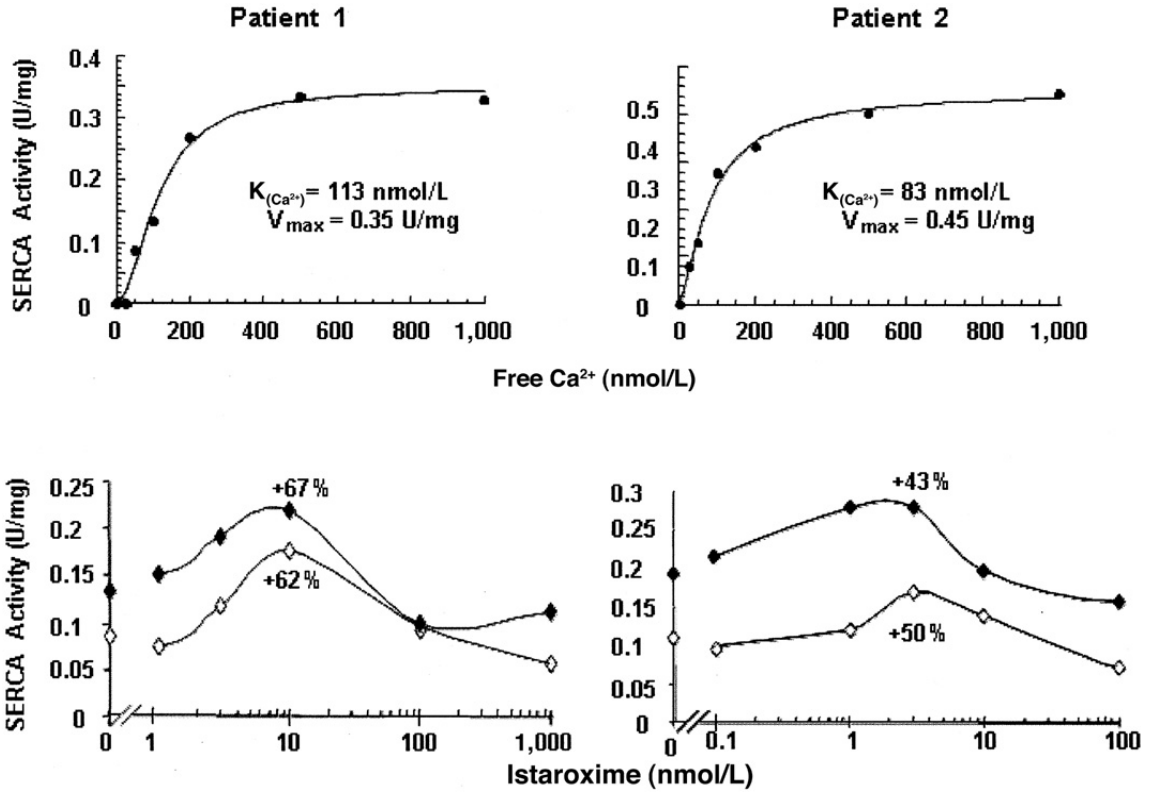

Figure 21. Istaroxime stimulated SERCA2a activity in two human samples**.** Shown are the maximum effective concentrations of 10 and 3 nmol/L. SERCA2a activity was increased by 62% and 67% at 50 and 100 nmol/L free calcium, respectively, in the first preparation and by 50% and 43% in the other preparation. Istaroxime displayed biphasic activation where ATPase activity was reduced at concentrations above 5-10 nmol/L. Reprinted and adapted from [100].

inhibits the Na^+/K^+ pump, and its use has been reserved only for the most severe cases of heart failure. Digoxin has a very narrow therapeutic window, where overdose or toxicity leads to death. Digoxin was once the standard drug for treating congestive heart failure. Recent improvements in β-blockers, and digoxin's negative side effects of hypotension and arrhythmias have made its use fall out of favor [99]. Istaroxime activated SERCA ATPase activity by 17% in hamster models of heart failure [100]. A proposed mechanism suggests that istaroxime activates SERCA by means of inhibiting PLB, as no effect on SERCA activity is found in skeletal muscle preps without PLB. Istaroxime was further found to increase SERCA activity in human samples.

Animal studies using istaroxime have proven very successful in ameliorating various types of heart failure models [101]. Istaroxime seems to overcome the negative long-term effects of classical inotropes. Detrimental side effects such as tachycardia, arrhythmias, and myocardial ischemia have not been observed. The drug's main difference from other Na^+/K^+ inhibitors is its ability to activate SERCA2a. It is likely that the adverse long-term effects, seen with classical inotropes, may be mitigated by stimulating the sequestration of calcium into the SR. [101]. The effect of SERCA stimulation on the heart has been controversial, and some studies have shown an increase in arrhythmias in rats with constitutive overexpression of SERCA2 [102]. It has been suggested that uncontrolled or unregulated SERCA2a overexpression may lead to SR-leak at the RYR2 receptors, because calcium is overloaded in the SR. Some cautioned that induced-by-disease promoters may be necessary in SERCA2a gene therapy clinical trials to reduce arrhythmic effects [102]. In the case of istaroxime, this effect has been suggested to be diminished by achieving a finely tuned balance of calcium back and forth from the cytosol and SR. As more calcium is stored in the SR, more calcium is also released via its inotropic effects without the expenditure of more energy [103]. Many more studies need to be performed to determine whether or not istaroxime would be beneficial for long term therapeutic use.

Istaroxime was recently evaluated in a phase IIb randomized, double-blind, placebo-controlled dose-escalating trial to access acute heart failure in young patients from the ages of 18-25 (HORIZON-HF) [101]. The study concluded that istaroxime use in younger patients decreased pulmonary capillary wedge pressure, increased systolic blood pressure, and decreased diastolic cardiac stiffness. Istaroxime's dual actions now need to

be tested in more severe forms of heart failure, where low cardiac output persists. If istaroxime is capable of restoring myocardial energetics in more severe cases of heart disease and failure, it may prove to be a very powerful drug, especially for patients on a Left Ventricular Assist Device (LVAD) with no other option than a heart transplant.

Istaroxime was well tolerated in phase I/II trials, but the most adverse side effects were gastrointestinal issues and a burning sensation of pain at the site of injection. I.P. delivery of the drug was determined not to be suitable, and new delivery methods via liposomes have been developed [104]. The reason for istaroxime adverse effects are unknown, but it may be due to the cross reactivity of TRP1V, TRP1a, mechanical or temperature sensitive ion channels. The compound seems to cast broad effects, and has numerous targets. In a recent study, 63 derivatives of istaroxime were chemically synthesized, and 3D-QSAR and CoMSIA analysis were performed on each compound. These studies providing insights into chemical structure, and the potency of each for inhibition of the Na^+/K^+ Pump. All of the istaroxime derivatives were tested for their inotropic properties through Na^+/K^+ pump activity assays, but their effect on SERCA activity was not assessed [105]. Unfortunately, the company that owned the compounds was bought out by a large pharmaceutical company, and there are currently no on-going clinical trials.

Conclusion

The calcium pump SERCA may prove to be a very successful target for drug discovery, across a wide range of diseases and disorders. Clinical trials using AAV vectors, initially showed promising results for the treatment of severe heart failure, [106] but the

PhaseIIb results were neutral, showing no positive benefits [59]. New high-throughput drug screening technologies may make it possible to identify novel isoform-specific SERCA activators. SERCA's isoforms are differentially expressed though out the body and they can be used as targets to treat specific diseases such as diabetes, Alzheimer's, asthma, or heart failure. The non-specific interactions with SERCA, found from all currently known pharmacological activators, and protein modulators has proven problematic thus far. It may be important to take careful consideration of the structural and kinetics features of SERCA, when designing activators, or improving on leads identify in drug screens.

Chapter 3 – High-throughput FRET Technology and Assays for Drug Discovery

3.1 Fluorescence Resonance Energy Transfer

Fluorescence resonance energy transfer (FRET) has become a standard tool to detect molecular interactions, and the method has been adapted to a broad range of fields and applications. Fluorescence is typically defined as the absorption of a photon of light by a molecule in the form of electromagnetic radiation and its emission at a longer wavelength. Fluorescence light is emitted at rate of 10^8 s^{-1}, with lower energy than when it was absorbed. The process of fluorescence emission is depicted by a Jablonski diagram in **Figure 22**. A photon is absorbed by a molecule from the ground electronic state (S_0) and its electrons are excited to a vibrational energy of the excited-electronic state (S_1). The electrons rapidly relax (k_V) to the lowest vibrational level of the excited-state through the process of internal conversion. The molecule is brought back to the ground state through non-radiative relaxation or radiative fluorescence emission, occurring within nanoseconds at a rate of $10^{-8}sec^{-1}$(k_F). Non-radiative relaxation is dependent on the environment and dynamics of the excited molecule. Fluorescence emission is the result of the radiative transition to the ground state. A photon is emitted at a longer wavelength (Stokes shift or red shift) because energy is lost due to the fast process of vibrational relaxation. The energy lost through non-radiative rotational and vibrational interactions of the excited state electron colliding with other particles is determined by the equation ($E = hv$). Where E is energy, h is Planck's constant, and v is frequency. The frequency is proportional to the wavelength (λ), and the speed of light (c) because $\lambda = c/ v$. The difference in the energy of

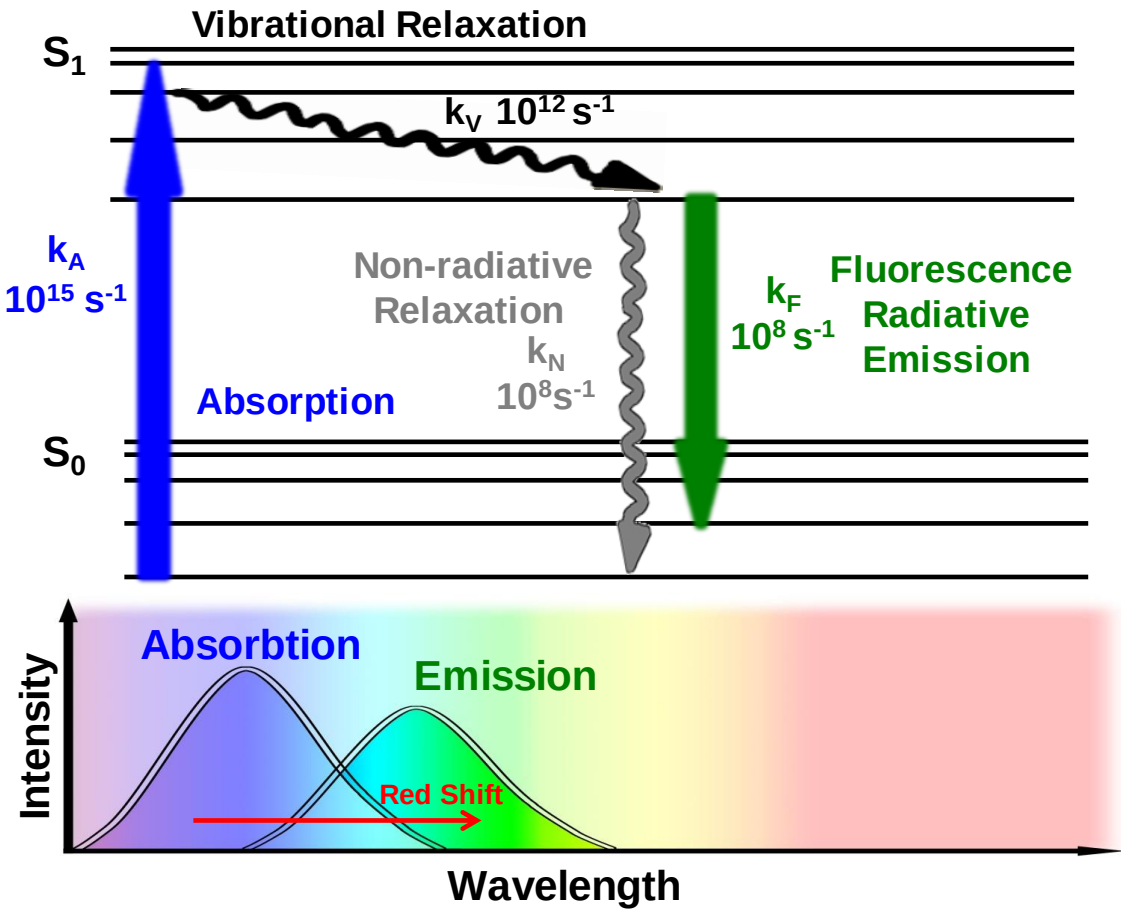

Figure 22. Jablonski diagram. Light is absorbed (blue arrow) as a high energy photon from the S_0 state, and the system is excited electronically and vibrationally to the S_1 state. The system vibrationally relaxes to the lowest excited energy state through non-radiative (gray arrow) and radiative processes (fluorescence, green arrow). Energy is lost through vibrational relaxation, so the emitted photon is red shifted, and fluoresces at a longer wavelength.

the absorbed photon, and emitted fluorescence photon results in the longer wavelength of the emitted photon [107].

The number of photons emitted can be determined by calculating the quantum yield (ϕ_F) in (Eq. 1). The quantum yield reflects the number of photons emitted (k_F) over the number of photons absorbed $(k_F + k_{NR})$, and is dependent on the rates associated with each relaxation process.

$$\phi_F = \frac{k_F}{(k_F + k_{NR})} \qquad \text{(Eq. 1)}$$

FRET occurs by the transfer of non-radiative energy between dipole-dipole interactions, typically between a shorter wavelength donor molecule, in the excited electronic state, to a longer wavelength acceptor molecule in the ground state (**Figure 23**). The probability that energy transfer will occur depends on the spectral overlap between the emission and absorption spectra of the donor and acceptor, the fluorescence quantum yield of donor, the molar absorptivity (extinction coefficient) of the acceptor, and the distance and orientation of the dipole interaction. The probability of energy transfer is defined as FRET efficiency (E), which is directly proportional to the rate of energy transfer (k_T) and the R^{-6} distance dependence of the donor and acceptor. The Forster distance (R_0) shown in (Eq. 2) is the distance between a particular donor-acceptor FRET pair, at which the probability of FRET efficiency is 50%.

$$R_0 = 9{,}790\left[J(\lambda)\kappa^2\eta^{-4}\phi_D\right]^{1/6} \qquad \text{(Eq. 2)}$$

The Forster distance (R_0) is defined by the area of overlap between the donor emission and acceptor excitation fluorescence spectra $J(\lambda)$, the relative orientation of the transition dipoles of the donor and acceptor κ^2, the quantum yield of the donor ϕ_D (not in the presence of the acceptor), and the refractive index of the medium η. The orientation factor (κ) is usually assumed to be equal to 2/3. This is appropriate for donor and acceptor pairs attached by flexible linkers, where motion is dynamic, and not sterically restricted. R_0 is most affected by the overlap integral $J(\lambda)$ of a particular FRET pair.

The rate constants of radiative donor fluorescence emission (k_D) and non-radiative resonance energy transfer (k_T) to the acceptor are inversely proportional, and can be used

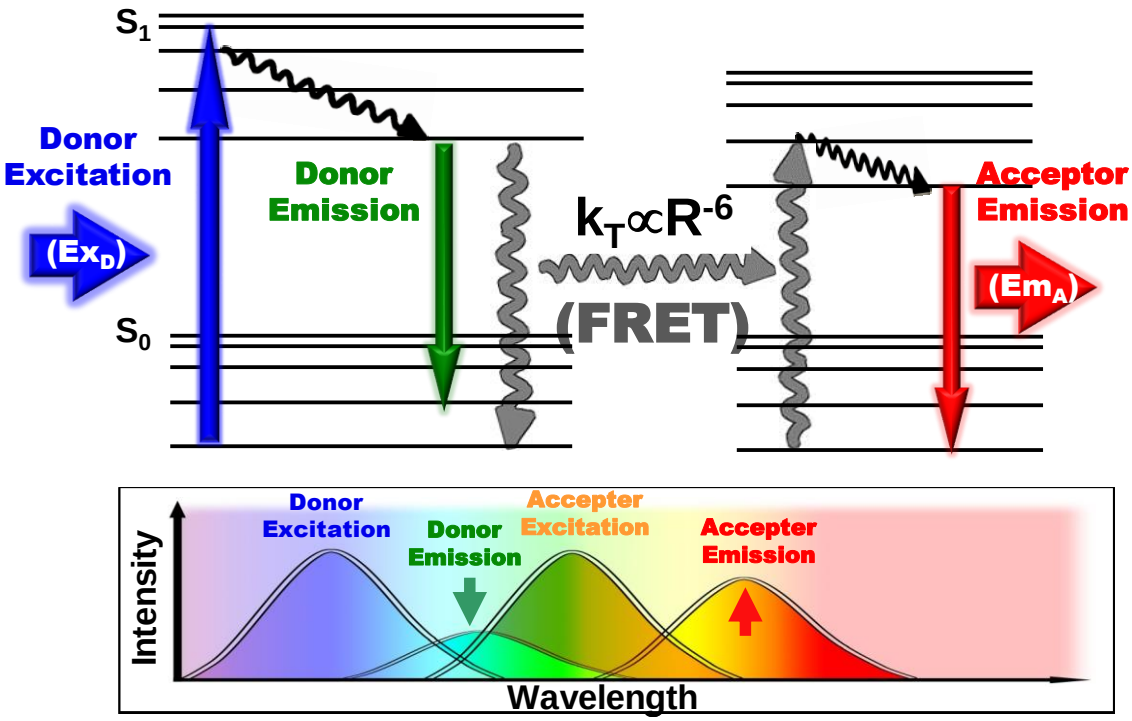

Figure 23. Fluorescence resonance energy transfer (FRET) diagram. FRET is the non-radiative energy transfer from an excited donor molecule to an acceptor molecule. The rate of energy transfer (k_T) is dependent on the distance (R) between the donor and acceptor fluorophores by an inverse power of the sixth.

to determine the distance (R) between donor and acceptor molecules (Eq. 3). The efficiency of energy transfer, or the probability that energy will be transferred to an acceptor will be low, if the rate of radiative emission from the donor molecule is faster than the rate of energy transfer.

$$k_T = k_D \left(\frac{R}{R_0}\right)^{-6} \qquad \text{(Eq. 3)}$$

The ability to determine the distance between two fluorescent probes allows FRET to be used as a powerful tool to determine molecular interactions, and directly quantitate the measurement in terms of distance and possibly orientation. The sensitivity of FRET is determined by the Forster distance (R_o), and is highest when the distance between the donor and acceptor probes is near R_o. As shown by **Figure 24**, when the FRET

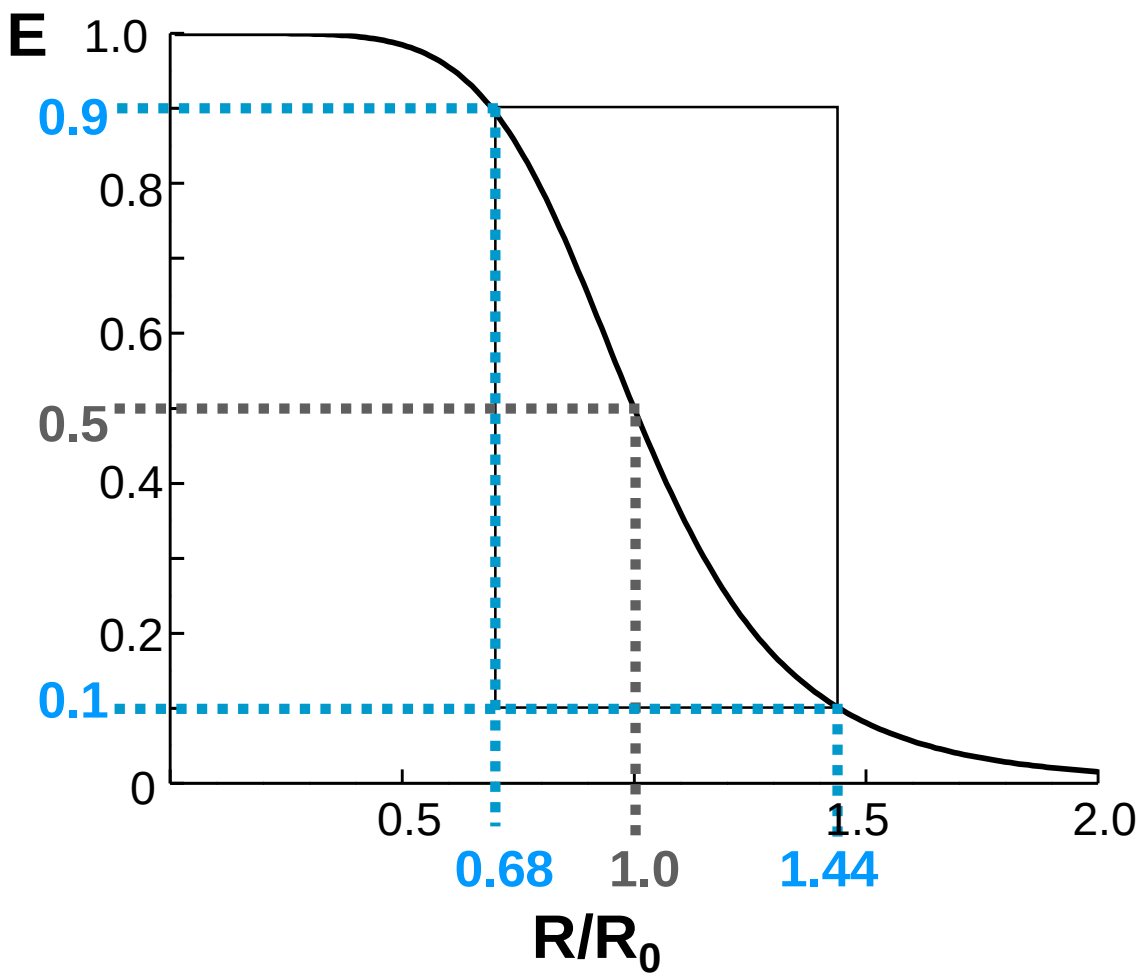

Figure 24. Universal FRET plot. The efficiency of energy transfer (E) is dependent on the Forster distance (R_0), and the distance (R) between the donor and acceptor fluorescent probes. The dynamic range of FRET is most sensitive when the distance measured is close to the Forster distance, shown in blue.

efficiency is 50%, the dynamic range that can be observed is the largest. At 50% FRET efficiency, half of the donor molecules decay by energy transfer to the acceptor, and half decay by the radiative and non-radiative rates.

3.2 Fluorescence Lifetime

The measurement of fluorescence emission is generally described as being determined by steady-state intensity methods or from the fluorescence lifetime. For steady-

state determination of FRET, the fluorescence intensity from the donor-acceptor (F_D) is compared to the donor-only sample (F_D), as shown in (Eq. 4).

$$E = 1 - \frac{F_{DA}}{F_D} \qquad \text{(Eq. 4)}$$

Most approaches utilize steady-state fluorescence measurements to determine FRET efficiency, and monitor fluorescence emission as the peak intensity from one or two fluorescence wavelengths. These types of measurements tend to lack precision and resolution, yielding single-point average FRET and distance determinations.

Fluorescence lifetime measurements are resolved by using time-resolved fluorescence measurements to determine the rate of fluorescence emission decay. These measurements are more precise than steady-state fluorescence because the fluorescence intensity is resolved over multiple time points. Fluorescence lifetime is defined as the average time a excited-molecule stays in the excited-state, or more specifically for a single-exponential decay, when 63% of the molecules have decayed prior to $t = \tau$ and 37% decay at $t > \tau$. Where τ is the fluorescence lifetime and t is time. Fluorescence lifetime is dependent on the radiative fluorescence emission from the excited state (k_F). The rate of fluorescence decay from a donor molecule is $k_D = 1/\tau_D$. The rate of fluorescence decay of donor molecule in the presence of an acceptor undergoing FRET is equal to the rate of radiative fluorescence emission (k_F) and non-radiative energy transfer to the acceptor (k_T), so $k_{DA} = k_F + k_T$. Substituting these rate constants into Eq. 3, and rearranging the equation yields a simplified equation (Eq. 5), useful for determining FRET efficiency from lifetime measurements of a donor-only sample and a FRET sample (donor-acceptor).

$$E = 1 - \frac{\tau_{DA}}{\tau_D} \qquad \text{(Eq. 5)}$$

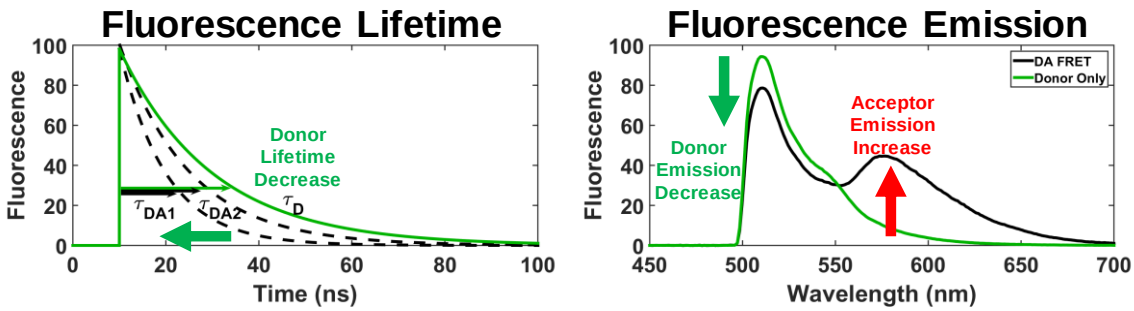

Figure 25. Fluorescence lifetime and steady-state FRET. The intensity decay rate determines the fluorescence lifetime as shown on the left plot. The donor lifetime τ_D (green curve) decreases in the presence of an acceptor due to FRET (black dashed curves). Multiple states τ_{DA1} and τ_{DA2} can be resolved from a single lifetime measurement. The fluorescence emission spectrum shown on the right depicts the decrease in donor fluorescence and increase in acceptor fluorescence due to FRET.

Fluorescence lifetime is typically determined by analyzing the donor lifetime. A key advantage of lifetime in comparison to steady-state measurements is that the intensity decay curve can be used to resolve multiple populations (**Figure 25**). Multi-component fluorescence lifetime analysis of properly placed FRET pairs, is useful for determining multiple distances of a dynamic equilibrium of structural states. The information provided from these high-resolution measurements will be described in more detail in Chapter 5, in the context of drug discovery for SERCA small-molecule effectors using FRET-based biosensors.

3.3 Fluorescent Proteins

Fluorescent proteins (FP) were first isolated from the *A. victoria* jellyfish [108]. The discovery of fluorescent proteins completely changed the biomedical sciences, by allowing scientists to label proteins and track their movement, function, and behaviors. The continuously expanding palette of fluorescence proteins now extends across the visible spectrum. Longer wavelength FP variants have been isolated from the marine anemone *Discosoma* and other *Anthozaon* coral [109]. The fluorescent properties of each

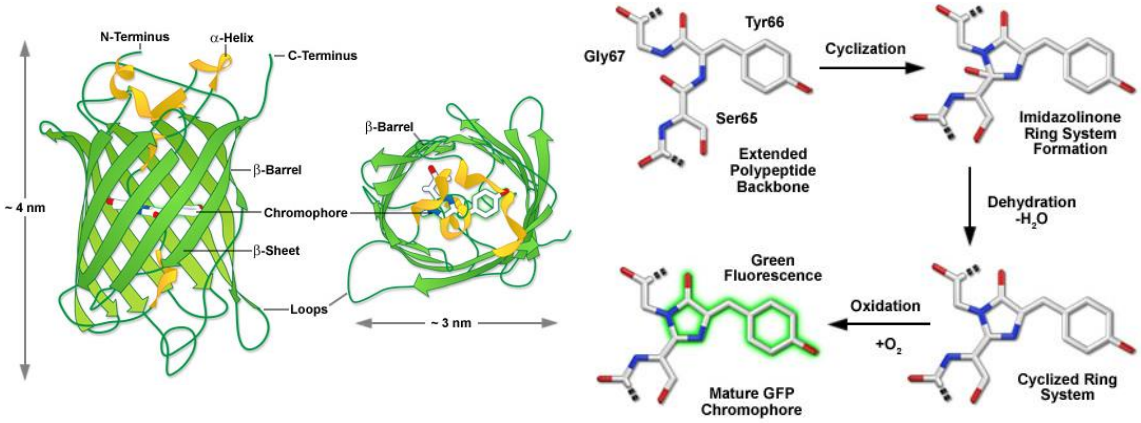

Figure 26. Structure and chromophore of GFP. GFP's structure contains 11-beta strands forming a rigid, hydrophobic beta-barrel, surrounding a core alpha-helix. Three residues Ser65, Gly67, and Tyr66 form the chromophore, and catalyze the cyclization and oxidation reactions responsible for a mature fluorescent protein. Adapted from [111]

FP have been dramatically improved through genetic mutations which improve brightness, photostability, and maturation [110].

FP's weigh ~27 kD and they have a rigid beta-barrel structure consisting of 11 beta-strands surrounding a core alpha-helix. Three amino-acids Ser65, Gly67, and Tyr66 are involved in the reaction that results in the conjugation of the imidazoline ring, and subsequently fluorescence emission (**Figure 26**). First, a nucleophilic substitution of the amino group of Gly67 onto the carbonyl group of Ser65 occurs, followed by elimination of water, and the formation of an imidazolidinone ring. Tyr66 is then oxidized, and results in a large delocalized pi-system [111].

The successful engineering of a broad range of FPs has made it possible to develop genetically-encoded FRET biosensors, targeted to specific locations within a cell, and responsive to ligand-binding. FRET-based biosensors are now being utilized for high-throughput drug screening. The live-cell biosensors that will be presented in Chapters 4 & 5 were developed using cyan, green, yellow, and red fluorescent proteins.

Chapter 4 – Spectral Unmixing Plate Reader

Spectral unmixing plate reader: high-throughput, high-precision FRET assays in living cells

Tory M. Schaaf[1], Kurt C. Peterson[2], Benjamin D. Grant[2],
David D. Thomas[1, 3], and Gregory D. Gillispie[2,*]

[1]Department of Biochemistry, Molecular Biology and Biophysics, University of Minnesota, Minneapolis, Minnesota 55455
[2]Fluorescence Innovations Inc., Minneapolis, MN 55455
[3]Photonic Pharma LLC, Minneapolis, MN 55410

Adapted from:
Schaaf TM, Peterson KC, Grant BD, Thomas DD, Gillispie GD. Spectral Unmixing Plate Reader: High-Throughput, High-Precision FRET Assays in Living Cells. J Biomol Screen. 2016 Nov 22. pii: 1087057116679637. [Epub ahead of print]

Author Contribution Statement:

TMS designed experiments, performed experiments, analyzed data, and wrote the manuscript. KCP and BDG built the fluorescence plate reader, and wrote software for plate reader data acquisition and analysis. GDG, BDG, and DDT contributed to experimental design, and edited the manuscript.

4.1 Summary

We have developed a microplate reader that records a complete high-quality fluorescence emission spectrum on a well-by-well basis under true high-throughput screening (HTS) conditions. The read time for an entire 384-well plate is less than 3 minutes. This instrument is particularly well suited for assays based on fluorescence resonance energy transfer (FRET). Intramolecular protein biosensors with genetically encoded GFP donor and RFP acceptor tags at positions sensitive to structural changes were stably expressed and studied in living HEK cells. Accurate quantitation of FRET was achieved by decomposing each observed spectrum into a linear combination of four

component (basis) spectra (GFP emission, RFP emission, water Raman, and cell autofluorescence). Excitation and detection are both conducted from the top, allowing for thermoelectric control of the sample temperature from below. This spectral unmixing plate-reader (SUPR) delivers an unprecedented combination of speed, precision, and accuracy for studying ensemble-averaged FRET in living cells. It complements our previously reported fluorescence lifetime plate reader, which offers the feature of resolving multiple FRET populations within the ensemble. The combination of these two direct waveform-recording technologies greatly enhances the precision and information content for HTS in drug discovery.

4.2 Introduction

Numerous live-cell FRET biosensors based on genetically encoded fluorescent fusion proteins have been developed, but their application in high-throughput screening (HTS) assays is uncommon. An intramolecular FRET sensor for sarco/endoplasmic reticulum calcium ATPase (SERCA) [112-114] is a rare exception [114]. This two-color SERCA (2CS) biosensor, expressed in HEK293 cells, employs eGFP and tagRFP (further referred to as GFP and RFP) fluorescent proteins [115]. Fluorescent proteins were engineered at carefully selected locations on SERCA's cytoplasmic headpiece domains. The headpiece domains are known to undergo large-scale structural changes as ATP hydrolysis fuels the active pumping of calcium from the cytosol into the endoplasmic reticulum. The interactions of small molecules with SERCA produce measurable changes in intramolecular FRET that correlate with function, making this structure-based biosensor a powerful tool for the discovery of novel drugs related to calcium homeostasis.

The previous development of a novel fluorescence lifetime readout in the nanosecond time domain was shown to enable rapid and reliable identification of small-molecules that affected FRET in the two-color SERCA (2CS) biosensor [114, 116-118]. Conventional microplate readers, which measure fluorescence intensity, lack the precision required for reliable observation of the typically small FRET changes associated with allosteric effectors in live-cell assays. Similarly, the throughput of related fluorescence technologies such as microscopy is too low, and the precision of flow cytometry is currently too low for large-scale library screening [119, 120]. The technological advances of direct waveform recording (DWR) led to the development of a novel fluorescence lifetime plate reader in the time domain [116], and now have been applied to the wavelength-domain. This new spectral unmixing microplate reader rapidly and accurately records the entire fluorescence emission spectrum.

The quality of the acquired spectral data enables a simple and direct decomposition of the observed spectra into linear combinations of component spectra (spectral unmixing), yielding accurate and precise FRET efficiency values. The benefits are critically evaluated by coupling fluorescence lifetime detection with the complementary spectral recording to further optimize the precision of FRET measurements for high-throughput screening. The combination of the spectral and fluorescence lifetime readouts represents a promising screening platform for detecting small changes in FRET.

This study emphasizes live-cell biosensors, but the same approach is equally applicable to purified proteins labeled with dyes [61]. In addition to drug discovery activities, the spectral recording technology has high potential for a wide range of

biological applications, such as binding studies, analytical biochemistry, and molecular diagnostics.

4.3 Materials and Methods

Cell Culture

HEK293 cells were maintained in phenol-red-free DMEM from Gibco (Waltham, MA) supplemented with 2 mM GlutaMAX (Gibco), 10% fetal bovine serum (FBS) from Atlanta Biologicals (Lawerenceville, GA), and 1 IU/mL penicillin/streptomycin (Gibco) and grown at 37° C with 5% CO_2. Stable clones expressing the FRET biosensors and corresponding donor- and acceptor-labeled control cell lines were established as described previously [114]. Briefly, cells were transfected with the recombinant DNA following established protocols lipofectaimine 3000 from Invitrogen (Carlsbad, CA). 48 hours post transfection the cells were placed under G418 (500 µg/mL) from Sigma (St. Louis, MO), selection, and plated to allow for the growth of single colonies. Clones were isolated 2-3 weeks after transfection and antibiotic selection. The stability of each clone was assessed by flow cytometry and confocal microscopy (data not shown). The cell lines were expanded in T225 flasks from Corning (Corning, NY), harvested by treatment with Tryple (Invitrogen), washed three times in phosphate buffer solution (PBS) with no magnesium or calcium Thermo Fischer (Waltham, MA)) and centrifuged at 300 g, filtered using 70 µm cell strainers (Corning), and diluted to 10^6 cells/mL using an automated countess cell counter from Invitrogen. In studies with cyan and yellow fluorescent protein biosensors, transient transfections were performed. In these studies, cells were harvested and prepared

as described above, 48 hours after transfection. Cell viability was assessed using trypan blue.

Cell and drug liquid dispensing

Cells were dispensed using a Multidrop Combi liquid dispenser from Thermo Fischer (Pittsburg, PA) at a density of 10^6/mL. Compounds were diluted in DMSO and dispensed either using a Mosquito liquid handeler from TTP Labtech (Melbourn, UK) or a Mantis liquid dispenser from Formulatrix (Bedford, MA). The known SERCA inhibitors thapsigargin (TG, Sigma), 1,4-dihydroxy-2,5-di-tert-butylbenzene (BHQ) from Tocris (Minneapolis, MN), and cyclopiazonic acid (CPA, Tocris) were diluted at 50X concentrations and subsequently serially diluted in 96-well mother plates prior to liquid dispensing. Cells and drug mixtures were dispensed into 384-well flat, black-bottom polypropylene plates from Greiner (Kremsmünste, Austria) and incubated for 20 min at room temperature (20-23 ℃), unless otherwise noted.

Instrumentation overview

Figure 27A is a schematic drawing depicting key features of the fluorescence plate-reader platform. The lifetime and spectral readout experiments presented here were conducted with separate instruments at 20°C, but both modes can be incorporated into a single instrument, and work along these lines is in progress. Simultaneous acquisition of the lifetime and spectral data is also feasible. The photomultiplier tube (PMT) and digitizer are as described previously [116], but this new instrument employs epi-illumination excitation and detection from above, which facilitates implementation of temperature control.

In its spectral unmixing plate reader (SUPR) mode, the instrument provides direct high-throughput detection of the complete fluorescence emission spectrum, (emission vs wavelength), with excitation provided by a 473 nm continuous wave laser. Spectra are recorded using a grating-based fiber optic input spectrograph equipped with linear-array CCD detector (Sony ILX511B). The recorded wavelength range in these experiments spanned the entire visible spectrum, but only the 400-700nm range was used in the data analysis. In lifetime mode, the full nanosecond-resolved fluorescence emission waveform is acquired following excitation with a 473 nm pulsed microchip laser. The acquisition time per well is typically 200 ms in either spectral or lifetime mode (**Figure 27A**).

Time-resolved FRET acquisition and analysis

Fluorescence decay waveforms for lifetime determination, were detected directly as previously described [114, 116]. The 473 nm passively Q-switched microchip laser (Concepts Research Corporation, Belgium, WI) delivers highly reproducible, and high-energy pulses (~1 μJ) at 5 kHz repetition rate. A full fluorescence decay waveform was detected in response to each laser pulse over a 128 ns time window, using a photomultiplier module from Hamamatsu (Cat# H10720-210), and a proprietary transient digitizer from Fluorescence Innovations (Minneapolis, MN). A 488 nm long-pass filter from Semrock (Rochester, NY) and 517/20 bandpass emission filter (lifetime mode), were used, ensuring that only emission from the GFP donor was detected. A 488 nm dichroic mirror directed fluorescence signal toward the PMT (lifetime mode) or spectrograph (spectral mode) using a fiber optic cable.

The observed donor fluorescence waveform $F_D(t)$ was analyzed using least-squares minimization global analysis software [116] and fitted (Eq. 6) by a simulation $S_D(t)$,

consisting of a n-exponential decay model $M_D(t)$ (characterized by pre-exponential factors A_i and lifetimes τ_{Di}), convolved with the instrument response function IRF(t), acquired by recording scatter from 0.31 µm latex microsphere suspensions (Thermo Fischer).

$$M_D(t) = \sum_{i=1}^{n} A_i \exp(-t/\tau_{Di}) ,$$
$$S_D(t) = \int_{-\infty}^{+\infty} IRF(t-t')\, M_D(t')\, dt' \qquad \text{(Eq. 6)}$$

For initial analysis, a single-exponential model (n = 1) was assumed, and FRET (efficiency) was calculated from (Eq. 7).

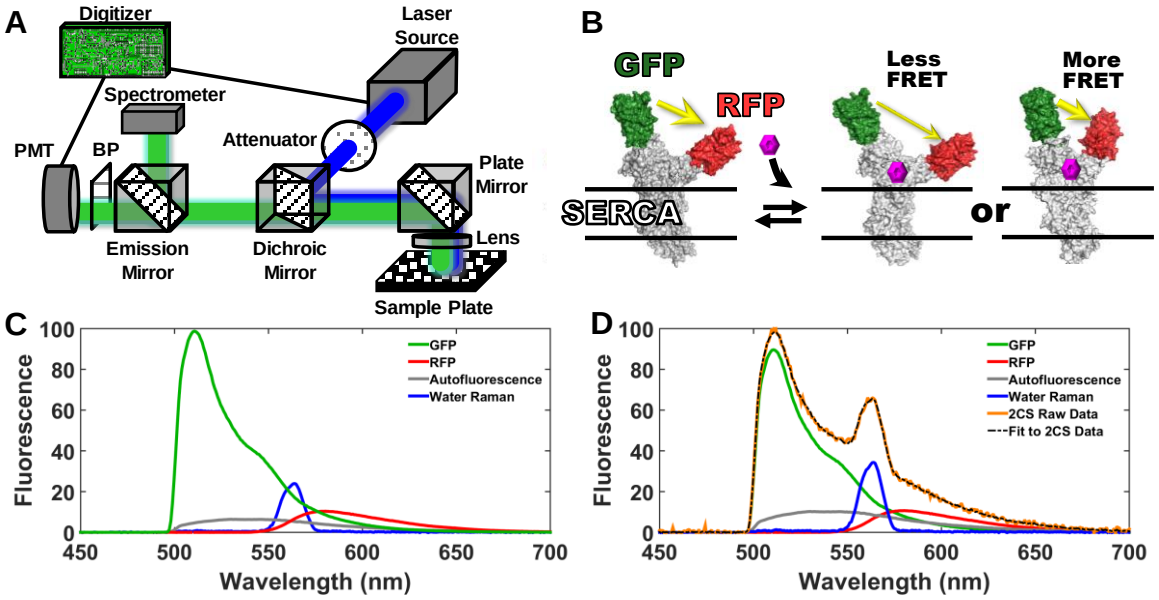

Figure 27. Overview of spectral unmixing plate reader technology and methods. (**A**) Diagram of the instrument, which provides high-throughput detection of the emission spectrum or lifetime (time-dependent decay). A 473 nm laser (continuous wavelength for spectrum, microchip pulsed for lifetime) excites the sample, and the spectral (fluorescence vs. wavelength) or lifetime (fluorescence vs. time) waveform is recorded directly using a photomultiplier tube (PMT) coupled to a proprietary digitizer or spectrograph, respectively. (**B**) The two-color SERCA (2CS) FRET biosensor, expressed in HEK293 cells, enables measurement of FRET between green (GFP) and red (RFP) fluorescent proteins, positioned at optimized locations on SERCA[112-114]. As depicted, FRET efficiency depends on the structural status of SERCA's domains. (**C**) Reference fluorescence emission (basis) spectra corresponding to one-color SERCA (GFP or RFP), cellular autofluorescence, and water Raman (inelastic light scattering), normalized to GFP. These basis spectra were used to analyze the spectra of cells expressing 2CS (**D**), to decompose the observed spectrum of 2CS (orange) into a linear combination of component spectra (best fit shown in dashed black, components shown with same color scheme as in C), thus permitting accurate quantitation of the GFP (donor) and RFP (acceptor) fluorescence needed to calculate FRET (13.7% for data shown in D, with SD = 0.11%), using (Eq. 9). Complete emission spectra from 500-700 nm were acquired in less than 3 minutes for a full 384-well plate.

$FRET = 1-(\tau_{DA}/\tau_D)$ (Eq. 7)

Where τ_{DA} is the lifetime of the intramolecular FRET biosensor, and τ_D is the lifetime of the corresponding donor-only cell line. The fluorescence lifetime of eGFP from a single-exponential fit of the donor-only control was 2.58 ± 0.02 ns **(Figure S38)**, in agreement with reported values [121].

Spectral FRET acquisition and analysis

The fluorescence spectra were recorded with a fiber-optic spectrometer. The uncooled linear array detector offers higher data density (pitch) compared to the multimode PMTs, that have more commonly been used for spectral unmixing in fluorescence microscopy [122]. The linear array detector is also substantially smaller, and less costly compared to a TE-cooled 2-dimensional scientific grade CCD camera.

The observed fluorescence emission spectrum F(λ) was fitted by least-squares minimization to a linear combination of component spectra

$$F_{Fit}(\lambda) = aF_D(\lambda) + bF_A(\lambda) + cF_C(\lambda) + dF_W(\lambda) \quad \text{(Eq. 8)}$$

where D is donor, A is acceptor, C is cell autofluorescence, and W is water Raman, and *a*, *b*, *c*, *d* are the weighting (scalar) coefficients determined from the fit. The fitted spectrum for each well was determined using least squares minimization with Matlab (Mathworks) to solve for the scalar coefficients (Eq. 8).

For an intramolecular FRET sensor with a 1:1 ratio of donor D and acceptor A molecules, FRET efficiency (FRET) was determined from (Eq. 9).

$$FRET = \frac{FR \times QR - AR}{1 + FR \times QR}, \quad \text{(Eq. 9)}$$

Where QR is the ratio of quantum yields (Q_D/Q_A) in the absence of FRET, AR is the ratio of molar absorptivity ($\varepsilon_A/\varepsilon_D$), both obtained from reported values [123]. QR was corrected for spectrometer sensitivity at the appropriate wavelengths (**Figure S36**). The only experimentally observed variable in (Eq. 9) becomes the fluorescence ratio (FR).

$$FR = \frac{Acceptor\ fluorescence}{Donor\ fluorescence} = \frac{bF_A}{aF_D}. \qquad \text{(Eq. 10)}$$

A full derivation of (Eq. 9) is in Supplementary Data.

4.4 Results

Two one-color stable cell lines expressing GFP-SERCA or RFP-SERCA were developed as controls for analysis of 2-color FRET spectra. Reference (basis) spectra from these cell lines, untransfected cells (water Raman plus cell autofluorescence), and buffer solution (water Raman) were acquired using a detector integration time of 100 ms, for each well of a 384-well plate. The GFP-only reference spectrum was corrected for autofluorescence and water Raman contributions (**Figure S33**,**Figure S34**). The RFP-only spectrum was acquired by excitation at 532 nm (**Figure S35**), under which conditions the Raman and autofluorescence signals were negligible. Each of the four reference spectra was quite reproducible, so that a single set of reference spectra, acquired only one time, was used to decompose or unmix the component spectra from the observed fluorescence emission spectrum in 2CS samples for over six months. Reference spectra are superimposed in **Figure 27C,** normalized to the peak intensity of the GFP sample. The RFP spectrum shown corresponds to the intensity observed with excitation at 473 nm. Spectral unmixing (Eq. 8) resolved the distinct components of GFP and RFP for quantitative determination of the apparent FRET (Eq. 9),(Eq. 10). **Figure 27D** illustrates

the analysis of a sample of cells expressing the 2CS biosensor, showing the observed spectrum (orange) and the best fit (dashed black) to the four components, yielding a FRET value of 13.7% (SD = 0.11%).

Spectral unmixing of GFP and RFP live-cell mixtures

Accuracy and precision of the spectral unmixing method was verified by analyzing known mixtures of GFP- and RFP-expressing HEK293 cell lines, dispensed at 10^6 cells/mL into a 384-well plate. The GFP-only control cell line was mixed with cells expressing the RFP-only control construct to produce wells with the percentage of GFP increasing in 10% increments. The total volume per well was 50 µL. The expression of the RFP-only cell line was five times that of the GFP-only cell line, as determined by quantitative western blotting. The observed spectra (raw data) show a uniform decrease in the GFP contribution (500-550 nm region) **(Figure 28A)**.

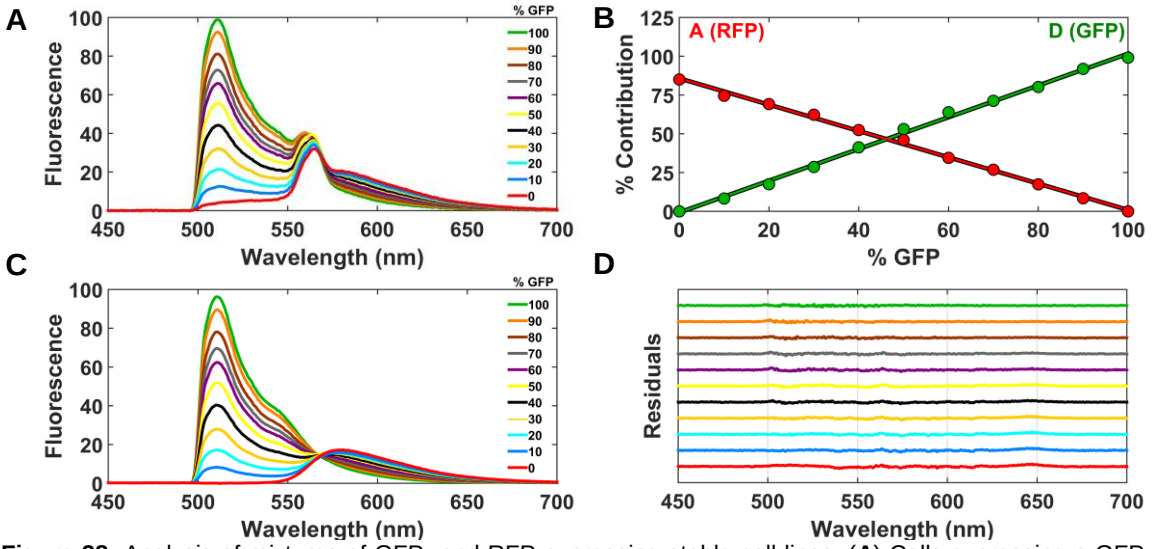

Figure 28. Analysis of mixtures of GFP- and RFP-expressing stable cell lines. (**A**) Cells expressing a GFP-only control construct were mixed with cells expressing a RFP-only control construct in a 384-well plate. The % of GFP cells was varied as indicated, but the total volume and number of cells remained constant. The observed spectrum of each GFP mixture is shown (average from 32 wells). Each observed spectrum was fit using linear least-squares minimization to determine the four scalar coefficients (Eq. 8), and the results are plotted in (**B**), showing that the fluorescence contributions of GFP and RFP to the emission spectrum vary inversely and linearly. (**C**) shows the results of A after subtracting contributions from autofluorescence and Raman. (**D**) shows the residuals from fits in B, offset vertically for clarity.

The individual scalar coefficients from the fluorescence emission spectrum of each mixture were assessed as described in (Eq. 8). The scalar coefficients of GFP (D) and RFP (A) were converted to fluorescence signal by multiplying by the total emission from the corresponding reference spectra (F_{RFP} and F_{GFP}) using (Eq. 9),(Eq. 10). The contributions of GFP (D) and RFP (A) increased inversely and linearly as expected. The contribution from cellular autofluorescence and water Raman remained constant across the GFP/RFP live-cell gradient (**Figure 28B**) and were subtracted from the spectrum of each mixture (**Figure 28C**). An isoemissive point at 567 nm, clearly distinguishes the change in GFP and RFP emission across the gradient of cellular mixtures. The residuals obtained using the four-component model (Eq. 8) are plotted for each %GFP mixture in **Figure 28D**. The residuals remain flat, demonstrating excellent agreement between the fit and observed spectrum (Eq. 8).

The scalar coefficients were used to determine the contribution of each component to the total fluorescence signal. At the lowest mixture of cells expressing GFP (10% GFP), there are approximately 5,000 GFP-expressing cells and 45,000 RFP-expressing cells per well (50 µL total volume per well). Based on the diameter of the laser beam (500 microns), well dimensions, and diameter of one cell, we estimate approximately 500 cells expressing GFP contribute to the observed spectrum. As such, we have performed preliminary studies with low-volume 1536-well PCR plates, which indicate that decreasing the total volume

and number of cells by a factor of ten, does not significantly degrade the data quality (results not shown).

Concentration-response curve comparison of 2CS FRET change with known SERCA inhibitors

The spectral unmixing method's capability to resolve 2CS FRET changes via controlled addition of the known SERCA inhibitor thapsigargin, which binds to SERCA2a with subnanmolar affinity (K_i = 2 nM), was evaluated and compared to lifetime mode [124]. Ten different concentrations of thapsigargin were dispensed across a 384-well plate (0.8, 1, 2, 3, 4, 5, 6, 8, 10, and 50 nM thapsigargin concentrations, n = 32 wells for each concentration). Matching DMSO controls (0.5 µL DMSO / 50 µL total well volume) were located in the outer columns (1, 2, 23, and 24) of the 384 well plate. The spectra were decomposed using a four-component model (Eq. 8). The 2CS FRET change, acquired in

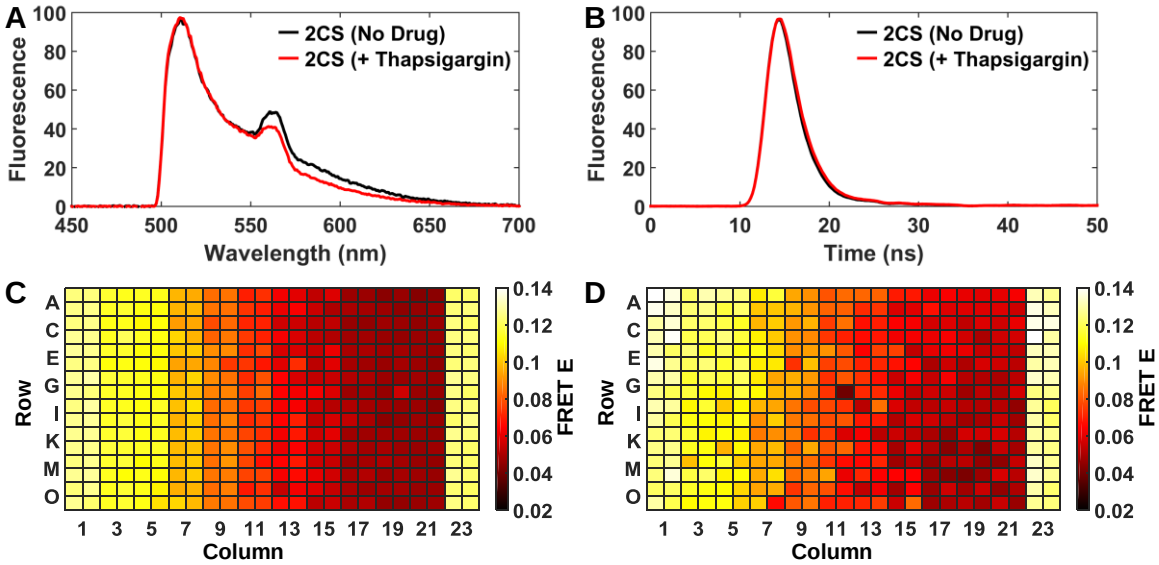

Figure 29. Spectral and lifetime mode comparison of 2CS concentration-dependent FRET change in response to the known SERCA inhibitor thapsigargin. (**A**) Fluorescence emission spectra (average of 32 wells) normalized to GFP intensity, showing 8% reduction in FRET (decreased RFP emission) in response to 50 nM thapsigargin. (**B**) Nanosecond time-resolved fluorescence decay waveforms (average of 32 wells) normalized to GFP-only, showing a 6% reduction in FRET (longer GFP lifetime) in response to 50 nm thapsigargin.(red decay) (**C**) Heat map of FRET efficiency calculated from spectral mode. 10 different concentrations of thapsigargin (0.8,1,2,3,4,5,6,8,10, and 50 nM, increasing left to right) were dispensed across a 384-well plate, with DMSO controls at columns 1, 2, 23, and 24. (**D**) Heat map of FRET efficiency calculated from lifetime mode from the same plate.

spectral mode, is reflected by a decrease in the RFP-region (550-650 nm) of the fitted spectrum (Figure **29A**).

For direct comparison with spectral recording, nanosecond time-resolved fluorescence decay waveforms were acquired on the same samples (Figure **29B**). The fluorescence lifetime for each well was determined as described above (Eq. 6). A saturating concentration of thapsigargin (Tg), (50 nM) induced a 200 picosecond increase in the GFP lifetime, corresponding to a 6% decrease in FRET efficiency, as determined from the lifetime change compared to the donor-only control (Eq. 7), as shown in Figure **29B**. A decrease in FRET may relate to a longer distance between GFP and RFP at SERCA's cytosolic headpiece. Heatmaps of FRET efficiency demonstrate excellent uniformity at each concentration across the plate (Figure **29C, D**), with greater precision evident for the spectral data.

The sensitivity of FRET detection for both lifetime and spectral modes was further investigated by generating 14-point concentration-response curves for addition of thapsigargin, and two other well-established SERCA inhibitors 1,4-dihydroxy-2,5-di-tert-butylbenzene (BHQ) and cylcopiazonic acid (CPA). Reported K_i's fall in the range of 2-7 µM for BHQ and 90-2500 nM for CPA. The concentration-dependent FRET change [124, 125], in response to the three known SERCA effectors, again exhibited excellent agreement between the FRET efficiency acquired from both spectral and lifetime modes (**Figure 30C and D**).

The experimentally determined apparent FRET equilibrium constants of thapsigargin and CPA agree with the previously reported K_i values (Figure **30A and B**).

Note that error bars (n = 8 wells) represent one standard deviation, not standard error of the mean. A tenfold difference from the FRET EC_{50} and reported K_i from functional activity assays was found for BHQ. This finding could reflect a difference between live-cell assays and biochemical functional assays performed on purified proteins. However, we have found the K_i of BHQ to be 400 nM, as assessed by measuring the rate of ATP hydrolysis (data not shown).

The precision of the spectral unmixing and lifetime methods was further assessed by evaluating the FRET efficiency determined from 384 wells of 2CS cells, without the addition of drug. Histograms for all 384 wells of the 2CS cells-only control plate are shown in (Figure **30C and D**). The average FRET efficiency was 13.7% (spectral mode) and 13.6% (lifetime mode) with standard deviations of 0.11% (spectral mode) and 0.36% (lifetime mode).

Spectral fitting results in high assay precision, even if cellular autofluorescence is high

Live-cell fluorescence assays are prone to artifacts from cellular autofluorescence, dispensing error, and other variability in sample preparation [126]. Spectral unmixing is a very effective way to resolve the cellular autofluorescence component, maintaining high precision and accuracy of FRET determination. To simulate increasing autofluorescence (e.g., due to low biosensor expression or transient transfection), cells expressing the 2CS FRET biosensor were mixed with known amounts of untransfected cells, and dispensed across a column-wise gradient of one 384 well plate (**Figure 31A**). The well volume (50 µL) and number of cells per well (50,000) were held constant**.** Spectra were analyzed as in **Figure 1D**, as illustrated in **Figure 31B** for 80% untransfected cells, resulting in much greater autofluorescence than that in **Figure 27D.** The autofluorescence signal from each mixture was assessed by determining weighting coefficient *c* from (Eq. 8), and the expected

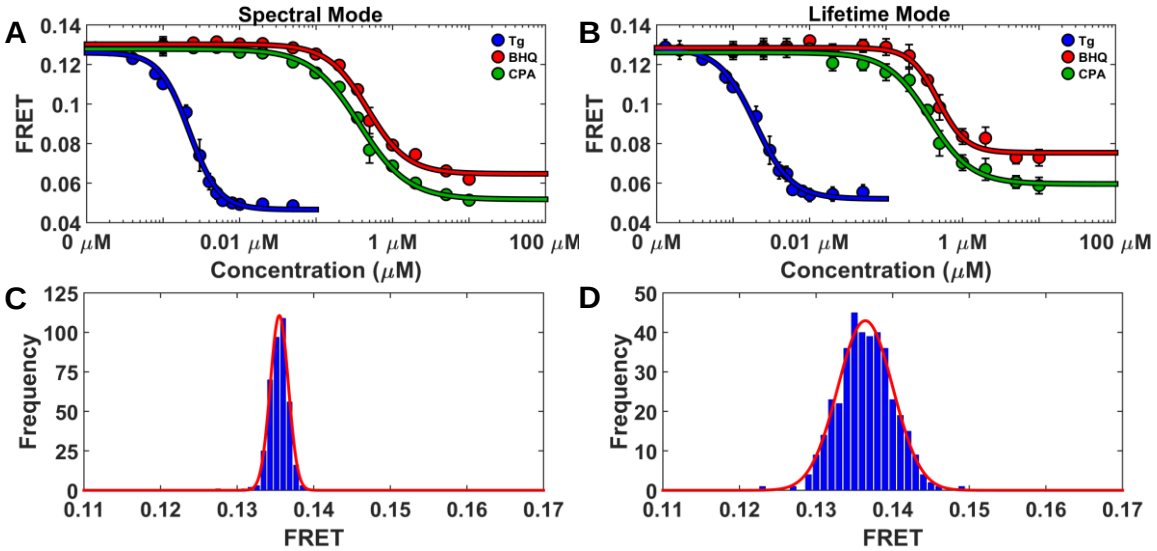

Figure 30. Concentration-response curves and precision of known SERCA effectors. (**A** and **B**) show the concentration-dependent 2CS FRET response of three well-established SERCA inhibitors, thapsigargin (Tg), 4-dihydroxy-2, 5-di-tert-butylbenzene (BHQ), and cylcopiazonic acid (CPA), in a 384-well plate (n = 8 wells for each concentration). Fits to the Hill equation (curves) give EC_{50} values in close agreement for the two modes, and in good agreement with published data on SERCA inhibition. Histograms (**C**) (Spectral Mode) and (**D**) (Lifetime Mode) illustrate the precision of FRET determination from 384 wells of 2CS cells without the addition of drug. Mean and standard deviation values for FRET, determined from the Gaussian fits shown in red, were 13.7% ± 0.11 for spectral and 13.6% ± 0.36 for lifetime.

linear increase was observed (**Figure 31C**). To assess the effect of autofluorescence on the quality of the HTS assay, a 384-well plate was prepared with half the wells containing 100 nM thapsigargin and half being DMSO control wells (%v/v). These positive and negative controls were used to define the signal window for determination of assay quality factor Z′ [61, 127], yielding values of 0.90 (spectral mode) and 0.77 (lifetime mode), indicating that both modes provide an excellent assay for HTS (Z′ > 0.5), until the sample is diluted by 80% (lifetime) or 90% (spectral) with untransfected cells (**Figure 31D**).

Accurate FRET efficiency determination from cyan and yellow fluorescent proteins

Although GFP and RFP (and other red-shifted FRET pairs) are less susceptible to compound fluorescence artifacts [128], the overwhelming majority of genetically-encoded FRET-based biosensors established and studied to date, involve cyan (CFP) and yellow

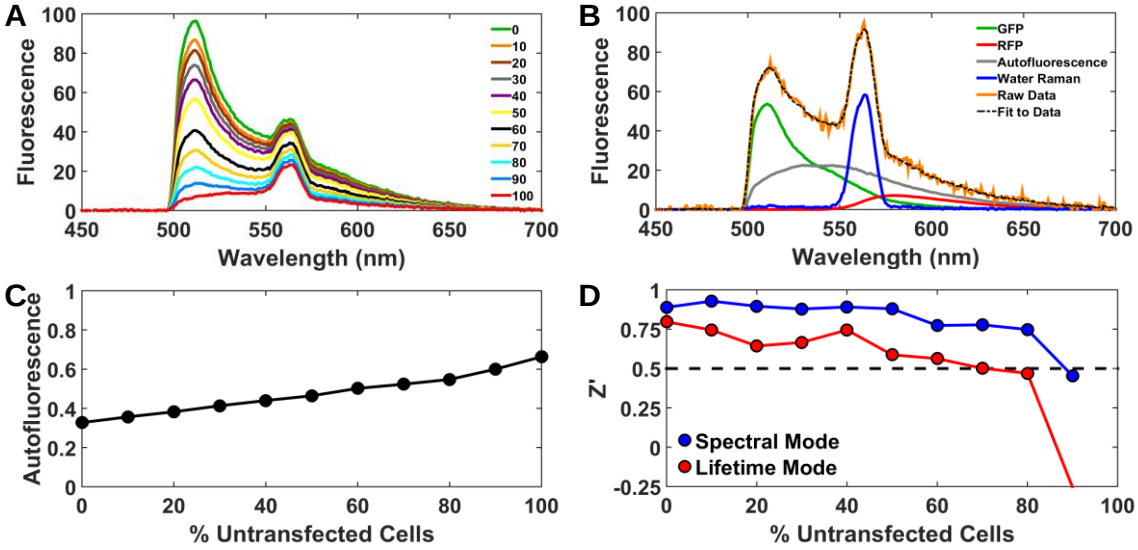

Figure 31 Spectral fitting increases assay precision by solving for the contribution of cellular autofluorescence. (**A**) Spectra were obtained from mixtures of transfected cells (expressing 2CS), with the indicated % of untransfected cells. Each spectrum is the average from 16 wells. (**B**) Example of data analysis using **(Eq. 8**, showing the fit to the data in A for the case of 80% untransfected cells. (**C**) Autofluorescence (*c* in **(Eq. 8**, normalized to the sum of all four components) from fits. (**D**) Quality factor Z′ [61, 127], using the effect of 100 nM Tg (**Figure 30**) to define the signal window.

(YFP) fluorescent proteins [129][129]. Accordingly, we present an illustration of the spectral plate reader's performance using this FRET pair.

Reference standards consisting of mCerulean (CFP) and mVenus (YFP) tethered by flexible linkers of increasing lengths of 5, 17, and 32 amino acids (designated C5V, C17V, and C32V, respectively) [130] have been widely used in FRET calibrations [130](Koushik et al. 2006). Various means to record the FRET signal, including subsequent lifetime and spectral analysis, have been previously applied. These controls can be used to calibrate and validate new FRET detection technology. The consensus FRET efficiencies for these constructs are 43 ± 2 (C5V), 38 ± 3 (C17V), and 31 ± 2 (C32V) %. Transient transfections of HEK293 cells with these FRET reference standards and the appropriate donor CFP (mCerulean) and acceptor YFP (mVenus) labeled constructs were performed. The cells were harvested and assessed on the plate reader with excitation at 434/17 nm from a laser-driven light source (Energetiq). FRET efficiency was evaluated. Optimized transfection protocols for large-scale transient transfections, were found to obtain sufficiently high expression of the FRET standard constructs, so that contributions from autofluorescence and water Raman were negligible. Subsequently, only a two-component fit was required, as shown by the fitted and observed data with component spectra (**Figure 32A**). The CFP/YFP ratio (FR in (Eq. 9),(Eq. 10)) was converted to FRET efficiency as described in Supplemental Material (Derivation), using reported values of extinction coefficients and quantum yields [110]. The acceptor/donor fluorescence ratio, FR in (Eq. 10**)** was then calibrated to the previously reported FRET efficiency of C5V [130].

FRET efficiencies determined from spectral mode were in excellent agreement with the reported results 42.3 ± 0.7 (C5V), 38.3 ± 0.7 (C17V), and 29.0 ± 0.6 % (C32V) as shown in **Figure 32B**. The precision was high; each bar represents the data from a single well. These results validate the capability of accurate FRET efficiency determination from CFP and YFP FRET pairs using the spectral unmixing method.

Investigation of a CFP and YFP FRET pair was evaluated with the well-known cameleon calcium sensor, in which the calmodulin-binding (M13) domain of myosin light chain kinase (MLCK) and calcium-binding domain of calmodulin are fused together, and located between two fluorescence proteins (eCFP/mCitrine). These calcium sensors have allowed cellular [Ca^{2+}] to be monitored more directly and reliably than using calcium-sensitive dyes [131]. The endoplasmic reticulum-targeted cameleon sensor (D1ER) was

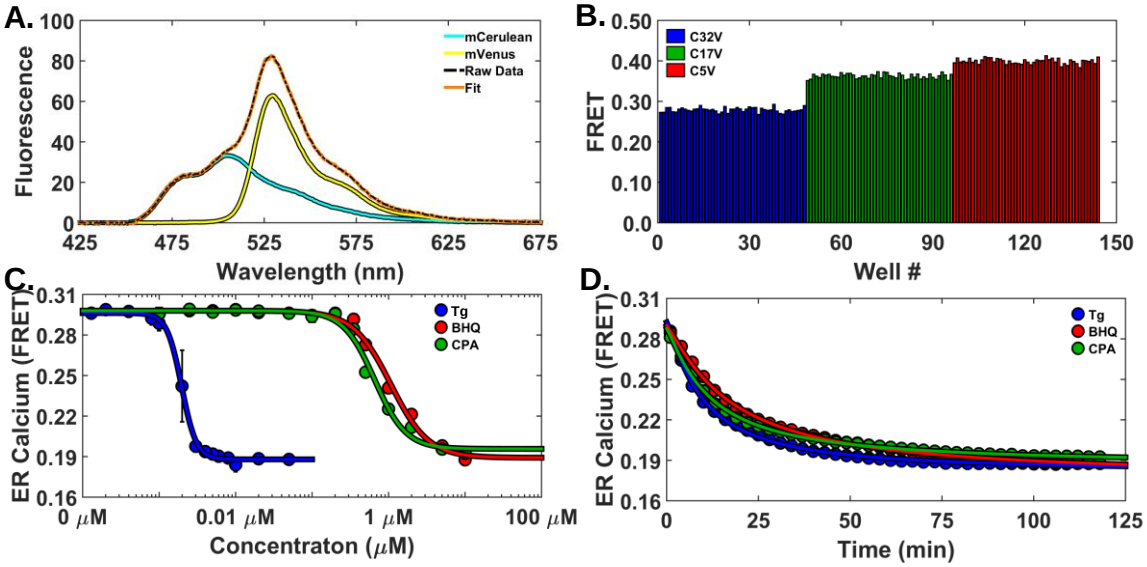

Figure 32. Accurate FRET efficiency determination from CFP and YFP biosensors in HEK293 cells. (**A**). Two-component spectral fit of the C17V FRET standard. (**B**) FRET data from three CFP-YFP FRET pairs with different lengths. 48 wells for each of the three pairs were studied in a 384-well plate. (**C**) Concentration-response curves showing the effects of three SERCA inhibitors on FRET (120 min after mixing), using the CFP/YFP-based D1ER cameleon FRET calcium sensor (n = 8 wells for each concentration). Curves show best fits to the Hill equation.(**D**) Time-dependent effects of SERCA inhibitors on ER Calcium at saturating drug concentrations. DMSO controls have no effect on ER calcium concentrations (data not shown). Thapsigargin (Tg, blue) irreversibly binds SERCA with high-affinity and depletes calcium at a faster rate than BHQ and CPA, which have micromolar binding affinities.

selected because it is known to be sensitive to the SERCA inhibitors thapsigargin, CPA, and BHQ. Instead of detecting direct ligand binding, as in the 2CS studies reported above, the D1ER sensor can be used to monitor changes in ER calcium level [132]. Upon SERCA inhibition, calcium is no longer pumped into the ER, leading to calcium depletion through various mechanisms including IP3-gated receptors and ryanodine receptors. D1ER senses these changes as calcium binding leads to a conformational rearrangement of the biosensors, increasing FRET between CFP and YFP. Therefore, calcium depletion due to SERCA inhibition is detected as a decrease in FRET.

A HEK293 stable clone with constitutive expression of the D1ER cameleon calcium sensor was generated using G418 antibiotic selection. The localization of D1ER to the endoplasmic reticulum (ER) lumen was verified by microscopy, and expression remained constant over months in culture. Cells were harvested and dispensed into 384-well plates containing the same concentrations of thapsigargin, CPA, and BHQ, as previously evaluated with 2CS (**Figure 30**). D1ER FRET was monitored only in spectral mode, because the CFP donor cannot be excited effectively by the 473 nm laser used in lifetime mode. ER calcium was monitored by repeatedly scanning the 384 well plate at three-minute intervals over a 120-minute period. The expected concentration and time-dependent decreases in FRET were observed. The high-affinity and selective SERCA inhibitor thapsigargin produced a sigmoidal FRET response with an equilibrium constant of 1.97 nM (ER calcium depletion shown at 120 min time point) (**Figure 32C**).

The submicromolar SERCA inhibitors BHQ and CPA also produced a concentration-dependent effect. FRET EC_{50} values were evaluated for each concentration

curve, and agree with the expected values based on their affinity for SERCA. The time-dependent effect of SERCA inhibitors on endoplasmic reticulum (ER) calcium concentration can be determined by evaluating the rate of calcium depletion (FRET decrease) in response to titration with the inhibitors. Thapsigargin (Tg) irreversibly binds SERCA with high-affinity, and depletes calcium at a faster rate than BHQ and CPA, which have micromolar binding affinities (Figure **32D**). The time dependence of calcium depletion was evaluated by fitting each curve to the Hill equation to determine the rate of calcium depletion T_{50}. The T_{50} of thapsigargin, BHQ, and CPA were 9.5, 17.4, and 11.7 minutes; respectively.

4.5 Discussion

Accurately recording a fluorescence signal is an essential element of fluorescence spectrometers, microplate readers, fluorescence microscopes, flow cytometers, qPCR machines, chromatography, capillary array electrophoresis detectors, gel scanners, and sequencers. However, scanning a wavelength-selective filter (monochromator) through a range of emission wavelengths is usually employed only for research-grade fluorescence spectrometers, where data quality is more important than measurement speed. Microplate readers equipped with monochromators, now commonly available, could serve as alternatives to research-grade spectrometers. The primary difference between the two classes of instruments lies in the sample holder format and optical geometry, i.e., cuvettes and right angle for spectrometers, plastic plates and epi-illumination for plate readers. It is plausible to assume that a research-grade, cuvette-based fluorescence spectrometer will always provide much higher data quality than could ever be possible in a microplate reader,

because the right-angle geometry, large sample volumes, and high-quality optics of the sample container minimize artifacts from light scattering and other sources of interfering background [107]. However until now, a comprehensive study that directly compares the data quality obtained with a fluorescence microplate reader to that produced by a fluorescence spectrometer did not exist (**Figure S33**). The de facto standard approach to performance characterization of fluorescence spectrometers is the water Raman test [133]. The corresponding de facto standard approach to performance characterization of microplate readers is a fluorescence limit-of-detection test [134]. The data presented here strongly suggest that the quality gap between fluorescence spectrometers and microplate readers is much smaller than is generally assumed.

Genetically encoded FRET sensors are usually studied via imaging in a fluorescence microscope, using a rigorous 3-cube technique [112]. Corrections for cross-talk or bleed-through between the donor and acceptor excitation/emission [134] are determined by assessing images of fluorescence proteins expressed individually at each wavelength of interest. Acquisition at multiple excitation and emission wavelengths is typically required during each microscopy experiment. A major advantage revealed by these studies is that the shape of the full emission spectrum (2048 data points spread across the 300-800 nm wavelength region) can be used to reliably and accurately quantitate fluorescence signal without the need for exhaustive controls on each of day of experiments. Reference spectrum from control cell lines (in suspension) need only to be acquired one time. They were used to calibrate for detector sensitivity, and found to produce reproducible results for months on end. This drastically reduced the workload of

maintaining and culturing control cell lines, thereby increasing productivity by reducing the number of conditions required for each experiment.

Another source of potential error in imaging experiments is autofluorescence contributions or interfering background emission. Microscopy methods rely on defining regions of interest, designed to isolate the cells of interest (e.g., cells that have the highest fluorescence signal) from the background. These results are averaged over a statistically meaningful number of cells [135]. The laborious nature of fluorescence emission correction from cellular autofluorescence and fluorescent protein crosstalk has made its usefulness for high-throughput drug screening impractical.

The spectral unmixing method incorporates essentially the same filter cubes and epi-illumination geometry as fluorescence microscopy. However, no attempt is made to image individual cells, as a simple lens directs the excitation light into a microplate well, and collects the emitted fluorescence signal. This cells-in-wells approach treats the cells as a homogeneous solution. Excitation of less than 50,000 cells placed in suspension, yielded enough photons to obtain high-quality spectra and fluorescence decay rates (lifetime) in a fraction of a second.

Spectral unmixing in fluorescence microscopy has previously been limited to low-throughput high-end instruments, typically based on a multi-anode PMT with 32 channels on roughly 10-nm spacing [136]. The present approach utilizes a linear array detector, and records at intervals of approximately 0.5 nm. This is substantially narrower than the width of the spectral features of interest, but advantageous nonetheless because oversampling improves the robustness of the fitting.

Many methods have been developed to decompose the fluorescence spectrum for the purposes of correcting waveform distortions associated with monochromator-based excitation and emission [135, 137]. The complexities of these methods are unsuitable for large-scale drug discovery campaigns. The development of a simplified method for multi-component spectral analysis for the determination of FRET efficiency from a live-cell biosensor, resulted in a assay suitable for high-throughput screening, as shown by the Z' in **Figure 31D**. Reference spectra of the known components are used to decompose the spectrum from the sample of interest (**Figure 1C**). The spectral recording technology allows for robust measurements, with inexpensive equipment in comparison to fluorescence microscopes and flow cytometry. The spectral unmixing method can also be used to solve for unknown components such as sample contamination or, as shown in our following companion paper [138], the direct identification of fluorescent compounds (false-positives) during a high-throughput drug screen.

Data acquired by both spectral and lifetime modes were shown to be extremely precise. The focus of this article is to demonstrate the novel spectral recording technology, as the lifetime technology has previously been evaluated [114, 116, 117]. However, this is the first demonstration of the top-read fluorescence lifetime plate reader. This optical configuration is advantageous, as inexpensive black-bottom microplates can be used, instead of glass-bottom microplates. Another benefit is that temperature can be controlled by placing a heat source underneath the microplate. These studies directly compared two novel fluorescence plate reader technologies. A three-fold increase in precision was found for spectral mode over lifetime mode as shown in Figure **30C, D.** These studies utilized

data analysis methods that can currently be used for large-scale drug discovery efforts, as they are not computationally taxing, and can be performed in real time. The precision of the lifetime method is likely to be increased by development of more sophisticated analysis methods. For example, in these studies a single-exponential model was used to fit the lifetime data, and no attempt was made to correct the lifetime data for artifacts from cellular autofluorescence. Demonstrations of advancements in using more-rigorous global lifetime analysis can be found in the accompanying article, reporting high-throughput screening performance [138].

The increased precision from spectral mode, as compared with lifetime mode, is likely to be observed primarily when employing two-color biosensors, in which every donor has an acceptor on the same molecule. In biosensors created by reacting dyes with amino acid side chains, and/or involving donor and acceptor on different proteins, lifetime detection has the advantage of resolving heterogeneous populations of donors. The unique structural resolution of the lifetime mode also permits the resolution of multiple structural states of the biosensor [112, 139, 140], providing more detailed structural information about the results of screening.

Two distinct classes of live-cell FRET biosensors were shown, those that are designed specifically for structure determination (**Figure 29A; Figure 30A; Figure 32B**), and those that exploit a structural change in the biosensor for the purpose of quantitating the concentration of some species, such as $[Ca^{2+}]$, in the cellular milieu **(Figure 32C,D)**. There are many applications in which a better way to detect structural changes of either a cytosolic or membrane protein via FRET would be valuable. Developing and engineering

fluorescent protein FRET biosensors can be challenging, as they can be difficult to express (low signal, high cellular autofluorescence), they exhibit a low FRET signal (because the donor and acceptor are too far apart), or the dynamic range of the signal window may be limited. These problems can be overcome, as incredibly small changes in FRET signal can be detected using this spectral and lifetime detection technology. Even more so, detection of weak GFP fluorescence masked by cellular autofluorescence, was clearly resolved using the spectral unmixing methods.

Beyond increased sensitivity and precision, the rapid acquisition rates reported here (10 wells or more per sec) allow for time-course studies. Previous reports suggest that the resolution and sensitivity of microplate readers is inadequate to directly monitor calcium flux in live-cells [141]. To date, high-throughput screening with cameleon sensors, such as D1ER, has been achieved using laborious high-content imaging [142], or calcium-sensitive fluorescent dyes with CCD-camera based plate readers (FLIPR, Molecular Devices). To our knowledge, this is the first time changes in live-cell calcium levels were shown to be monitored with high speed and precision in a fluorescence microplate reader using a FRET based biosensor (**Figure 32C**). Short acquisition times of 200 ms per well were used to repeatedly scan portions of high-density microplates, and monitor calcium flux at rates, comparable to standard microscopy techniques; except across a range of chemical perturbations (**Figure 32D**). Thus, the D1ER FRET-based calcium biosensor may be a powerful tool for high-throughput screening, linking the structural perturbations of 2CS to functional changes, at the level of calcium dysregulation in live-cells.

The spectral and lifetime detection methods presented here are widely applicable across the life sciences, beyond high-throughput and high-content assays. Potential assays, which may benefit from this platform are phenotypic screening of libraries of mutant constructs, recombinant antibody development, or protein stability assays, where sample quantities are limited. Future technological developments may also include cell sorting by the addition of microfluidics devices.

In conclusion, a new instrument records fluorescence spectra in a microplate reader, at speeds fully compatible with high-throughput screening applications. The resolution of the recorded spectra is improved in comparison to that provided by standard cuvette-based fluorescence spectrometers, even though the acquisition rates are 100 times faster and sample volumes 100 times smaller (**Figure S33**). The novel spectral and lifetime technologies were thoroughly evaluated, and when used together are complementary, creating a new combination of precision and resolution, particularly in applications to living cells expressing genetically encoded FRET biosensors. Accuracy and precision is comparable to or greater than those achieved with much lower throughput instruments, such as cuvette-based spectrofluorometers and fluorescence microscopes. These technical breakthroughs in fluorescence recording enable their use in high-throughput screening applications, as illustrated in the following article [138].

Declaration of Conflicting Interests

Dr. Thomas holds equity in and serves as an executive officer for Photonic Pharma LLC. This relationship has been reviewed and managed by the University of Minnesota.

Acknowledgments

We thank Jesse E. McCaffrey, Karl Petersen, Razvan L. Cornea, Benjamin Binder, and J. Michael Autry for helpful discussions, Octavian Cornea for assistance in manuscript preparation, and Simon J. Gruber and Seth L. Robia for development of the reagents and materials used for many of the experiments. Fluorescence microscopy was performed at the UMN Imaging Center, flow cytometry at the UMN Lillehei Heart Institute, and spectroscopy was performed at the UMN Biophysical Technology Center. pcDNA-D1ER was a gift from Amy Palmer & Roger Tsien (Addgene plasmid # 36325). C5, C17V, and C32V was a gift from Steven Vogel (Addgene plasmid # 26394, 26395, and 26396)

Funding

The authors disclosed receipt of the following financial support for the research, authorship, and/or publication of this article: This work was supported by NIH grants R42DA037622 (to G.D.G and D.D.T.), R01HL129814 (to D.D.T.), and R01GM27906 (to D.D.T.). T.M.S. was supported by the NIH Chemistry-Biology Interface Training Grant (5T32GM008700), and by predoctoral fellowships from 3M and Arnold H. Johnson.

4.6 Supplementary Material

Reference spectra determination for fluorescence emission components of 2CS FRET biosensor

The spectral unmixing process yields a decomposition of the observed (experimental) spectrum into a linear combination of biochemically meaningful component spectra. In the case of the experiments reported here, a minimum of four components (basis spectra) must

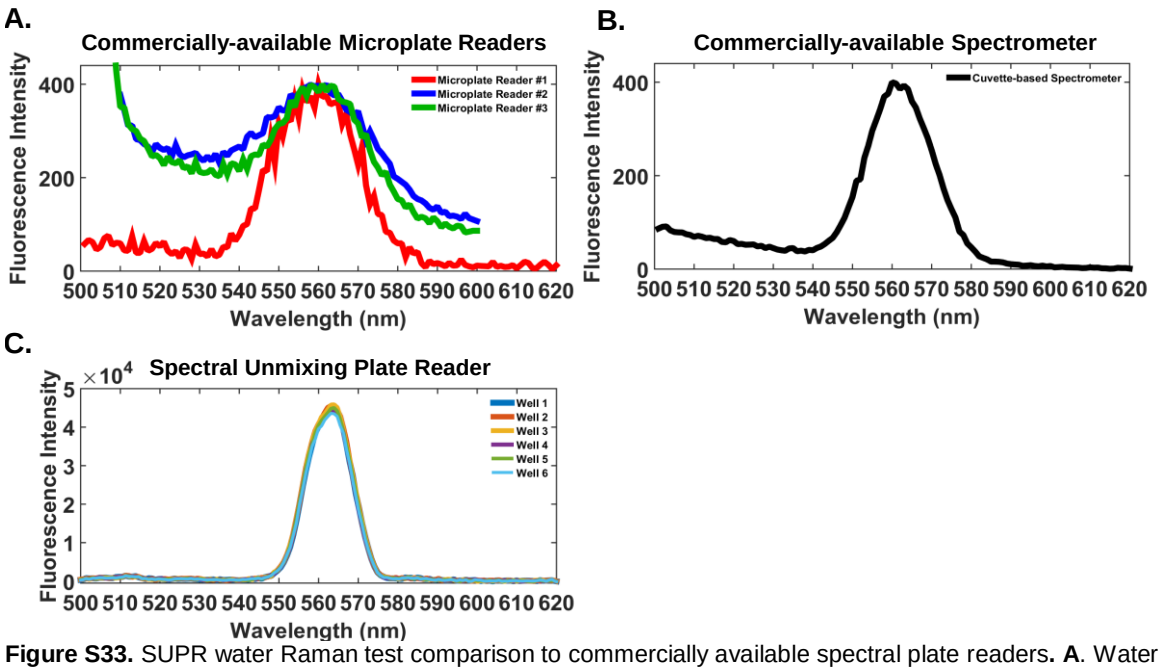

Figure S33. SUPR water Raman test comparison to commercially available spectral plate readers**. A**. Water Raman spectra acquired on a commercially-available fluorescence microplate readers. Total acquisition time is approximately 2 minutes for each spectrum (one second per wavelength). **B**. Water Raman spectrum acquired using a cuvette-based spectrometer with flash lamp excitation. **C.** Water Raman spectra acquired from six separate wells of one 384 well plate using the spectral unmixing plate reader. The six raw spectra are ovelaid to demonstrate the reproducibility across measurements.

be included in the spectral fitting: donor fluorescence (GFP), acceptor fluorescence (RFP), cellular autofluorescence, and Raman scattering of the buffer (effectively the inelastic Raman scattering of water). Scattered exciting light, stray light, background fluorescence of the plate material, and impurities are other possibilities. The quality of the fit is typically judged by the residuals (errors) between the observed and fitted spectrum. A challenge that was overcome was that it is not possible to prepare pure samples of the individual components except in the case of the water Raman.

Water Raman:

A signal-to-noise comparison of the inelastic light scattering due to the water Raman band after excitation at 473 nm (GFP excitation) was performed. Comparison water Raman spectra were acquired on three commercially-available fluorescence microplate readers equipped with emission monochromators. The acquisition rate in these experiments

(Figure S33A) was set at one second per wavelength, and the wavelength spacing at 1 nm. A water Raman spectrum (black) was also acquired on a cuvette-based fluorescence spectrometer (Cary Eclipse, xenon flash-lamp excitation) with the same acquisition time and wavelength interval **(Figure S33B)**. **Figure S33C** shows the superposition of six spectra, each corresponding to a different well of a 384 plate, at 200 ms acquisition time per well, acquired with the spectral unmixing plate reader (Fluorescence Innovations). The spectra have been normalized to the same area under the curve to better illustrate the very high repeatability. The relatively narrow water Raman spectra acquired with the spectral unmixing plate reader, allows for the capability to extract spectral features, and produce robust and high precision measurements. Note, too, the very low background signal from the black polypropylene plates on either side of the water Raman band, despite the epi-illumination geometry.

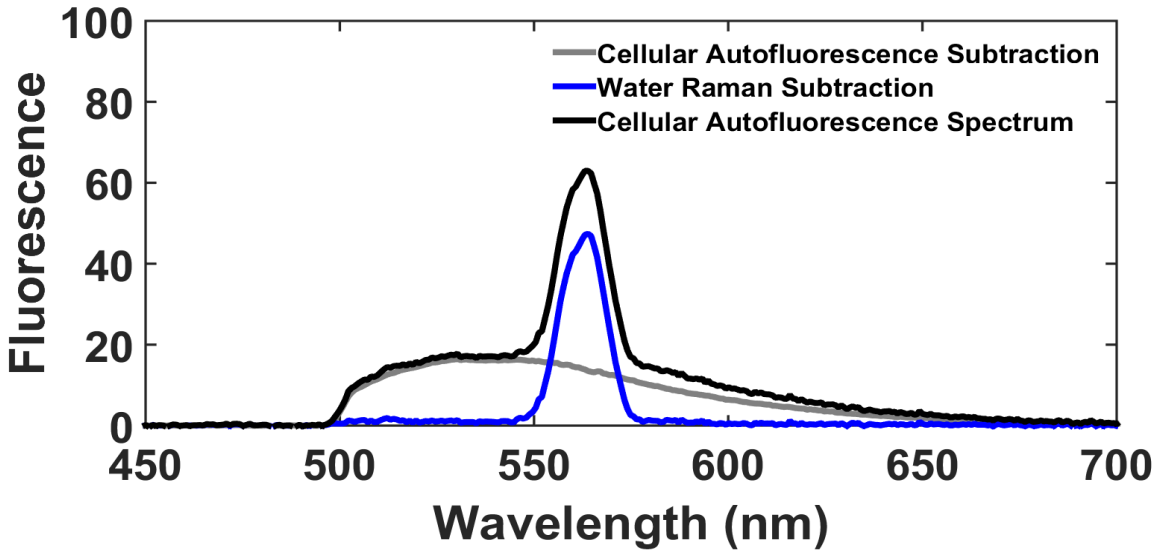

Figure S34. Determination of autofluorescence reference spectrum.

Cellular autofluorescence: Excitation of living cells in the 450-500 nm wavelength range produces a background autofluorescence signal, generally attributed to flavins [143]. The fluorescence spectrum of 50 μL of untransfected HEK293 cells suspended in PBS at a concentration of 50,000 cells per well of a 384 well plate is shown in

Figure S34. The sharp and narrow peak of the water Raman feature at 560 nm was used to subtract the water Raman signal from cellular autofluorescence spectrum, thereby

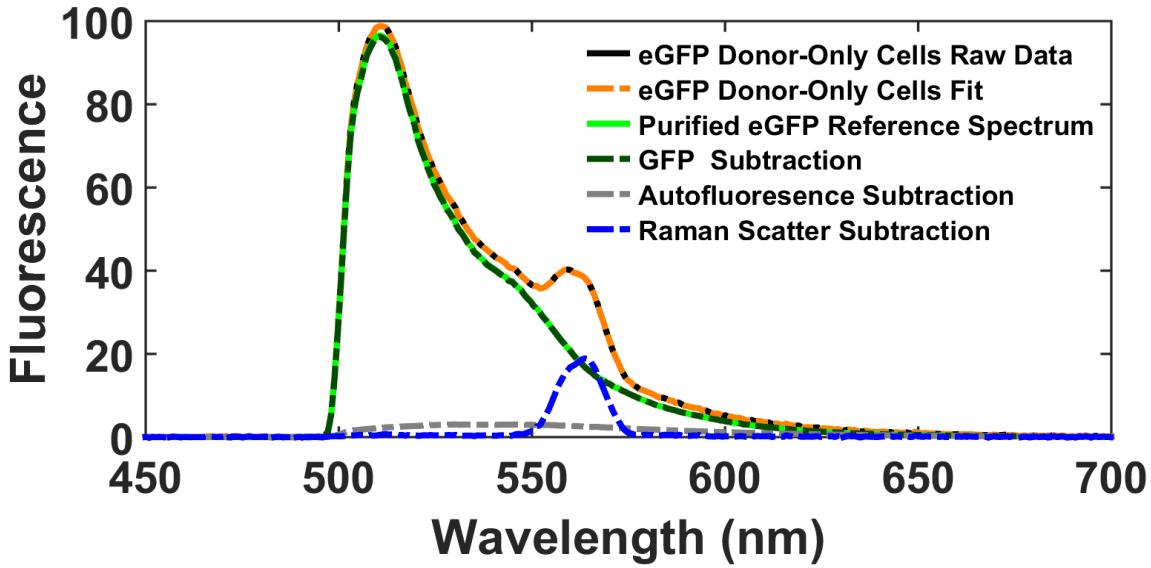

Figure S35. Determination of GFP reference spectra.

producing the autofluorescence reference spectrum.

GFP reference spectrum. The reference spectra of GFP (eGFP) were acquired from purified fluorescent protein preparations, and by subtracting each component spectrum (water Raman, autofluorescence, and the signal from fluorescent protein) using live-cells expressing the fluorescent proteins. The former approach avoids the need to consider the

autofluorescence contribution, but the signal of the green or red fluorescent proteins may be dependent on buffer conditions, and vary with environment surrounding the purified protein.

The reference spectrum of GFP, the donor fluorescent protein used for the red/green FRET pair of the two-color SERCA biosensor, was acquired from HEK293 cells overexpressing high levels of an appropriately donor-labeled control cell line. This cell line expressed a genetically-encoded construct, where GFP was fused to an intra-sequence flexible loop on SERCA2a's cytosolic nucleotide-binding domain (at residue 509). The GFP reference spectrum was generated by subtracting the contribution of the cellular autofluorescence and water Raman from the observed GFP SERCA control cell line (dark green spectrum in **Figure S35**). The fluorescence signal of the GFP-SERCA fusion protein was much higher than the background signal from the cells themselves (cellular autofluorescence). Therefore, a very subtle subtraction of the autofluorescence signal was made for this particular cell line. However, the shift in the shape of the subtracted GFP reference fluorescence spectrum did not significantly alter the results of the spectral unmixing methods. This reference spectrum was used to accurately resolve the fluorescence signal of GFP from a cell line over-expressing the two-color SERCA FRET biosensor. Further comparison of the inferred GFP reference spectrum from live-cells with the spectrum of purified protein is shown in **Figure S35**, by the overlay of GFP subtraction and the denoted solved GFP reference spectrum. Although small variations in the overall shape of the reference GFP spectrum acquired from live-cells and purified protein

preparations have been previously reported [143], these differences did not distort the results obtained from the spectral unmixing methods.

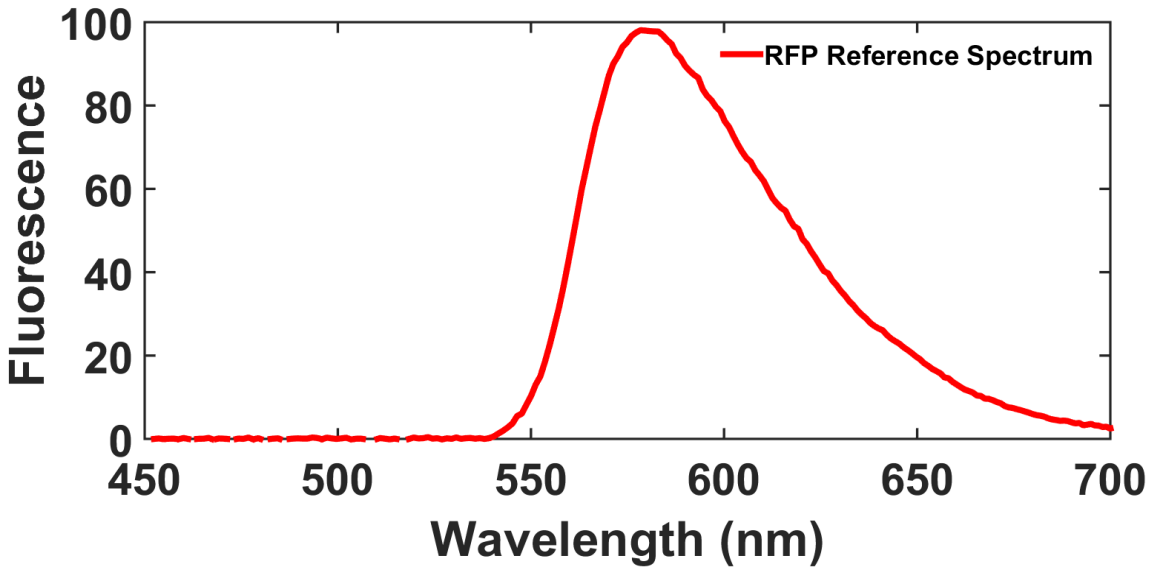

Figure S36. HEK293 cells overexpressing an acceptor-only control construct. TagRFP was fused to SERCA2a used to generate the tagRFP reference spectrum (red). A longer wavelength excitation (532 nm) was used, so the subtraction of cellular autofluorescence and the water Raman signal are not required.

RFP reference spectrum. The reference spectrum of the red fluorescent protein (tagRFP) was acquired using 532 nm laser excitation, which eliminated the contribution from cellular autofluorescence. Excitation at a longer wavelength also shifts the water Raman band to the 650 nm wavelength. The effect of the water Raman band is much weaker because of its λ^4 dependence. Finally, the RFP-SERCA fluorescent fusion construct had much higher expression than the intrasequence labeled GFP-SERCA control construct. The RFP reference spectrum is shown in **Figure S36**.

The four reference spectra shown in **Figure 27A** were used for all studies involving spectral unmixing of the 2CS construct with GFP and RFP-labeled fluorescent proteins.

Derivation of the spectral FRET equation for 2-color biosensor

Nomenclature:

ε_A: molar absorptivity of acceptor at λ_{ex}

ε_D: molar absorptivity of donor at λ_{ex}

Φ_{FRET}: Fluorescence quantum yield of FRET efficiency

$\Phi_{F,D}$: Fluorescence quantum yield of donor, including potential change due to FRET

$\Phi_{F,A}$: Fluorescence quantum yield of acceptor

Assumptions:

1. # Donor excited states proportional to ε_D
2. # Acceptor excited states proportional to $\varepsilon_D \Phi_{FRET} + \varepsilon_A$
3. # Donor emission events proportional to $\varepsilon_D \Phi_{F,D}$
4. # Acceptor emission events proportional to $(\varepsilon_D \Phi_{FRET} + \varepsilon_A) \Phi_{F,A}$

Derivation:

Let *FR* be the FRET ratio of total number of photons emitted by acceptor to total number of photons emitted by donor (Eq. 5); assuming the CCD linear-array spectrograph detector has been corrected for wavelength dependence of its response. The total fluorescence emission *F* of each component's reference spectrum is dependent on the scalar coefficients shown as the sum of the linear combination of the four components of the fluorescence emission signal from as shown in (Eq. 8), where *b* represents the scalar coefficient for RFP (acceptor), and *a* the scalar coefficient for GFP (donor).

$$FR = \frac{Acceptor\ fluorescence}{Donor\ fluroescence} = \frac{bF_{RFP}}{aF_{GFP}}. \qquad \text{Eq. 10}$$

Substitution of extinction coefficients (molar absorptivity) and quantum yields, which represent the total acceptor and donor fluorescence from the FRET biosensor gives following equation:

$$FR = \frac{(\varepsilon D\ \Phi FRET\ +\ \varepsilon A)\ \Phi F, A}{\varepsilon D\ \Phi F, D}. \qquad \text{Supp Eq. 1}$$

However, the contribution of FRET to the donor fluorescence when the rate of fluorescence energy transfer is zero, gives $\Phi_{F,D} = \Phi_{F,D}(E = 0)\ (1 - \Phi_{FRET})$. Substitution of this equation for the donor quantum yield at (E=0) yields:

$$FRET = \frac{FR * \Phi F,D/\Phi F,A - \varepsilon A/\varepsilon D}{1 + FR * \Phi F,D/\Phi F,A}. \qquad \text{Supp Eq. 2}$$

where QR $(\Phi F,D/\Phi F,A)$ is the ratio of the donor fluorescence quantum yield under non-FRET conditions to the acceptor fluorescence quantum yield. AR ($\varepsilon A/\varepsilon D$) is the extinction coefficient ratio of acceptor molar absorptivity to the donor molar absorptivity at 473 nm wavelength excitation. Note that FR is the only experimentally derived quantity as the quantum yields and extinction coefficients of the eGFP and tagRFP have been previously reported, and were determined for 473 nm wavelength excitation [110].

The quantum yield ratio could be determined directly, although quantum yields are notoriously difficult to measure with very high accuracy. Moreover, the fluorescence ratio (FR) depends on the wavelength dependence of the CCD spectrograph detector. In other words, the measured FR needs to be corrected to a constant detector response (no wavelength dependence).

A β-factor was experimentally determined, and used to calibrate for the difference in the overall spectrograph sensitivity at longer wavelengths (wavelength-dependent

response and the wavelength dependence of the grating's diffraction efficiency) The dispersion of the light by the grating is non-linear, so shorter wavelength light is spread out more than longer wavelength light. For simplicity the β-factor was designated to quantum yield factor (QR) yielding:

$$FRET = \frac{\beta\ (\mathrm{QR})\ *\ \mathrm{FR} - (\varepsilon \mathrm{A}/\varepsilon \mathrm{D})}{1\ +\ \beta(QR)\ *\ \mathrm{FR}}. \qquad \text{Supp Eq. 3}$$

The β value (correction factor) used to correct for difference in GFP and RFP detector sensitivity was determined using the fluorescence lifetime data of the τ_D (GFP-SERCA) and τ_{DA} (2CS) cell lines, and solving for the apparent FRET efficiency in as (Eq. 7) shown in **Figure S37**.

Solving for the FRET efficiency of 2CS (above) for β gives

$$\beta\ =\ [(\tau \mathrm{D}/\tau \mathrm{DA})(1 + \varepsilon \mathrm{A}/\varepsilon \mathrm{D}) - 1]/\mathrm{FR} \qquad \text{Supp Eq. 4}$$

where the τ values are fluorescence lifetimes acquired from the appropriate donor-only and donor-acceptor (FRET) cell lines.

Supp Eq. 4 shows a single β-value (corrected QR = 0.83) that gives excellent agreement between the FRET efficiency values calculated by lifetime and by spectra. The data used for this calibration of FRET efficiency was from the 12-point thapsigargin 2CS dose-response studies (**Figure 30A and B**). Each point on the plot shows the FRET

efficiency obtained from lifetime mode (direct determination using (Eq. 7), and after solving for the β-factor using the spectral FRET efficiency equation (Eqs. 5 and 6) at 12 different concentration of Thapsigargin. For all FRET pairs, each correction factor was obtained by using reported values of the fluorescent protein quantum yield and molar absorptivity [110], and correcting for CCD detector sensitivity. The β-factors for the CFP/YFP variants were not determined by direct comparison to fluorescence lifetime measurement, because a microchip pulsed laser with the appropriate excitation wavelength does not exist. The β-factor for the quantum yield ratio of the mCerulean and mVenus FRET pair was determined by using the known FRET efficiency of the C32V construct [130], and solving for the β-factor to match the expected value. This β-factor was then used to determine the FRET efficiency of the C17V and C5V construct as shown in **Figure 32B**. The beta-factor for the eCFP/mcitrine FRET pair was determined by estimating the FRET efficiency of the D1ER FRET biosensor, under normal cellular conditions, using previously reported fluorescence lifetime measurements [144]. QR in supplemental table is the β-factor corrected quantum yield ratio from each FRET pair.

Table 2. Quantum yield and molar absorptivity ratios for donor and acceptor FRET pairs

FRET pair	QR	AR
eGFP and tagRFP (2CS)	0.83	0.05
eCFP and mCitrine (D1ER)	0.46	0.12
mCerulean and mVenus	0.37	0.10

Multiple-exponential lifetime fitting

The donor-only control cell line, where SERCA2a is fused to GFP, was used to determine the FRET efficiency using (Eq. 7 in first manuscript, $E = 1- \tau_{DA}/\tau_{D}$). The fluorescence

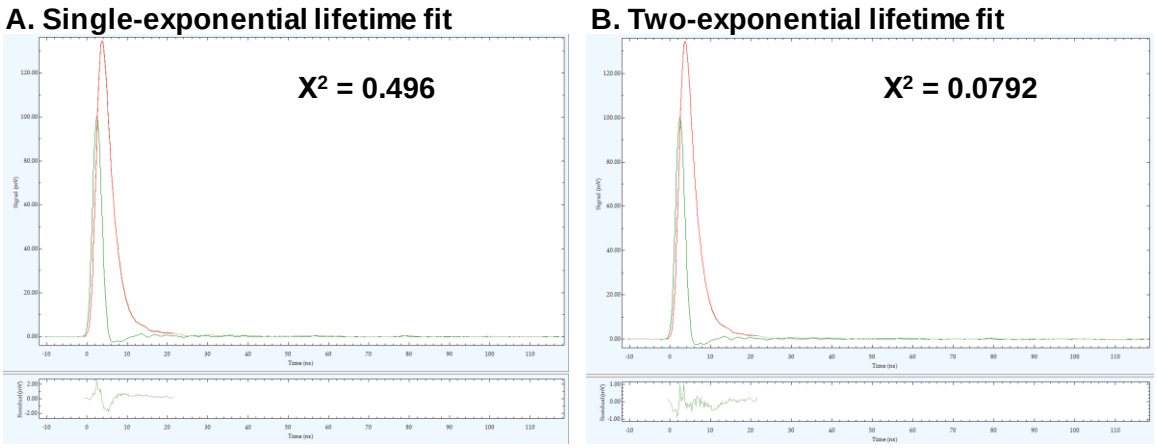

Figure S37. The fluorescence lifetime of the donor-only (GFP) one-color SERCA control. Evaluated using a single-exponential fit **(A)** and a two-exponential fit **(B).** For each fit (red), the raw donor-only waveform is shown in black and the instrument response function in green. The residuals from each fit across the nanosecond time domain (x-axis) is shown below the fluorescence decay waveforms and used to determine the χ^2. As shown the χ^2 was reduced for the two-exponential fit and the average lifetime was found to be 2.58 ns.

waveform was fit using both one- and two-exponential model as shown in **Figure S37**. The χ^2 of each fit across the nanosecond domain was determined from the sum of the residuals obtained from the fit. The χ^2 was reduced for the two-exponential model and this model was used for subsequent global lifetime analysis to determine distance distributions. Adding more than two exponentials to the model was not found to increase the goodness of the fits.

Chapter 5 – High-throughput Spectral and Lifetime-based FRET Screening

High-throughput spectral and lifetime-based FRET screening in living cells to identify small-molecule effectors of SERCA

Tory M. Schaaf[1], Kurt C. Peterson[2], Benjamin D. Grant[2], Prachi Bawaskar[1], Samantha Yuen[1], Ji Li[1], Joseph M. Muretta[1], Gregory D. Gillispie[2] and David D. Thomas[1,3,*]

[1]Department of Biochemistry, Molecular Biology and Biophysics, University of Minnesota, Minneapolis, Minnesota 55455
[2]Fluorescence Innovations Inc., Minneapolis, MN 55455
[3]Photonic Pharma LLC, Minneapolis, MN 55410

Reprinted from:

Schaaf TM, Peterson KC, Grant BD, Bawaskar P, Yuen S, Li J, Muretta JM, Gillispie GD, Thomas DD. Spectral Unmixing Plate Reader: High-Throughput, High-Precision FRET Assays in Living Cells. J Biomol Screen. 2016 Nov 29. pii: 1087057116680151. [Epub ahead of print]

Author Contribution Statement:
TMS designed experiments, performed experiments, analyzed data, and wrote the manuscript. SLY performed ATP activity assays. SLY and JL prepared and formatted the NCC library into 384 well plates. PB provided cell culture support for screening. KCP and BDG built the fluorescence plate readers, and wrote software for plate reader data acquisition and analysis. JMM directed global lifetime fitting analysis. GDG and DDT contributed to experimental design, and edited the manuscript. DDT advised and managed the project.

5.1 Summary

A robust high-throughput screening (HTS) strategy has been developed to discover small-molecule effectors targeting the sarco/endoplasmic reticulum calcium ATPase (SERCA), based on a fluorescence microplate reader that records both the nanosecond decay waveform (lifetime mode) and the complete emission spectrum (spectral mode), with high precision and speed. This spectral unmixing plate reader (SUPR) was

used to screen libraries of small molecules with a fluorescence resonance energy transfer (FRET) biosensor expressed in living cells. Ligand binding was detected by FRET associated with structural rearrangements of green (GFP, donor) and red (RFP, acceptor) fluorescent proteins fused to the cardiac-specific SERCA2a isoform. The results demonstrate accurate quantitation of FRET along with high precision of hit identification. Fluorescence lifetime analysis resolved SERCA's distinct structural states, providing a method to classify small-molecule chemotypes on the basis of their structural effect on the target. The spectral analysis was also applied to flag interference by fluorescent compounds. FRET hits were further evaluated for functional effects on SERCA's ATPase activity via both a coupled-enzyme assay and a FRET-based calcium sensor. Concentration-response curves indicated excellent correlation between FRET and function. These complementary spectral and lifetime FRET detection methods offer an attractive combination of precision, speed, and resolution for HTS.

5.2 Introduction

The preceding article reports the performance of a novel microplate-reader that records fluorescence emission spectra with an unprecedented combination of speed and precision. That study indicated that this spectral-unmixing plate-reader (SUPR), when combined with a previously described fluorescence lifetime plate-reader (FLTPR) that achieves a similarly high level of performance using nanosecond time resolution, is ready for HTS. This study demonstrates an initial application.

The specific target in this work is sarco/endoplasmic reticulum calcium ATPase (SERCA) [61, 114]. which has therapeutic relevance for a wide range of diseases, including

heart failure [114], multidrug-resistant leukemia [145], and type II diabetes [54]. SERCA is a critical enzyme, as it maintains calcium homoeostasis by actively pumping calcium from the cytosol into the endoplasmic or sarcoplasmic reticulum. Over a dozen human SERCA isoforms have been described, each with tissue-specific expression and distinct structural and functional characteristics. Specialized SERCA isoforms are predominantly found in electrically-excitable cells, such as myocytes and cardiomyocytes, where calcium-cycling is necessary for the contractile apparatus to function properly [34].

Recently, SERCA-based therapy based on calcium up-regulation by percutaneous administration of gene therapy was tested in cardiac disease clinical trials (CUPID study). SERCA overexpression by administration of adeno-associated virus (AAV), delivered directly to the hearts of patients experiencing end-stage heart failure, was shown to correct deficits in SERCA2a (cardiac-isoform) expression and activity, known to be correlated to impairment in cardiac (diastolic) function [53]. Despite encouraging early results, SERCA AAV gene therapy failed to meet primary end goals in phase IIb clinical trials. This failure was attributed to the limitations of AAV gene therapy, including the development of neutralizing antibodies [58], and difficulties of maintaining constant, long-term expression of the large 110 kD enzyme. We continue to explore alternative SERCA-based gene therapy strategies [146-148] but are also actively pursuing the search for small-molecule SERCA effectors capable of ameliorating the SERCA malfunction found in numerous degenerative diseases [34].

Initial screening campaigns evaluated structural perturbations using a reconstituted membrane system and fluorescence resonance energy transfer (FRET) detection between

SERCA and its regulatory partner phospholamban (PLB). In these studies, conventional fluorescence emission spectral recording was utilized for large-scale screening, and resulted in the discovery of small-molecule activators of SERCA [61]. We continued our development of SERCA biosensors by engineering a genetically-encoded intramolecular FRET sensor; donor and acceptor fluorescent proteins were fused to specific locations on SERCA's cytoplasmic headpiece, known to undergo large-scale, physiologically-relevant, structural changes (5-10 nm), as depicted by the known crystal structures [21],[114], This type of assay lends itself naturally to a structure-based screening campaign, in which the results are not only related to variation of compound structure, but also to variation of specific structural changes in the labeled target.

This two-color SERCA (2CS) biosensor utilizes green and red fluorescent proteins as a FRET pair. These red-shifted fluorescent proteins are less sensitive to cell autofluorescence and fluorescent compound interference, compared with their blue-shifted CFP and YFP counterparts. The existence of multiple 2CS FRET populations was previously identified using single-molecule fluorescence lifetime microscopy [113]. These studies elucidated SERCA's sensitivity to PLB and calcium, revealing insights into residues involved in this structure-activity relationship [149]. This set the stage for a proof-of-principle structure-based small-molecule screen, using a prototype fluorescence lifetime (FLT) microplate reader [114],[116], This seminal study proved that a genetically-encoded FRET sensor could be stably expressed in human embryonic kidney (HEK293) cells and utilized for HTS in a microplate format.

The present work utilizes a novel top-read fluorescence lifetime plate reader, which involves an epi-illumination geometry, thereby allowing for temperature control and the use of inexpensive black-bottom 384- or 1536-well plates. The preceding article established the technical feasibility of decomposing the fluorescence emission spectra into a linear combination of component spectra, from which the FRET efficiency (FRET) can be calculated. That study demonstrated high screening quality (high Z' value) and the ability to resolve minute FRET changes (0.5%), even when the cellular autofluorescence was artificially increased. This study involves screening a small-molecule library (National Clinical Collections 1 & 2), which contains a collection of compounds that have already been evaluated in pre-clinical and clinical trials. The ability to accurately determine changes in FRET from the 2CS biosensor from two independent fluorescence measurements (spectral and lifetime) increases the confidence of hit selection.

5.3 Materials and Methods

Cell Culture

HEK293 (originally derived from human embryonic kidney) cells were maintained in phenol red-free DMEM from Gibco (Waltham, MA) supplemented with 2 mM GlutaMAX (Gibco), 10% fetal bovine serum (FBS), from Atlanta Biologicals (Lawrenceville, GA), and 1 IU/mL penicillin/streptomycin (Gibco) and grown at 37° C with 5% CO_2. HEK293 cell lines were used to generate stable clones overexpressing the FRET-based biosensors and corresponding donor and acceptor labeled control cell lines [114]. Three days prior to screening, the stable cell lines were expanded in five T225 flasks from Corning Inc. (Corning, NY). On each day of screening and FRET hit retesting,

approximately 300 million cells were harvested by treatment of Tryple from Invitrogen (Carlsbad, CA), washed three times in phosphate buffer solution (PBS) with no magnesium or calcium from Thermo Scientific (Waltham, MA) by centrifugation at 300 g, filtered using 70 μm cell strainers (Corning), and diluted to 10^6 cells/mL using an automated countess cell counter (Invitrogen). On each day of screening, cell viability was assessed using the trypan blue assay.

After resuspension and dilution in PBS, the cells were constantly and gently stirred using a magnetic stir bar at room temperature, keeping the cells in suspension and evenly distributed to avoid clumping. During screening, cells were then dispensed into five 384 well assay plates, one containing no compound, one containing eight-point concentration curves of three known SERCA effectors, and three containing the NCC libraries 1 and 2. The same methods were applied for subsequent FRET testing of the reproducible hits identified in the pilot screen. Concentration-response curves (CRC) of the FRET hits were assessed at multiple time points by repeatedly scanning the 384-well plates. HEK293 stable clones expressing either the D1ER calcium FRET sensor (CFP/YFP) or the 2CS biosensor were used to evaluate the hits. The D1ER calcium sensor monitored changes in endoplasmic reticulum [Ca^{2+}] [131, 132]. The methods and protocols for the D1ER cells were identical to those for 2CS, with the exception that they were evaluated only in spectral mode, and the 384-well plates containing compound CRCs were scanned every three minutes for two-hours.

Liquid dispensing

Cells were dispensed using a Multidrop Combi liquid dispenser from Thermo (Pittsburg, PA), at a density of 10^6 cells/mL. Compounds were diluted in DMSO and dispensed either using an automated Echo acoustic liquid dispenser from Labcyte (Sunnyvale, CA) or a Mosquito liquid dispenser from TTP Labtech (Melbourn, UK).

Cells and compound mixtures were dispensed into 384-well flat, black-bottom polypropylene plates from Greiner (Kremsmünste, Austria). The cells were dispensed at room temperature into plates containing test compounds. They were incubated with compound for 20, 60, 90, and 120 minutes, and then scanned in both lifetime and spectral modes. 727 compounds from the NCC 1 and 2 compound libraries were purchased from Evotec (Hamburg, Germany), formatted into 96-well mother plates using a Biomek FX liquid dispenser from Beckman Coulter (Brea, CA), and subsequently formatted across three 384-well plates at 50 nL (10 µM final concentration per well) using an Echo liquid dispenser from Labcyte. Control wells containing matching %v/v DMSO were formatted into unused wells and columns 1, 2, 23, and 24 of the assay plates. The eleven reproducible FRET hits were purchased from three different vendors Sequoia Sciences (Saint Louis, MO), Tocris (Minneapolis, MN), or Santa Cruz (Santa Cruz, CA) depending on their availability.

Instrumentation and Data Analysis

An in-depth description of the fluorescence instrumentation is described in the previous article [150] and in the supplemental material. For lifetime mode, the observed fluorescence waveform was convolved with the instrument response function, and the average energy transfer efficiency ($E = 1- \tau_{DA}/\tau_D$) was calculated from the average lifetimes

of donor τ_D and donor-acceptor, τ_{DA}, FRET cell lines. The structural correlates for FRET were modeled as previously described [151-153], assessing the nanosecond time dependence of the TR-FRET waveforms according to (Eq. 11)-(Eq. 16):

$$F_D(t) = \sum_{i=1}^{2} A_i \, exp\left(-t/\tau_i\right) \quad \text{(Eq. 11)}$$

$$F_{\mathrm{DA}}(t) = \sum_{\mathrm{j}=1}^{2} X_{\mathrm{j}} \cdot T_{\mathrm{j}}(t) \quad \text{(Eq. 12)}$$

$$F(t) = x_{\mathrm{D}} F_{\mathrm{D}}(t) + x_{\mathrm{DA}} F_{\mathrm{DA}}(t) \quad \text{(Eq. 13)}$$

$$T_{\mathrm{j}}(t) = \int_{-\infty}^{\infty} \rho_{\mathrm{j}}(R) \cdot \sum_{i=1}^{3} A_{\mathrm{i}} \, exp\left(\frac{-t}{\tau_{\mathrm{i}}} \cdot \left[1 + \left(\frac{R_{0\mathrm{i}}}{R}\right)^6\right]\right) dR \quad \text{(Eq. 14)}$$

$$\rho_{\mathrm{j}}(R) = \frac{1}{\sigma_{\mathrm{j}}\sqrt{2\pi}} \exp\left(\frac{-\left[R - R_{\mathrm{j}}\right]^2}{2\sigma_{\mathrm{j}}^2}\right) \quad \text{(Eq. 15)}$$

$$\sigma_{\mathrm{j}} = \mathrm{FWHM_j}/\left(2\sqrt{2\ln 2}\right), \quad \text{(Eq. 16)}$$

where F_{D} is the time-resolved fluorescence decay function of the GFP donor (Eq. 11), best-fit by a two exponential decay (**Figure S37**). F_{DA} (Eq. 12) is the time-resolved fluorescence decay function of the GFP donor-acceptor FRET sample. F_{D} and F_{DA} were fit to a linear combination of mole fractions of x_{D} and x_{DA}. x_{D} equals zero for the intramolecular FRET sensor (Eq. 13). F_{DA} is a linear combination with molar fraction X_j of two FRET-affected fluorescence decays $T_j(t)$ (Eq. 14). ρ_{j} is the probability of each distance distribution, determined by least-squares minimization of the distance (nm) R, associated with each donor-acceptor lifetime species τ_{i} (Eq. 15). (σ_{j}) Gaussian interprobe distance distributions centered at R_j = 5.5 nm and 10.2 nm, with distribution widths defined by the standard deviation and full-width half-maximum (Eq. 16). The Förster distance (R_0) for the eGFP and tagRFP FRET pair is 5.8 nm. The parameters in this system of equations were optimized utilizing simultaneous least-squares minimization to waveforms from

donor-only and donor-acceptor cell lines. The best-fit model was indicated by minimized χ^2 and by evaluation of the parameter error surface as described in our previous publications [151-153].

For spectral detection, the observed fluorescence emission spectrum was fitted by least-squares minimization to a linear combination of component spectra:

$$F_{\mathrm{Fit}}(\lambda) = aF_{\mathrm{D}}(\lambda) + bF_{\mathrm{A}}(\lambda) + cF_{\mathrm{C}}(\lambda) + dF_{\mathrm{W}}(\lambda) \quad \text{(Eq. 17)}$$

where D is donor, A is acceptor, C is cell autofluorescence, and W is water Raman, and *a*, *b*, *c*, *d* are the coefficients determined from the fit.

$$FRET = \frac{FR \times QR - AR}{1 + FR \times QR} \quad \text{(Eq. 18)}$$

For an intramolecular FRET sensor, having both donor D and acceptor A, FRET was determined from (Eq. 9), where QR is the ratio of quantum yields (Q_D/Q_A) in the absence of FRET, AR is the ratio of molar absorptivities ($\varepsilon_A/\varepsilon_D$), both obtained from reported values [123]. QR is corrected for spectrograph sensitivity at the appropriate wavelength (**Figure S36**). The only experimental observable in (Eq. 9) was FR.

$$FR = \frac{Acceptor\ emission}{Donor\ emission} = \frac{bF_A}{aF_D}. \quad \text{(Eq. 19)}$$

Full derivation of (Eq. 17)-(Eq. 19) can be found in the supplementary material.

HTS Data Analysis

Fluorescent compounds were identified and flagged as potential false-positives by evaluating the similarity index (SI) between an observed compound spectrum $I_i^{(a)}$ and DMSO control spectra $I_i^{(b)}$:

$$SI = 1 - \frac{\sum I_i^{(a)} \cdot I_i^{(b)}}{\sqrt{\sum I_i^{(a)} \cdot I_i^{(a)}} \sqrt{\sum I_i^{(b)} \cdot I_i^{(b)}}} \quad \text{(Eq. 20)}$$

The spectra of 192 DMSO control wells (%v/v DMSO) were averaged for each screen to generate a single control spectrum ($I^{(b)}$). The fluorescence spectra of the two-color SERCA biosensor, screened against 727 separate compounds ($I^{(a_{1-727})}$), was compared with the single DMSO control spectrum. The similarity index between the spectra was computed over the GFP emission wavelength (i = 500-540nm). The fluorescent compound threshold was set to flag potential false-positives with an SI greater than $2x10^{-4}$ throughout the screens.

Enzymatic SERCA activity assays of FRET hits

Functional assays were performed using rabbit light skeletal sarcoplasmic (SR) vesicles [114]. An enzyme-coupled, NADH-linked ATPase assay was used to measure SERCA ATPase activity in 96-well microplates. Each well contained 50 mM MOPS (pH 7.0), 100 mM KCl, 5 mM $MgCl_2$, 1 mM EGTA, 0.2 mM NADH, 1 mM phosphoenol pyruvate, 10 IU/mL of pyruvate kinase, 10 IU/mL of lactate dehydrogenase, 1 μM of the calcium ionophore A23187 from Sigma (St. Louis, MO), and $CaCl_2$ added to set free [Ca^{2+}] to 10 μM [154]. 4 μg/mL of SR vesicle, calcium, compound, and assay mix were incubated for 20 min. The assay was started upon the addition of ATP, at a final concentration of 5

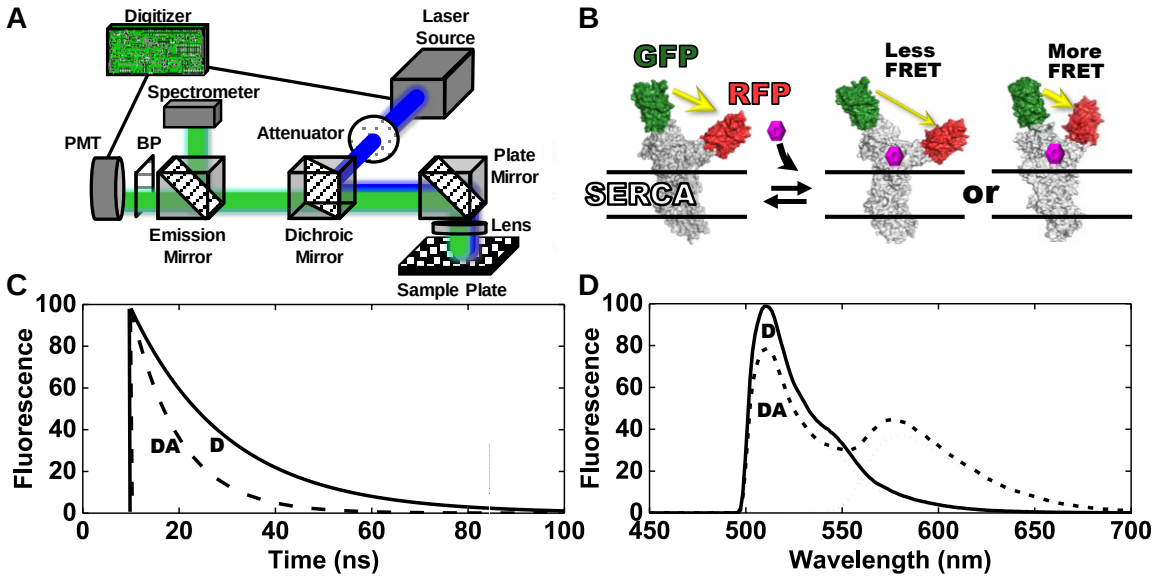

Figure 38 Overview of high-throughput spectral and lifetime FRET drug screening. (A) Diagram of the instrument. (B) The two-color SERCA (2CS) intramolecular FRET biosensor.[112-114] As depicted, the FRET efficiency is dependent on the structural status of SERCA's domains, which may be affected by the binding of small molecules. Conceptual data (**C**, lifetime mode) and (**D**, spectral mode) illustrate the dependence of fluorescence signals on FRET. Solid black curve (D): donor only (no FRET). Dashed black curve (DA): donor plus acceptor (FRET). In (**D**) dotted curves show the resolution of the spectrum into components corresponding to donor (GFP) and acceptor (RFP) emission.

mM (total volume to 200 μL), and absorbance read in a SpectraMax Plus microplate spectrophotometer from Molecular Devices (Sunnyvale, CA).

5.4 Results

High-precision FRET efficiency determinations from two independent fluorescence measurements

The sarco/endoplasmic reticulum calcium ATPase (SERCA) cycles through multiple conformations as it pumps calcium into the sarcoplasmic reticulum. Briefly, a green fluorescent protein (GFP) was fused to the N-terminus of SERCA and a red fluorescent protein (RFP) was fused to a flexible intrasequence loop located on the nucleotide-binding domain of SERCA. The distance between these two fluorescent proteins can be measured by determining the rate of fluorescence resonance energy transfer (FRET). This two-color SERCA (2CS) biosensor was stably expressed in a human

embryonic kidney (HEK293) cell line, and grown in sufficient quantities for high-throughput screening [114]. The binding of potential small-molecule effectors is directly evaluated as changes in FRET (**Figure 38B**).

Conceptual fluorescence lifetime waveforms are depicted in **Figure 38C**. In the actual lifetime measurements, typically 1000 laser pulses are averaged over a 200 ms interval, to generate an entire decay waveform for each well of a 384-well plate. The fluorescence lifetimes τ_{DA} (FRET biosensor with donor and acceptor) and τ_D (donor-only control) are used to determine the energy transfer efficiency FRET = $1 - \tau_{DA}/\tau_D$. A representative complete fluorescence emission spectrum acquired with a 100 ms integration time at 0.5 nm spectral resolution in spectral mode is shown in **Figure 38D**. The high-quality emission spectrum, acquired from a single well was decomposed into a linear combination of its spectral components green fluorescent protein (GFP) and red fluorescent protein (RFP). These components were then used to solve for the contribution of the fluorescence emission from GFP (donor fit) and RFP (acceptor fit), allowing for a high-precision determination of an ensemble-averaged FRET from the 2CS biosensor.

Global lifetime analysis resolves structural status of 2CS biosensor

Global analysis of the fluorescence intensity decay rate (lifetime mode) was used to resolve two distinct structural states of the 2CS biosensor (Eq. 11)-(Eq. 16). These distinct structural states of 2CS were previously resolved using single-molecule fluorescence microscopy [113], which is not a high-throughput detection method. Here, we demonstrate analogous structural resolution of the 2CS biosensor, except with an ensemble-averaged FRET measurement, acquired in 200 ms per well from live-cell suspensions.

FRET is a sensitive spectroscopic molecular ruler, due to the R^{-6} distance dependence of the rate of energy transfer from an excited donor fluorophore (GFP) to an acceptor (RFP) in the ground state [107]. The exceptionally good precision of direct waveform recording (DWR) and global analysis of the fluorescence decay waveforms produced in this fashion allow FRET measurements to be evaluated in terms of distance distributions and mole fractions of physiologically-relevant structural states. Fluorescence lifetime waveforms were analyzed using a global two-component model (Eq. 11)-(Eq. 16), yielding a two-state structural model for SERCA's cytosolic headpiece**,** describing an equilibrium between the open (102 nm) and closed (55 nm) structural states with full-width at half-maximum (FWHM) of 69 and 22 nm; respectively. The Gaussian distance distribution was determined for each structural state and plotted as a histogram in **Figure 39A**. The distance R and FWHM fitting parameters were allowed to vary globally, and the

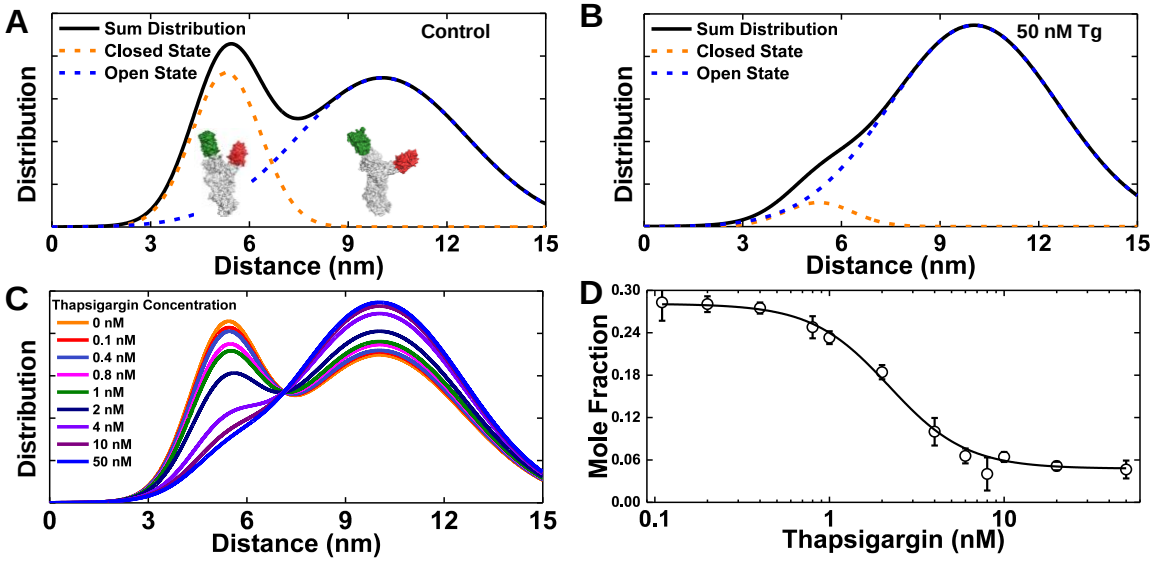

Figure 39. Lifetime analysis of time-resolved fluorescence decay waveforms resolves structural states of the 2CS biosensor. (**A**) Two structural states of SERCA are resolved, corresponding to two Gaussian interprobe distance distributions, consistent with a two-state structural model with an equilibrium between closed (5.5 nm FRET distance, orange) and open (10.2 nm FRET distance, blue) structural states. (**B**) The addition of a saturating dose (50 nM) of the known inhibitor thapsigargin (Tg) shifts this equilibrium substantially toward the open state. (**C**) Concentration dependence of Tg effect on the structural distribution (n= 8 wells for each concentration). (**D**) Plot, based on (C), of closed state mole fraction vs Tg.

mole fraction of each state was determined according to the two-component global fit (Eqs. 1-6). Thapsigargin inhibits SERCA at nanomolar concentration, and perturbs SERCA2a's cytosolic headpiece, greatly increasing the population of the more open and disordered structural state at 50 nM (**Figure 39B**). The full concentration dependence is illustrated in (**Figure 39C**), and the concentration-response curve of the closed state mole fraction (**Figure 39D**) yields an EC_{50} value of 2.2 nM thapsigargin in agreement with the known EC_{50} for SERCA inhibition [155].

Pilot screening of NCC libraries to evaluate both spectral and lifetime FRET detection

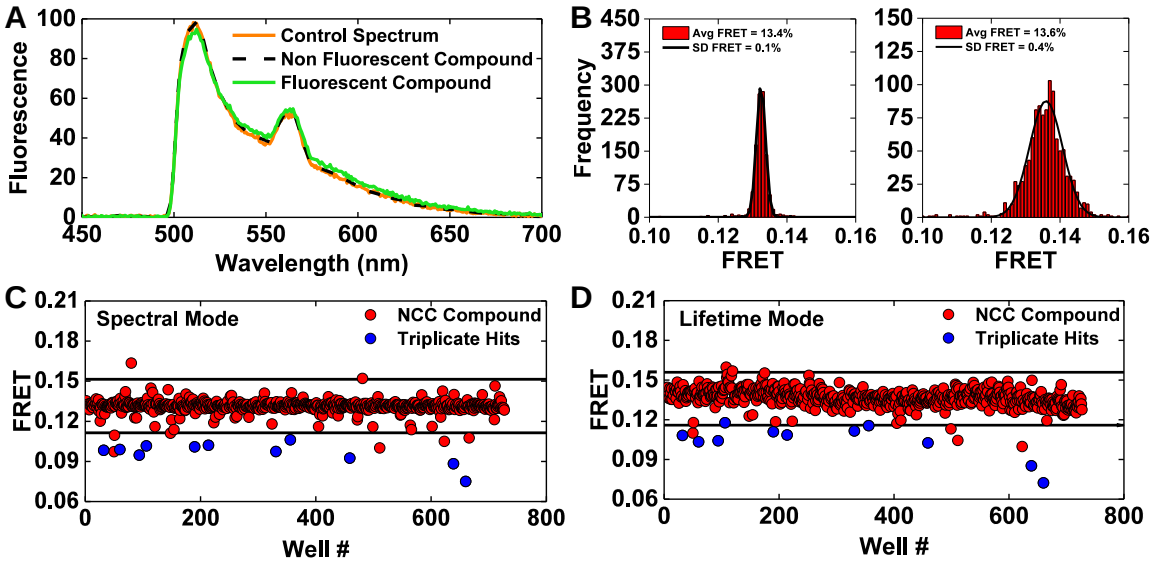

Figure 40. Spectral and lifetime pilot drug screening. (**A**) Fluorescence emission spectra were used to identify and flag potential interference from fluorescent compounds by assessing the similarity index (Eq. 20) of each well from a pilot screen of the NCC1 & 2 small-molecule libraries. A control spectrum (%v/v DMSO well) and non-fluorescent (compound not identified as a FRET hit during screening with 2CS) have a high degree of similarity, as shown as direct overlap of orange and black spectrum. A slightly fluorescent compound is depicted by the green spectrum and was flagged as a potential false-positive hit. The fluorescent profile of all 1152 wells from one NCC screen was assessed using a stringent similarity index threshold; 44 compounds were flagged as potential false-positives due to interference from compound fluorescence. (**B**) Histogram plots of the wells from one NCC screen after removing potential fluorescent compounds. Gaussian fits depict an increase in precision from spectral mode (left) in comparison to lifetime mode (right), shown as the frequency of FRET efficiency determined by either method and a narrower distribution from spectral mode (average FRET calculated by spectral unmixing or lifetime and the standard deviation determined from the Gaussian fit). (**C**) One 2CS pilot NCC screen (spectral mode) is shown with a hit threshold set at a 0.02 change in 2CS FRET (4 SD). 16 FRET hits were identified in this screen. 11 of these 2CS FRET hits were found to be reproducible across three independent screens (blue). (**D**) The same 384-well plates were scanned in lifetime mode. 16 hits were identified using the same threshold set at a 0.02 change in 2CS FRET efficiency (3 SD). In this screen, nine of the reproducible 2CS FRET hits identified in spectral mode were also FRET hits as assessed by lifetime mode (blue).

A small-molecule library (National Clinical Collections 1&2), consisting of 727 compounds previously evaluated in preclinical and clinical trials, was used to evaluate both spectral and lifetime modes of the spectral unmixing plate reader (SUPR). After an initial quality control check of the 2CS cell line on each day of screening (response to known effectors and signal level), a HEK stable clone overexpressing the 2CS biosensor was dispensed, using a Multidrop liquid dispenser into 384-well plates, and then scanned in both spectral and lifetime modes after 20, 60, 90, and 120 minutes of incubation with the compounds or control wells.

A single-exponential fit was used to determine the lifetime τ_{DA} from 2CS and τ_D from the one-color SERCA2a donor-only control cell line. These lifetimes were used to determine FRET = 1- τ_{DA}/τ_D. In spectral mode, the observed spectrum acquired from each well was decomposed into a linear combination of components (GFP, RFP, cellular autofluorescence, and water Raman). The reference spectrum of each was used to solve for the total contribution of fluorescence emission from each component (Eq. 17). These values were used to calculate a fitted ratio of the total fluorescence emission of RFP/GFP (Eq. 19) and then FRET from the 2CS biosensor was determined using the simplified FRET equation for intramolecular FRET sensors as described in the preceding article (Eq. 9),[150].

Both lifetime and spectral fluorescence measurements are prone to interference from fluorescent compounds. We took advantage of the information contained in the full emission spectrum to develop a streamlined process to flag these potential false-positives. A spectral similarity index (Eq. 20), which monitors differences from the spectra of control

wells with no compound added, was computed in the donor only region. A stringent similarity index threshold ($2x10^{-4}$) was used to flag 44 compounds as potential false-positives, due to interference from compound fluorescence (**Figure 40A**).

Histogram plots from all wells that passed the fluorescence compound filter, from a single NCC screen demonstrate a three-fold increase in precision from the spectral mode, in comparison to lifetime mode, as exemplified by a narrower distribution **(Figure 40B**). These two complementary determinations of FRET were used to identify hits, quickly rule out false-positives, and increase reproducibility across screens.

From three independent screens of the NCC libraries at a time point of 20 min after compound incubation, eleven reproducible FRET hits were found. These hits were identified using the spectral unmixing method and a hit threshold set at a 0.02 change in FRET. The results from one 2CS NCC screen are depicted in **Figure 40C and D.** Based on triplicate screens, 11 out of 16 compounds were identified as reproducible FRET hits (shown as blue circles in **Figure 40C**). In lifetime mode, 9 of the 11 reproducible FRET hits found using spectral mode were also reproducible lifetime hits **(Figure 40D**).

Reproducibility of hit identification across independent screens and time course studies

The reproducibility of 2CS FRET hits identified across three independent screens in spectral mode, after 20 min compound incubation at 10 µM concentration, is depicted in **Figure 41A**. The change in 2CS FRET (Δ FRET) of each hit from three independent NCC screens remained nearly constant from one screen to the next. For purposes of directly evaluating the use of the spectral recording method, a hit threshold of a 0.02 negative change in FRET (red bar) was applied and will be used from here on. When these same hits were evaluated in lifetime mode, nine of the eleven spectral FRET hits were found to

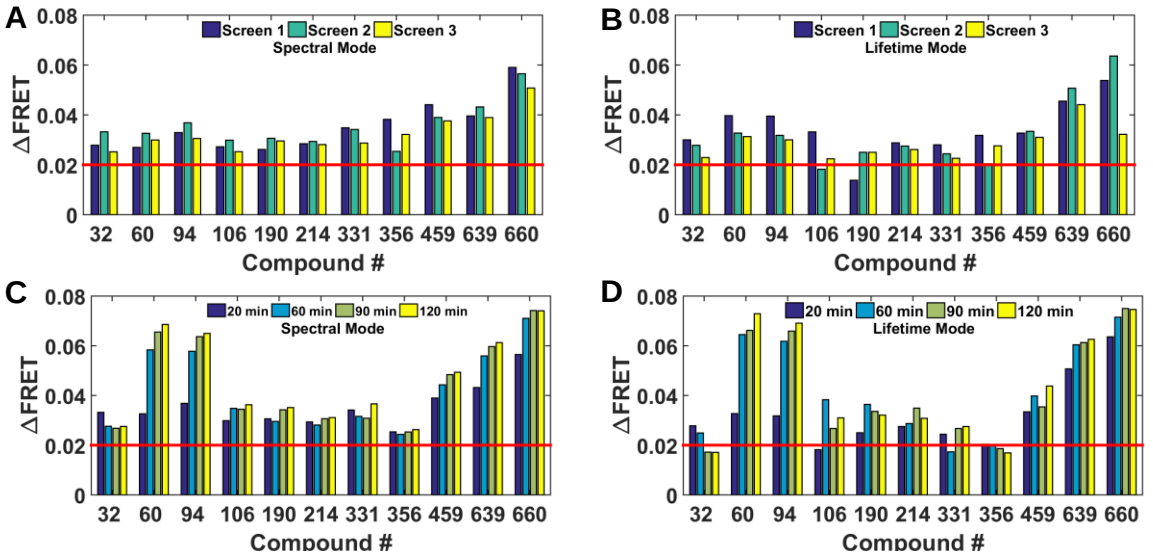

Figure 41. Reproducible FRET hits assessed across independent screens and time course studies. (**A**) Spectral mode identified eleven reproducible 2CS FRET hits using a threshold of 0.02 change in FRET (red line). The reproducibility of each 2CS FRET hit, after 20 min incubation, across three independent screens is shown. The ΔFRET from each compound remains consistent from screen to screen. ΔFRET was calculated by assessing the change in FRET of 2CS from the average FRET, determined by the Gaussian fit of all wells not flagged as fluorescence compounds. (**B**) Lifetime mode assessment of the eleven reproducible spectral FRET hits. Nine of the eleven FRET hits were reproducible (triplicate) hits using a 0.02 FRET threshold. Compounds #106 and190 were not identified as lifetime FRET hits in one of the three independent screens. (**C**) Spectral FRET hits evaluated by time-course studies. Each independent pilot screen was scanned in spectral mode after 20, 60, 90, and 120 minutes of compound incubation. The change in 2CS FRET efficiency (ΔFRET) of each compound is plotted and each reproducible FRET hit, identified as a hit using the spectral unmixing method, remained a hit over multiple time points. The 2CS FRET hits depicted here were from screen 2 (turquoise bars in A and B). Compounds #60, 94, 459, 639, and 660 exhibited an increased FRET change over time. (**D**) Lifetime FRET change evaluated by time-course studies. Ten compounds from screen 2 were identified as hits, after 20 minutes of compound incubation, using a threshold set at 0.02 FRET change (red bar). Compounds #32 and 356 displayed a modest reduction in 2CS ΔFRET at the later time points. Compounds # 60, 94, 459, 639, and 660 again exhibited an increased FRET change over time.

be reproducible hits **(Figure 41B**). Compounds #106 and190 were not identified as lifetime FRET hits in one of the three independent screens.

The ability to acquire lifetime and spectral measurements with scan times under three minutes for an entire 384-well microplate, allowed for the examination of 2CS FRET changes in response to the full NCC library of compounds at multiple compound incubation time points. Time-course screening may not be directly amenable to large-scale screening but is potentially highly applicable for assessing the reproducibility of a large number of FRET hits identified during a large-scale HTS campaign, at multiple concentrations. Time-dependent compound effects may also elucidate compounds with low binding affinities or delayed effects from low membrane permeability. These types of studies may also be useful for other fluorescence bioassays solely based on monitoring time-dependent effects, as we will depict later using the cameleon calcium FRET sensor. For these 2CS pilot screening studies, time-dependent screening was used to determine the inter-screen reproducibility of FRET hit identification as assessed both spectral and lifetime modes.

Time-dependent scans of reproducible 2CS FRET hits were consistent over multiple time points (20, 60, 90, and 120 min after compound incubation). The 2CS FRET hits analyzed here were from screen 2 (turquoise bars in **Figure 41A** and **B**) and show excellent reproducibility across time points. Five compounds # 60, 359, 459, and 639 exhibited an increased FRET change over time (**Figure 41C**). Reproducible hits were evaluated in lifetime mode (**Figure 41D**) Very subtle differences in the 2CS FRET changes were found across spectral and lifetime methods. Ten compounds from screen 2 were identified as hits, after 20 minutes of compound incubation. Compounds #32 and 356

displayed a modest reduction in 2CS ΔFRET at the later time points. Compounds #60, 94, 459, 639, and 660 again exhibited an increased FRET change over time. Overall, both methods show excellent agreement in terms of the direction and magnitude of FRET change.

Multi-parameter concentration-dependent effects of FRET hits

The reproducible 2CS FRET hits were further evaluated as a function of concentration. Compounds were dispensed into 384-well plates, across an eight-point concentration-gradient (n=4 for each concentration). Three independent dose-dependent FRET tests were performed on the 2CS FRET hits. Six compounds that produced the largest reproducible FRET change after 120 minute compound incubation are depicted.

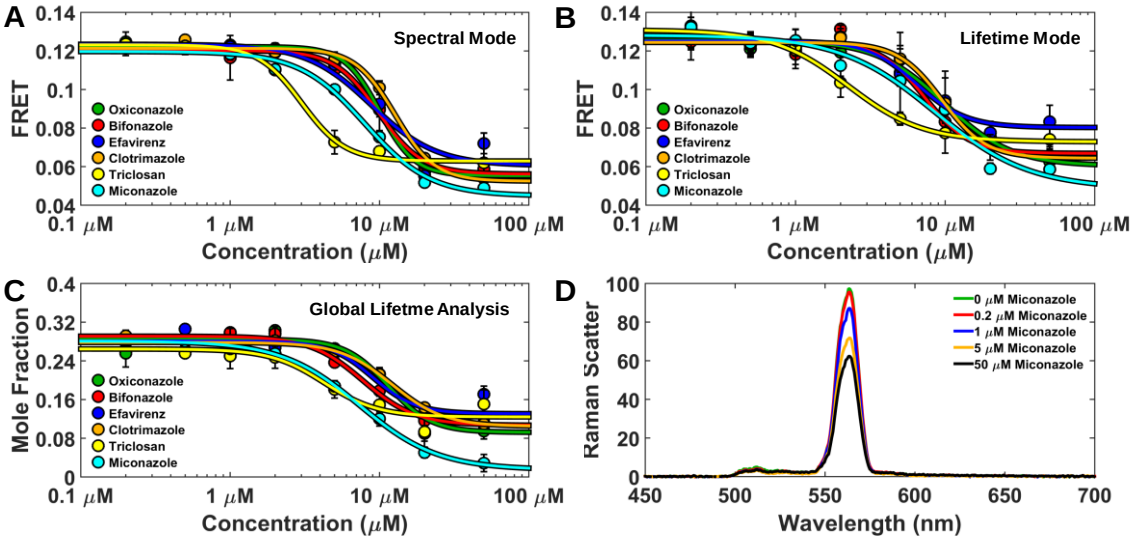

Figure 42. Multi-parameter concentration-dependent effect of FRET hits (**A**) Spectral mode analysis of the reproducible 2CS FRET hits. Compounds were dispensed into 384 well plates, across an eight-point concentration-gradient (n=4 for each concentration). Six representative compounds produced a dose-dependent FRET change as evaluated in spectral mode. These compounds altered FRET with micromolar affinities with subtle differences across the compounds. (**B**) The same 384-well plate was evaluated using lifetime mode and demonstrated excellent agreement in the dose-dependent FRET change across two independent FRET measurements. (**C**) Global analysis of the lifetime data depicts a dose-dependent change in the mole fraction of the closed 2CS headpiece (5.5 nm distance distribution). Using this distance distribution model, the confirmed reproducible hits perturbed the 2CS structural equilibrium between open and closed states. All of the hits decreased 2CS FRET, indicating increased distance between GFP and RFP. (**D**) Water Raman spectrum acquired from compound-only wells of the known compound aggregator miconazole demonstrates ultra-high-sensitivity of spectral recording. Compound aggregation dose-dependently causes more light to be absorbed and decreases inelastic light scattering (Raman band).

These compounds dose-dependently decreased 2CS FRET as determined by spectral mode (**Figure 42A**). Each FRET curve was fit using the Hill equation. Decreased 2CS FRET was observed at micromolar concentrations with notable differences in the apparent EC_{50} (half maximal effective concentration) of the FRET curve. The same 384 well plate, containing the reproducible hits, was evaluated in lifetime mode with a simple, single exponential fit (Eq. 12) and demonstrated great agreement between the FRET changes across the two modes of independent FRET measurements. **(Figure 42B**).

The compounds found to be reproducible hits and that exhibited dose-dependent FRET changes all decreased 2CS FRET. The imidazole antifungal clotrimazole was a hit and has been previously shown to inhibit SERCA function [156]. The related compounds oxiconazole, bifonazole, and miconazole were also hits. The antibacterial triclosan has been shown to increase cytosolic calcium [157] but to our knowledge not through interaction with SERCA.

Global analysis of the lifetime data (Eq. 11)-(Eq. 16)resolved a dose-dependent change in the mole fractions of the open and closed structural states. Using this distance distribution model, the reproducible hits perturbed the 2CS structural equilibrium between open and closed states in **Figure 42C** (5.5 nm distance distribution shown). The high sensitivity of spectral mode is shown by the fluorescence signal of the water Raman spectrum. Raman scattering was acquired from compound-only wells of the known aggregator miconazole [158]. Compound aggregation dose-dependently causes more light to be absorbed and decreases inelastic light scattering (Raman band) (**Figure 42D**). This

information may become useful for flagging potential false-positives due to compound aggregation.

Functional characterization of FRET hits on SERCA ATPase activity and ER calcium content

Functional assays of the confirmed reproducible NCC hits were used to assess the relationship of hits that perturb 2CS structure and their effects on SERCA function. The ATPase activity of purified SERCA was measured after 20 minute incubation with a saturating dose of buffered free calcium (10 µM) and titration of each compound.

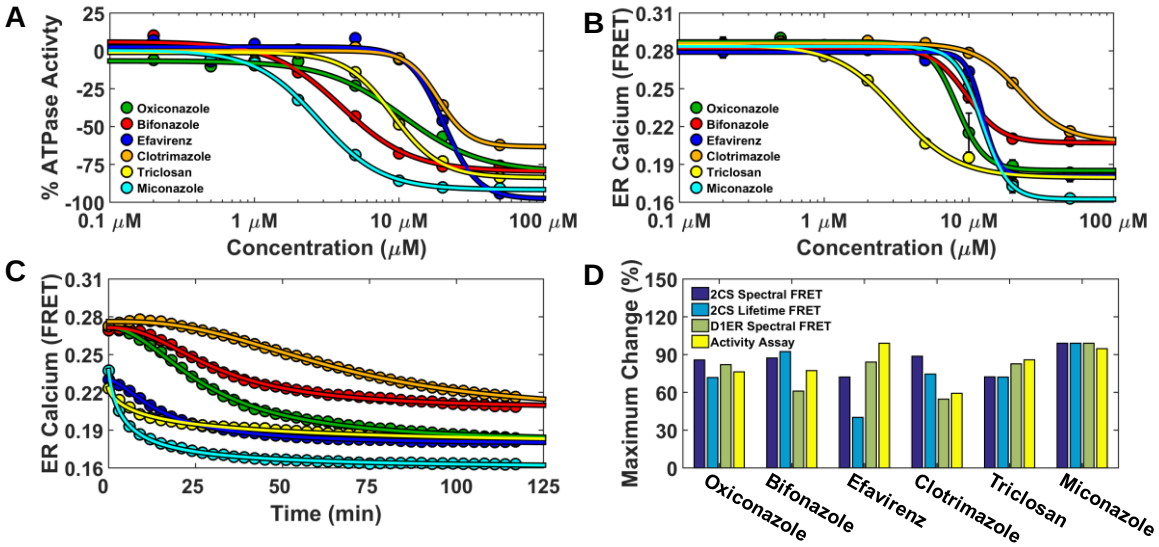

Figure 43. Functional characterization of FRET hits on SERCA ATPase activity and ER calcium content. (**A**) 2CS FRET hits inhibit SERCA ATPase activity. NADH-enzyme coupled activity assay of purified SERCA was measured at eight different concentrations of the reproducible FRET hits. The maximal rate of SERCA activity was measured at saturating calcium (10 µM) after 20 minute incubation with compounds and dose-dependent inhibition was observed. (**B**) Endoplasmic reticulum calcium was depleted by the 2CS FRET hits. ER calcium was monitored in live-cells overexpressing the endoplasmic reticulum localized calcium FRET sensor (D1ER). D1ER FRET is dependent on calcium concentration, where less calcium causes a reduction in FRET. ER calcium levels were monitored over time in response to an eight-point concentration gradient of each hit compound. A 384 well plate was repeatedly scanned (every three minutes) with D1ER cells. The dose-dependent FRET change (ER calcium depletion) after 120 minutes compound incubation is shown and depicts differential depletion at each compound concentration. (**C**) Maximal ER calcium depletion in the presence of a saturating dose (50 µM) of each compound (decreased D1ER FRET) was assessed over a 120 minute period. The 2CS FRET hits displayed time-dependent and compound-specific ER calcium depletion. Miconazole (turquoise) exhibited both maximal SERCA ATPase Vmax inhibition and the largest amount of ER depletion. (**D**) Structure and activity assay correlation of 2CS FRET hits. The maximal change (percent change) of the structural FRET change from the 2CS FRET biosensor as well as the maximal change from two different functional assay (ATPase activity assay and D1ER calcium depletion).are shown.

Experiments were performed in triplicate with eight-point concentration curves. The top six hits were found to dose-dependently inhibit SERCA's ATPase function (**Figure 43A**). The antifungal Miconazole shows almost complete inhibition (92.4%) with a K_i of 2.8 µM. Clotrimazole's ability to inhibit SERCA's ATPase was slightly reduced in comparison with a K_i of 17.3 µM which is in agreement with previous steady-state measurements (7-35 µM) [156].

SERCA malfunction can result in decreased ATPase activity and/or calcium pumping efficiency. ER calcium content was monitored over time using the endoplasmic-localized cameleon calcium FRET sensor (D1ER) [132]. As demonstrated in the preceding article, known SERCA inhibitors deplete ER calcium in a time and dose-dependent manner and can be monitored using live-cells expressing D1ER. Briefly, D1ER FRET changes were monitored over time by repeatedly (every 3 minutes) scanning a 384-well plate containing varying concentrations of the 2CS FRET hits. D1ER cells were assessed immediately after compound incubation. These plates were scanned only in spectral mode using 434 nm excitation with a laser-driven light-source, to acquire a full emission spectrum from each well. The appropriate CFP/YFP reference spectra were used to determine FRET using (Eq. 8).

D1ER FRET curves were determined for each time-point scan, after compound incubation, over a period of 120 minutes (40 scans total). The 2CS FRET hits displayed time-dependent and compound-specific ER calcium depletion. Miconazole (turquoise) exhibited both maximal SERCA ATPase Vmax inhibition and the largest amount of ER calcium depletion as depicted at the final 120 min time point in **Figure 43B**. Maximal ER

calcium depletion in the presence of a saturating dose (50 μM) of each compound (decreased D1ER FRET) was assessed over a 120 minute period (**Figure 43C**). The 2CS FRET hits displayed time-dependent and compound-specific ER calcium depletion. The K_I and EC_{50}'s from the ATPase activity and D1ER FRET curves showed good agreement at the 20 minute time points. The structure-activity relationship of the 2CS FRET hits was further analyzed by comparing 2CS FRET (both spectral and lifetime mode), ATPase activity, and ER calcium depletion (**Figure 43D**). The maximal change (shown as percent change) of the structural FRET change from the 2CS FRET biosensor had excellent agreement with the maximal change from two different functional assays (ATPase activity assay and ER calcium depletion). Structural perturbation of the 2CS FRET biosensor directly relates to a compound's effect on SERCA function.

5.5 Discussion

This study illustrates the complementary combination of spectral and lifetime fluorescence detection for the purposes of HTS. The spectral unmixing method increases the precision of hit identification and reproducibility of the hits in concentration-response curves (**Figure 41**). The fluorescence lifetime detection mode offers excellent precision and offers the additional advantage of structural resolution, revealed by multi-exponential global lifetime fitting. This approach resolves multiple FRET populations and assesses them in terms of distance-distributions and mole fractions, assigned to structurally-relevant perturbations of SERCA effectors (**Figure 39**). This resolution of multiple FRET-detected structural states from a live-cell biosensor is highly advantageous for screening, offering the potential to elucidate chemotypes or classes of compounds, identified in large-scale

screens, which differentially alter the structural status of a biosensor. This high-content information can be used to generate structure-activity relationships based on binding-affinities, structural dynamics, and disorder.

The capability to couple two independent measurements of FRET, thereby substantially decreasing the false-positive rate, would be of significant value to the high-throughput screening community. Spectral recording does not offer the resolution of structural information, in terms of resolving multiple structural states, but can be used to identify fluorescent compounds, eliminate artifacts due to dispenser error or contaminated samples, and increase assay precision across screens (**Figure 40**).

This is the first microplate reader capable of direct waveform recording in both lifetime and spectral domains. A recent review of fluorescence lifetime imaging (FLIM) plate readers demonstrates the medium-throughput capabilities currently offered by other technologies (20 min scan times per 96 well plate) [159]. The approach described here is considerably faster, yet offers very high precision.

Beyond developing new fluorescence technology, the overarching goal of this research is to identify novel small-molecule SERCA effectors with therapeutic potential for multiple disease states. These studies employed a 2CS biosensor based on the SERCA2a isoform [114], which is the primary isoform expressed in the heart. We have engineered constructs based on the other human isoforms, with the intent of performing drug-discovery campaigns to identify isoform-specific SERCA effectors. Further, we are currently developing new synthetic analogues based on our previously identified SERCA activators and inhibitors, where our HTS approach allows us to quickly assess and triage

the most prominent candidates from a large pool of synthetically-derived analogues. We concluded this assay-based demonstration by investigating hits identified through structural-based screening, using an NADH-enzyme coupled ATPase activity assay and the D1ER endoplasmic reticulum-targeted calcium sensor to evaluate the correlation between the structure and function of hits identified in this pilot screening campaign (**Figure 43**).

The compounds identified during these pilot screens all decreased FRET from the 2CS biosensor, corresponding to opening of SERCA's cytoplasmic headpiece. This may be a consequence of their similarity in the mode of binding or mechanism of inhibition. However, the 2CS biosensor is not limited to detection of decreases in FRET. In broken cells, we have previously shown that ligands such as calcium increase FRET, due to closure of SERCA's cytoplasmic headpiece [112]. It is plausible that the maximal FRET effect is essentially reached for the HEK293 live-cells, in which calcium and ATP maintain SERCA in its closed structural state.

The novel paradigm used in the present study enables the measurement of multiple FRET parameters. These high-content assays are ideally suited for high-throughput screening campaigns, with potential to discover novel allosteric effectors, which may differentially perturb FRET. This strategy is now being evaluated for use on homogenate and microsomal cellular preparations using FRET-based biosensors. These applications allow for fine control of environment (calcium, nucleotide, pH, etc.). Preliminary results have demonstrated that these purified preparations of FRET-based biosensors are suitable for counter screens and also in-depth structural evaluations of novel SERCA effectors.

The high-resolution FRET approach, coupled to functional assays, is applicable to a wide range of protein targets, including the ryanodine receptor [160], myosin [152, 161], phospholamban [148], multiple-drug resistance receptor [162], and the tumor necrosis receptor [163]. The ability to quickly and reliably assess structural perturbations from biosensors in relation to physiologically-relevant functional changes holds high promise for the development of allosteric effectors and potentially valuable lead compounds.

Declaration of Conflicting Interests

Dr. Thomas holds equity in and serves as an executive officer for Photonic Pharma LLC. This relationship has been reviewed and managed by the University of Minnesota.

Acknowledgments

Jesse E. McCaffrey, Bengt Svensson, Razvan L. Cornea, and J. Michael Autry provided helpful discussions, and Octavian Cornea prepared the manuscript for publication. Simon J. Gruber and Seth L. Robia developed many of the reagents and materials used. Fluorescence microscopy was performed at the UMN Imaging Center, flow cytometry at the UMN Lillehei Heart Institute, compound dispensing at the UMN Institute of Therapeutic Drug Discovery and Development, and spectroscopy was performed at the UMN Biophysical Technology Center. pcDNA-D1ER was a gift from Amy Palmer & Roger Tsien (Addgene plasmid # 36325).

Funding

The authors disclosed receipt of the following financial support for the research, authorship, and/or publication of this article: This work was supported by NIH grants R42DA037622 (to G.D.G and D.D.T.), R01GM27906 (to D.D.T.), and R01HL129814 (to

D.D.T.). T.M.S. was supported by the NIH Chemistry-Biology Interface Training Grant (5T32GM008700), and by predoctoral fellowships from 3M and Arnold H. Johnson.

Chapter 6 – Summary and Future Directions

This research demonstrates new technological advances for high-throughput drug screening with FRET biosensors. The cardiac calcium pump SERCA is an attractive target for discovery of, and/or developing small-molecule effectors for the treatment of heart disease and potentially numerous other degenerative disorders. The inter-molecular FRET sensor, called two-color SERCA, was used to thoroughly evaluate the lifetime and spectral recording fluorescence plate readers.

The combination of both spectral and lifetime fluorescence recording methods creates a novel screening platform offering the advantages of both methods. Lifetime-based screening offers high-precision measurements, which are not dependent on the intensity of the signal. Lifetime data can resolve the amount of different fluorescence species emitted from the same fluorophore. Spectral-based screening offers increased precision due to the resolution across the fluorescence spectrum. Spectral data can resolve the amount of different fluorescence species emitted across the full emission spectrum, including inelastic light scatter from the water Raman signal. This information can be used to determine the amount of material in each well, background signal from fluorescence sources such as cellular autofluorescence, or artifacts from fluorescent small-molecules. When these methods are combined for HTS, it creates a novel platform where incredibly precise and fast measurements from the emission spectrum and the nanosecond decay rate can be coupled and compared.

New high-throughput screening analysis methods were also developed throughout these studies. The similarity index flagged potential fluorescent compounds, and spectral

unmixing analysis was used to decompose the fluorescent emission spectra, in order to determine FRET efficiency from the two-color SERCA biosensor. High-throughput screening with live-cells FRET biosensors surpasses other fluorescence screening methods based on spectral emission recording technology, in terms of precision, speed of acquisition, data quality (resolution), and flexibility of fluorescence chromophores (continuous-wave tunable lasers). It was also possible to determine the relative amounts of fluorescent signal from a particular fluorescence source in comparison to the total signal.

The spectral unmixing methods requires basis spectrum of pure components. Determination of GFP, RFP, cellular autofluorescence, and water Raman spectrum was essential for the proof-of-concept of spectral unmixing methods for the 2CS FRET biosensor. FRET efficiency determination from both spectral and lifetime methods, allowed for calibration of spectrometer sensitivity across wavelengths, and determination of the correction factor. Direct comparison using the FRET efficiency, directly showed increased precision from spectral mode in comparison to lifetime mode.

The research and developments presented here, will result in continued exploration of the technology, drug screening methods, and other therapeutic drug targets in the Thomas lab.

Future directions

In the immediate future, two manuscripts are currently being prepared for publication. The first paper will utilize transient-time resolved FRET technology to determine the structural kinetics of SERCA. FRET changes from the 2CS biosensor are currently being evaluated on the ms time-scale, using rapid-mixing stopped-flow studies.

These studies have already recapitulated the original intrinsic fluorescence studies, showing that calcium-binding occurs sequentially and is coupled to a slow structural transition of SERCA's cytoplasmic headpiece [30]. Future work,will explore the structural kinetics and rate dependent steps of SERCA's structural transition throughout the E1-E2 enzymatic cycle. This work will reveal more specifically how calcium and ATP alter SERCA's structure, and will also be used to test novel SERCA activators, discovered from ongoing large-scale drug screens.

The second paper will continue to expand on the complementary lifetime and spectral unmixing screening strategies. A novel two-channel lifetime plate reader has been developed by Fluorescence Innovations and can simultaneously record the fluorescence lifetime from GFP and RFP emission. The addition of a second RFP channel has been shown to be useful for flagging fluorescent compound interference, analogous to the similarity index for spectral recording methods. Identifying new methods and strategies to remove fluorescence compound interference from screening data is very attractive for large pharmaceutical companies that screen millions of compounds a day, and may be eliminating potential false-positive compounds that may be true hits and lead compounds.

Another emphasis of the planned second publication is to thoroughly evaluate and compare live-cell assays to broken-cell assays. Recent experiments have demonstrated that broken cell assays, using homogenate preparations, allow for fine control of environment surrounding biosensor (e.g. calcium and ATP). Homogenate studies show that 2CS biosensor environment alters the FRET biosensor response to known effectors (e.g. high calcium shows larger effect, whereas low calcium shows no effect). Homogenate

preparations also allow for large-scale preparation of isolated biosensors and growth of cells in suspension culture. This may dramatically reduce the work flow required for live-cell culture. It may also increase prep-to-prep reproducibility because the biosensor samples can be frozen and stored. They may also be less prone to stable clone drift and day-to-day variations in cellular preparations.

Another area of ongoing work is to optimize the current FRET biosensors by generating new constructs with red-shifted fluorescent proteins. It is known that longer-wavelength fluorescent probes are less susceptible to interference from fluorescent compounds [164]. Pilot drug screens have shown that the GFP/RFP pair is significantly less susceptible than CFP/YFP to interference from fluorescent compounds. Orange-red (OFP/RFP) biosensor variants are now being developed. Using a red-shifted donor permits excitation at long wavelengths which decreases the autofluorescence background (thus increasing the dynamic range of the FRET response), and detection at long wavelengths, where interference from fluorescence compounds is at least ten times less than for GFP [164]. The fluorescent properties of red-shifted fluorescent proteins such as the mOrange and mKO variants [165] are suitable for the presented FRET biosensors. Longer lifetimes were found for mKO2 and mKOk, which should improve the sensitivity of FRET detection. The presented data shows that the GFP-RFP biosensor has excellent sensitivity to SERCA effectors, reliably detecting FRET changes as small as 1%, and we expect similar or better performance with the red-shifted FPs.

In collaboration with other members of the Thomas lab, I am currently developing a toolkit FRET biosensors to directly detect interactions between SERCA and its regulatory proteins PLB, DWORF, and SLN. These biosensors will be sensitive to key structural transitions of SERCA under the influence of each endogenous regulator. These biosensors will consist of HEK-expressed human SERCA2a (cardiac muscle isoform) labeled with GFP at the N-terminus (cytosolic side of the membrane), and PLB, DWORF, or SLN labeled with RFP at the N-terminus (also on the cytosolic side of the membrane) (**Figure 44**). FRET will detect regulator binding to SERCA. Each biosensor will be strategically evaluated and optimized using lifetime and spectral-based screening technology. The long term goal is to utilize this arsenal of FRET biosensors for HTS drug discovery and find

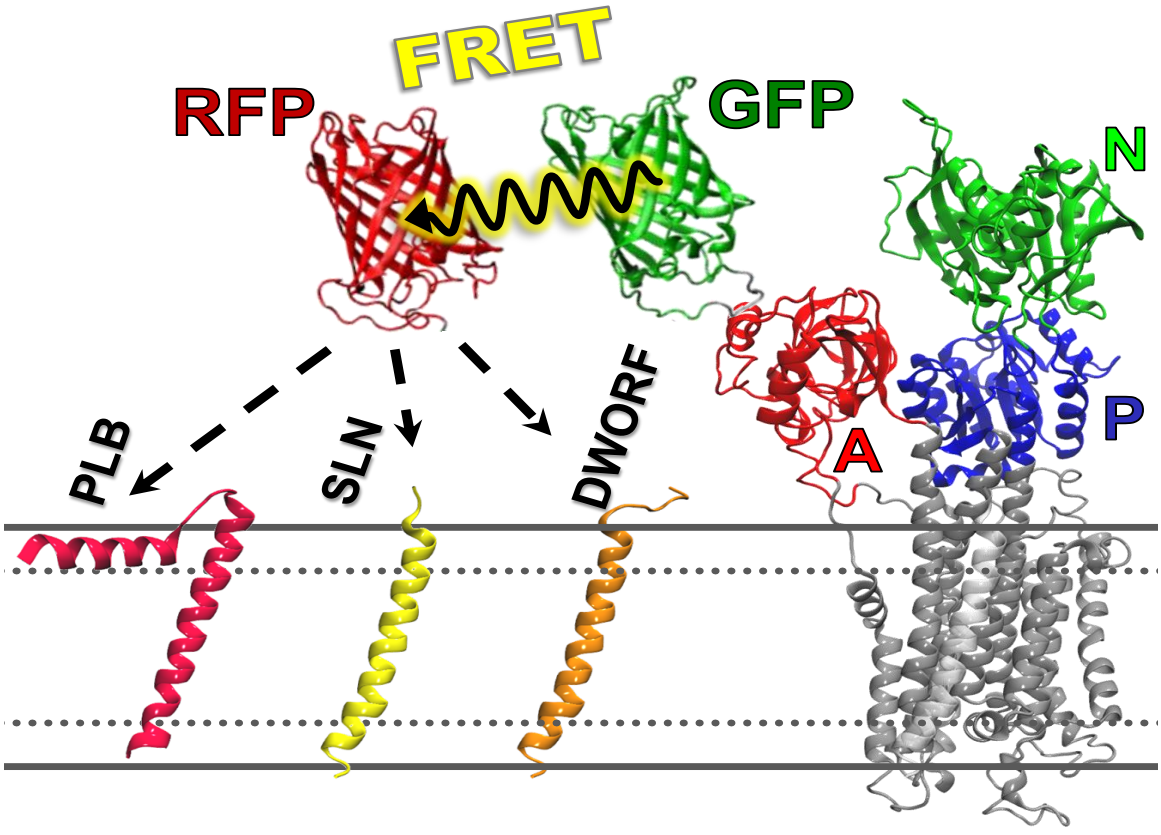

Figure 44 FRET biosensors to detect interaction of SERCA with by regulatory proteins. (PLB, SLN, and DWORF)

compounds with specificity toward one SERCA cardiac-regulator over another. PLB and DWORF are predominately expressed in the ventricles and SLN in the atrium, giving the rational that SERCA's activity can be preferentially targeted and controlled. A key feature of the PLB, DWORF, and SLN- SERCA binding-interface may involve the interaction of the inhibitory polar residues N34 (PLB) and N11 (SLN), as well as the potential activating hydrophobic residue I16 (DWORF).

Many other therapeutic targets, beyond the scope of this thesis work, are also currently under investigation in the Thomas lab, in collaboration with Fluorescence Innovations. The implementation of novel FRET-based biosensors, assays, and fluorescence technology has generated high hopes for the discovery of novel therapeutics for SERCA, as well as, numerous other life-threatening and degenerative diseases, where new treatments are urgently needed.

References:

1. Verkhratsky, A. and V. Parpura, *Calcium signalling and calcium channels: evolution and general principles.* Eur J Pharmacol, 2014. **739**: p. 1-3.
2. Berridge, M.J., P. Lipp, and M.D. Bootman, *The versatility and universality of calcium signalling.* Nat Rev Mol Cell Biol, 2000. **1**(1): p. 11-21.
3. Case, R.M., et al., *Evolution of calcium homeostasis: from birth of the first cell to an omnipresent signalling system.* Cell Calcium, 2007. **42**(4-5): p. 345-50.
4. Orrenius, S., B. Zhivotovsky, and P. Nicotera, *Regulation of cell death: the calcium-apoptosis link.* Nat Rev Mol Cell Biol, 2003. **4**(7): p. 552-65.
5. Berridge, M.J., *Calcium signalling remodelling and disease.* Biochem Soc Trans, 2012. **40**(2): p. 297-309.
6. Berridge, M.J., M.D. Bootman, and H.L. Roderick, *Calcium signalling: dynamics, homeostasis and remodelling.* Nat Rev Mol Cell Biol, 2003. **4**(7): p. 517-29.
7. Krebs, J., L.B. Agellon, and M. Michalak, *Ca(2+) homeostasis and endoplasmic reticulum (ER) stress: An integrated view of calcium signaling.* Biochem Biophys Res Commun, 2015. **460**(1): p. 114-21.
8. Berridge, M.J., *Inositol trisphosphate and calcium signalling mechanisms.* Biochim Biophys Acta, 2009. **1793**(6): p. 933-40.
9. Zalk, R., S.E. Lehnart, and A.R. Marks, *Modulation of the ryanodine receptor and intracellular calcium.* Annu Rev Biochem, 2007. **76**: p. 367-85.
10. Van Petegem, F., *Ryanodine receptors: structure and function.* J Biol Chem, 2012. **287**(38): p. 31624-32.
11. Stammers, A.N., et al., *The regulation of sarco(endo)plasmic reticulum calcium-ATPases (SERCA).* Can J Physiol Pharmacol, 2015. **93**(10): p. 843-54.
12. Gwathmey, J.K., A. Yerevanian, and R.J. Hajjar, *Targeting sarcoplasmic reticulum calcium ATPase by gene therapy.* Hum Gene Ther, 2013. **24**(11): p. 937-47.
13. Pedersen, P.L., *Transport ATPases into the year 2008: a brief overview related to types, structures, functions and roles in health and disease.* J Bioenerg Biomembr, 2007. **39**(5-6): p. 349-55.
14. Szakacs, G., et al., *Targeting multidrug resistance in cancer.* Nat Rev Drug Discov, 2006. **5**(3): p. 219-34.
15. Moller, J.V., et al., *The sarcoplasmic Ca2+-ATPase: design of a perfect chemi-osmotic pump.* Q Rev Biophys, 2010. **43**(4): p. 501-66.
16. de Meis, L. and A.L. Vianna, *Energy interconversion by the Ca2+-dependent ATPase of the sarcoplasmic reticulum.* Annu Rev Biochem, 1979. **48**: p. 275-92.
17. Inesi, G. and L. de Meis, *Regulation of steady state filling in sarcoplasmic reticulum. Roles of back-inhibition, leakage, and slippage of the calcium pump.* J Biol Chem, 1989. **264**(10): p. 5929-36.
18. Toyoshima, C. and G. Inesi, *Structural basis of ion pumping by Ca2+-ATPase of the sarcoplasmic reticulum.* Annu Rev Biochem, 2004. **73**: p. 269-92.
19. Toyoshima, C., et al., *Crystal structures of the calcium pump and sarcolipin in the Mg2+-bound E1 state.* Nature, 2013. **495**(7440): p. 260-4.

20. Jensen, A.M., et al., *Modulatory and catalytic modes of ATP binding by the calcium pump.* EMBO J, 2006. **25**(11): p. 2305-14.
21. Hou, Z., et al., *2-Color calcium pump reveals closure of the cytoplasmic headpiece with calcium binding.* PLoS One, 2012. **7**(7): p. e40369.
22. Winters, D.L., et al., *Interdomain fluorescence resonance energy transfer in SERCA probed by cyan-fluorescent protein fused to the actuator domain.* Biochemistry, 2008. **47**(14): p. 4246-56.
23. Espinoza-Fonseca, L.M. and D.D. Thomas, *Atomic-level characterization of the activation mechanism of SERCA by calcium.* PLoS ONE, 2011. **6**(10): p. e26936.
24. Toyoshima, C. and H. Nomura, *Structural changes in the calcium pump accompanying the dissociation of calcium.* Nature, 2002. **418**(6898): p. 605-11.
25. Traaseth, N.J., et al., *Structure and topology of monomeric phospholamban in lipid membranes determined by a hybrid solution and solid-state NMR approach.* Proc Natl Acad Sci U S A, 2009. **106**(25): p. 10165-70.
26. Zhang, Z., et al., *Detailed characterization of the cooperative mechanism of Ca(2+) binding and catalytic activation in the Ca(2+) transport (SERCA) ATPase.* Biochemistry, 2000. **39**(30): p. 8758-67.
27. Inesi, G., et al., *Concerted conformational effects of Ca2+ and ATP are required for activation of sequential reactions in the Ca2+ ATPase (SERCA) catalytic cycle.* Biochemistry, 2006. **45**(46): p. 13769-78.
28. Inesi, G., et al., *Cooperative calcium binding and ATPase activation in sarcoplasmic reticulum vesicles.* J Biol Chem, 1980. **255**(7): p. 3025-31.
29. Toyoshima, C., *Structural aspects of ion pumping by Ca2+-ATPase of sarcoplasmic reticulum.* Arch Biochem Biophys, 2008. **476**(1): p. 3-11.
30. Inesi, G., *Mechanism of calcium transport.* Annual review of physiology, 1985. **47**: p. 573-601.
31. Fernandez-Belda, F., M. Kurzmack, and G. Inesi, *A comparative study of calcium transients by isotopic tracer, metallochromic indicator, and intrinsic fluorescence in sarcoplasmic reticulum ATPase.* The Journal of biological chemistry, 1984. **259**(15): p. 9687-98.
32. Pegoraro, C., N. Pollet, and A.H. Monsoro-Burq, *Tissue-specific expression of Sarcoplasmic/Endoplasmic Reticulum Calcium ATPases (ATP2A/SERCA) 1, 2, 3 during Xenopus laevis development.* Gene Expr Patterns, 2011. **11**(1-2): p. 122-8.
33. Periasamy, M. and A. Kalyanasundaram, *SERCA pump isoforms: their role in calcium transport and disease.* Muscle Nerve, 2007. **35**(4): p. 430-42.
34. Brini, M. and E. Carafoli, *Calcium pumps in health and disease.* Physiological reviews, 2009. **89**(4): p. 1341-78.
35. Vandecaetsbeek, I., et al., *Structural basis for the high Ca2+ affinity of the ubiquitous SERCA2b Ca2+ pump.* Proc Natl Acad Sci U S A, 2009. **106**(44): p. 18533-8.
36. Dally, S., et al., *Ca2+-ATPases in non-failing and failing heart: evidence for a novel cardiac sarco/endoplasmic reticulum Ca2+-ATPase 2 isoform (SERCA2c).* The Biochemical journal, 2006. **395**(2): p. 249-58.

37. Dode, L., et al., *Dissection of the functional differences between sarco(endo)plasmic reticulum Ca2+-ATPase (SERCA) 1 and 3 isoforms by steady-state and transient kinetic analyses.* J Biol Chem, 2002. **277**(47): p. 45579-91.
38. Bobe, R., et al., *Identification, expression, function, and localization of a novel (sixth) isoform of the human sarco/endoplasmic reticulum Ca2+ATPase 3 gene.* J Biol Chem, 2004. **279**(23): p. 24297-306.
39. Brandl, C.J., et al., *Adult forms of the Ca2+ATPase of sarcoplasmic reticulum. Expression in developing skeletal muscle.* J Biol Chem, 1987. **262**(8): p. 3768-74.
40. Chami, M., et al., *SERCA1 truncated proteins unable to pump calcium reduce the endoplasmic reticulum calcium concentration and induce apoptosis.* J Cell Biol, 2001. **153**(6): p. 1301-14.
41. Dally, S., et al., *Multiple and diverse coexpression, location, and regulation of additional SERCA2 and SERCA3 isoforms in nonfailing and failing human heart.* J Mol Cell Cardiol, 2010. **48**(4): p. 633-44.
42. Greene, A.L., et al., *Overexpression of SERCA2b in the heart leads to an increase in sarcoplasmic reticulum calcium transport function and increased cardiac contractility.* J Biol Chem, 2000. **275**(32): p. 24722-7.
43. Dally, S., et al., *Ca2+-ATPases in non-failing and failing heart: evidence for a novel cardiac sarco/endoplasmic reticulum Ca2+-ATPase 2 isoform (SERCA2c).* Biochem J, 2006. **395**(2): p. 249-58.
44. Aulestia, F.J., et al., *Two distinct calcium pools in the endoplasmic reticulum of HEK-293T cells.* Biochem J, 2011. **435**(1): p. 227-35.
45. Dally, S., et al., *Compartmentalized expression of three novel sarco/endoplasmic reticulum Ca2+ATPase 3 isoforms including the switch to ER stress, SERCA3f, in non-failing and failing human heart.* Cell Calcium, 2009. **45**(2): p. 144-54.
46. Tsien, R.W., *Cyclic AMP and contractile activity in heart.* Advances in cyclic nucleotide research, 1977. **8**: p. 363-420.
47. Bhupathy, P., G.J. Babu, and M. Periasamy, *Sarcolipin and phospholamban as regulators of cardiac sarcoplasmic reticulum Ca2+ ATPase.* Journal of molecular and cellular cardiology, 2007. **42**(5): p. 903-11.
48. Colson, B.A., S.J. Gruber, and D.D. Thomas, *Structural dynamics of muscle protein phosphorylation.* Journal of muscle research and cell motility, 2012. **33**(6): p. 419-29.
49. Babu, G.J., et al., *Overexpression of sarcolipin decreases myocyte contractility and calcium transient.* Cardiovascular research, 2005. **65**(1): p. 177-86.
50. Bhupathy, P., et al., *Threonine-5 at the N-terminus can modulate sarcolipin function in cardiac myocytes.* Journal of molecular and cellular cardiology, 2009. **47**(5): p. 723-9.
51. Bal, N.C., et al., *Sarcolipin is a newly identified regulator of muscle-based thermogenesis in mammals.* Nature medicine, 2012. **18**(10): p. 1575-9.
52. Autry, J.M., D.D. Thomas, and L.M. Espinoza-Fonseca, *Sarcolipin Promotes Uncoupling of the SERCA Ca2+ Pump by Inducing a Structural Rearrangement in the Energy-Transduction Domain.* Biochemistry, 2016. **55**(44): p. 6083-6086.

53. Zsebo, K., et al., *Long-term effects of AAV1/SERCA2a gene transfer in patients with severe heart failure: analysis of recurrent cardiovascular events and mortality.* Circulation research, 2014. **114**(1): p. 101-8.
54. Kang, S., et al., *Small Molecular Allosteric Activator of the Sarco/Endoplasmic Reticulum Ca2+-ATPase (SERCA) Attenuates Diabetes and Metabolic Disorders.* The Journal of biological chemistry, 2015.
55. Nelson, B.R., et al., *A peptide encoded by a transcript annotated as long noncoding RNA enhances SERCA activity in muscle.* Science, 2016. **351**(6270): p. 271-5.
56. Anderson, D.M., et al., *Widespread control of calcium signaling by a family of SERCA-inhibiting micropeptides.* Science signaling, 2016. **9**(457): p. ra119.
57. Lipskaia, L., et al., *Benefit of SERCA2a gene transfer to vascular endothelial and smooth muscle cells: a new aspect in therapy of cardiovascular diseases.* Current vascular pharmacology, 2013. **11**(4): p. 465-79.
58. Greenberg, B., et al., *Prevalence of AAV1 neutralizing antibodies and consequences for a clinical trial of gene transfer for advanced heart failure.* Gene therapy, 2015.
59. Hulot, J.S., K. Ishikawa, and R.J. Hajjar, *Gene therapy for the treatment of heart failure: promise postponed.* European heart journal, 2016. **37**(21): p. 1651-8.
60. Karakikes, I., et al., *Correction of human phospholamban R14del mutation associated with cardiomyopathy using targeted nucleases and combination therapy.* Nature communications, 2015. **6**: p. 6955.
61. Cornea, R.L., et al., *High-throughput FRET assay yields allosteric SERCA activators.* J Biomol Screen, 2013. **18**(1): p. 97-107.
62. Green, K.N., et al., *SERCA pump activity is physiologically regulated by presenilin and regulates amyloid beta production.* The Journal of cell biology, 2008. **181**(7): p. 1107-16.
63. Kono, T., et al., *PPAR-gamma activation restores pancreatic islet SERCA2 levels and prevents beta-cell dysfunction under conditions of hyperglycemic and cytokine stress.* Mol Endocrinol, 2012. **26**(2): p. 257-71.
64. Minamisawa, S., *Enhancement of calcium uptake via the sarcoplasmic reticulum is a potent therapeutic strategy for dilated cardiomyopathy and heart failure.* Expert Opinion on Therapeutic Patents, 2000. **10**(11): p. 1693-1701.
65. Rishi, A.K., et al., *Gene amplification and transcriptional upregulation of the sarco/endoplasmic reticulum Ca2+ transport ATPase in thapsigargin-resistant hamster smooth muscle cells.* Nucleic Acids Research, 1998. **26**(19): p. 4529-4537.
66. Klein, I. and K. Ojamaa, *Thyroid hormone and the cardiovascular system.* N Engl J Med, 2001. **344**(7): p. 501-9.
67. Fadel, B.M., et al., *Hyperthyroid heart disease.* Clin Cardiol, 2000. **23**(6): p. 402-8.
68. Portman, M.A., et al., *Triiodothyronine Supplementation in Infants and Children Undergoing Cardiopulmonary Bypass (TRICC): a multicenter placebo-controlled randomized trial: age analysis.* Circulation, 2010. **122**(11 Suppl): p. S224-33.

69. Pugh, C.W. and P.J. Ratcliffe, *Regulation of angiogenesis by hypoxia: role of the HIF system.* Nat Med, 2003. **9**(6): p. 677-84.
70. Giacomello, M., et al., *Reduction of Ca2+ stores and capacitative Ca2+ entry is associated with the familial Alzheimer's disease presenilin-2 T122R mutation and anticipates the onset of dementia.* Neurobiol Dis, 2005. **18**(3): p. 638-48.
71. Dror, V., et al., *Glucose and endoplasmic reticulum calcium channels regulate HIF-1beta via presenilin in pancreatic beta-cells.* J Biol Chem, 2008. **283**(15): p. 9909-16.
72. Berger, J. and D.E. Moller, *The mechanisms of action of PPARs.* Annu Rev Med, 2002. **53**: p. 409-35.
73. Gillies, P.S. and C.J. Dunn, *Pioglitazone.* Drugs, 2000. **60**(2): p. 333-43; discussion 344-5.
74. Yau, H., et al., *The Future of Thiazolidinedione Therapy in the Management of Type 2 Diabetes Mellitus.* Curr Diab Rep, 2013.
75. Kistamas, K., et al., *Effects of pioglitazone on cardiac ion currents and action potential morphology in canine ventricular myocytes.* Eur J Pharmacol, 2013.
76. Ablorh, N.A., et al., *Accurate quantitation of phospholamban phosphorylation by immunoblot.* Anal Biochem, 2012. **425**(1): p. 68-75.
77. Vandecaetsbeek, I., et al., *Factors controlling the activity of the SERCA2a pump in the normal and failing heart.* Biofactors, 2009. **35**(6): p. 484-99.
78. Sathish, V., et al., *Effect of proinflammatory cytokines on regulation of sarcoplasmic reticulum Ca2+ reuptake in human airway smooth muscle.* Am J Physiol Lung Cell Mol Physiol, 2009. **297**(1): p. L26-34.
79. Sathish, V., et al., *Brain-derived neurotrophic factor in cigarette smoke-induced airway hyperreactivity.* Am J Respir Cell Mol Biol, 2013. **48**(4): p. 431-8.
80. Lampe, P.D., et al., *Phosphorylation of connexin43 on serine368 by protein kinase C regulates gap junctional communication.* J Cell Biol, 2000. **149**(7): p. 1503-12.
81. Prasad, A.M. and G. Inesi, *Regulation and rate limiting mechanisms of Ca2+ ATPase (SERCA2) expression in cardiac myocytes.* Molecular and Cellular Biochemistry, 2012. **361**(1-2): p. 85-96.
82. Wink, D.A., et al., *DNA deaminating ability and genotoxicity of nitric oxide and its progenitors.* Science, 1991. **254**(5034): p. 1001-3.
83. Schulman, I.H. and J.M. Hare, *Regulation of cardiovascular cellular processes by S-nitrosylation.* Biochimica Et Biophysica Acta-General Subjects, 2012. **1820**(6): p. 752-762.
84. Zimmet, J.M. and J.M. Hare, *Nitroso-redox interactions in the cardiovascular system.* Circulation, 2006. **114**(14): p. 1531-44.
85. Wootton, L.L. and F. Michelangeli, *The effects of the phenylalanine 256 to valine mutation on the sensitivity of sarcoplasmic/endoplasmic reticulum Ca2+ ATPase (SERCA) Ca2+ pump isoforms 1, 2, and 3 to thapsigargin and other inhibitors.* J Biol Chem, 2006. **281**(11): p. 6970-6.

86. Tzivoni, D., et al., *Effect of caldaret on the incidence of severe left ventricular dysfunction in patients with ST-elevation myocardial infarction undergoing primary coronary intervention.* Am J Cardiol, 2009. **103**(1): p. 1-4.
87. Starling, A.P., J.M. East, and A.G. Lee, *Stimulation of the Ca(2+)-ATPase of sarcoplasmic reticulum by disulfiram.* Biochem J, 1996. **320 (Pt 1)**: p. 101-5.
88. 2009.
89. Antipenko, A.Y., A.I. Spielman, and M.A. Kirchberger, *Interactions of 6-gingerol and ellagic acid with the cardiac sarcoplasmic reticulum Ca2+-ATPase.* J Pharmacol Exp Ther, 1999. **290**(1): p. 227-34.
90. Namekata, I., et al., *Ellagic acid and gingerol, activators of the sarco-endoplasmic reticulum Ca(2+)-ATPase, ameliorate diabetes mellitus-induced diastolic dysfunction in isolated murine ventricular myocardia.* Eur J Pharmacol, 2013. **706**(1-3): p. 48-55.
91. Lee, S.H., M. Cekanova, and S.J. Baek, *Multiple mechanisms are involved in 6-gingerol-induced cell growth arrest and apoptosis in human colorectal cancer cells.* Mol Carcinog, 2008. **47**(3): p. 197-208.
92. Mandadi, S. and B.D. Roufogalis, *ThermoTRP channels in nociceptors: taking a lead from capsaicin receptor TRPV1.* Curr Neuropharmacol, 2008. **6**(1): p. 21-38.
93. Khairy, H., et al., *Actions of ethanolamine on cultured sensory neurones from neonatal rats.* Neurosci Lett, 2010. **468**(3): p. 326-9.
94. Neumann, J.T. and J.A. Copello, *Cross-reactivity of ryanodine receptors with plasma membrane ion channel modulators.* Mol Pharmacol, 2011. **80**(3): p. 509-17.
95. Mahmmoud, Y.A. and M. Gaster, *Uncoupling of sarcoplasmic reticulum Ca(2)(+)-ATPase by N-arachidonoyl dopamine. Members of the endocannabinoid family as thermogenic drugs.* Br J Pharmacol, 2012. **166**(7): p. 2060-9.
96. Satoh, N., et al., *Lusitropic effect of MCC-135 is associated with improvement of sarcoplasmic reticulum function in ventricular muscles of rats with diabetic cardiomyopathy.* J Pharmacol Exp Ther, 2001. **298**(3): p. 1161-6.
97. Bar, F.W., et al., *Results of the first clinical study of adjunctive CAldaret (MCC-135) in patients undergoing primary percutaneous coronary intervention for ST-Elevation Myocardial Infarction: the randomized multicentre CASTEMI study.* Eur Heart J, 2006. **27**(21): p. 2516-23.
98. Aditya, S. and A. Rattan, *Istaroxime: A rising star in acute heart failure.* J Pharmacol Pharmacother, 2012. **3**(4): p. 353-5.
99. Cully, M., *The dangers of digoxin in AF.* Nat Rev Cardiol, 2013. **10**(2): p. 61.
100. Micheletti, R., et al., *Istaroxime, a stimulator of sarcoplasmic reticulum calcium adenosine triphosphatase isoform 2a activity, as a novel therapeutic approach to heart failure.* Am J Cardiol, 2007. **99**(2A): p. 24A-32A.
101. Farmakis, D. and G. Filippatos, *Istaroxime: is the remedy better than the disease?: Editorial to: "Chronic istaroxine improves cardiac function and heart rate variability in cardiomyopathic hamsters" by Pietro Lo Giudice et al.* Cardiovasc Drugs Ther, 2011. **25**(2): p. 115-7.

102. Chen, Y., et al., *Constitutive cardiac overexpression of sarcoplasmic/endoplasmic reticulum Ca2+-ATPase delays myocardial failure after myocardial infarction in rats at a cost of increased acute arrhythmias.* Circulation, 2004. **109**(15): p. 1898-903.
103. Alemanni, M., et al., *Role and mechanism of subcellular Ca2+ distribution in the action of two inotropic agents with different toxicity.* J Mol Cell Cardiol, 2011. **50**(5): p. 910-8.
104. Luciani, P., M. Fevre, and J.C. Leroux, *Development and physico-chemical characterization of a liposomal formulation of istaroxime.* Eur J Pharm Biopharm, 2011. **79**(2): p. 285-93.
105. Gobbini, M., et al., *Novel analogues of Istaroxime, a potent inhibitor of Na(+),K(+)-ATPase: Synthesis, structure-activity relationship and 3D-quantitative structure-activity relationship of derivatives at position 6 on the androstane scaffold.* Bioorg Med Chem, 2010. **18**(12): p. 4275-99.
106. Jessup, M., et al., *Calcium Upregulation by Percutaneous Administration of Gene Therapy in Cardiac Disease (CUPID): a phase 2 trial of intracoronary gene therapy of sarcoplasmic reticulum Ca2+-ATPase in patients with advanced heart failure.* Circulation, 2011. **124**(3): p. 304-13.
107. Lakowicz, J., *Principles of Fluorescence Spectroscopy, 3rd ed.* Springer2006.
108. Prasher, D.C., et al., *Primary structure of the Aequorea victoria green-fluorescent protein.* Gene, 1992. **111**(2): p. 229-33.
109. Gross, L.A., et al., *The structure of the chromophore within DsRed, a red fluorescent protein from coral.* Proceedings of the National Academy of Sciences of the United States of America, 2000. **97**(22): p. 11990-5.
110. Cranfill, P.J., et al., *Quantitative assessment of fluorescent proteins.* Nature methods, 2016. **13**(7): p. 557-62.
111. Davidson, R.N.D.a.M.W., *Aequorea victoria Fluorescent Proteins.* Carl Zeiss Microscopy Online Campus 2016.
112. Hou, Z., et al., *Two-color calcium pump reveals closure of the cytoplasmic headpiece with calcium binding.* PLoS ONE, 2012: p. accepted.
113. Pallikkuth, S., et al., *Phosphorylated Phospholamban Stabilizes a Compact Conformation of the Cardiac Calcium-ATPase.* Biophys J, 2013. **105**(8): p. 1812-21.
114. Gruber, S.J., et al., *Discovery of enzyme modulators via high-throughput time-resolved FRET in living cells.* J Biomol Screen, 2014. **19**(2): p. 215-22.
115. Shcherbo, D., et al., *Practical and reliable FRET/FLIM pair of fluorescent proteins.* BMC biotechnology, 2009. **9**: p. 24.
116. Petersen, K.J., et al., *Fluorescence lifetime plate reader: resolution and precision meet high-throughput.* Rev Sci Instrum, 2014. **85**(11): p. 113101.
117. Iram, S.H., et al., *ATP-Binding Cassette Transporter Structure Changes Detected by Intramolecular Fluorescence Energy Transfer for High-Throughput Screening.* Molecular pharmacology, 2015. **88**(1): p. 84-94.
118. Muretta, J.M., et al., *High-performance time-resolved fluorescence by direct waveform recording.* Rev Sci Instrum, 2010. **81**(10): p. 103101.

119. Guzman, C., C. Oetken-Lindholm, and D. Abankwa, *Automated High-Throughput Fluorescence Lifetime Imaging Microscopy to Detect Protein-Protein Interactions.* Journal of laboratory automation, 2015.
120. Suzuki, M., et al., *A high-throughput direct fluorescence resonance energy transfer-based assay for analyzing apoptotic proteases using flow cytometry and fluorescence lifetime measurements.* Analytical biochemistry, 2015. **491**: p. 10-7.
121. Suhling, K., et al., *Imaging the environment of green fluorescent protein.* Biophys J, 2002. **83**(6): p. 3589-95.
122. Leavesley, S.J., et al., *Assessing FRET using spectral techniques.* Cytometry. Part A : the journal of the International Society for Analytical Cytology, 2013. **83**(10): p. 898-912.
123. Thorn, T.L.a.K. *Fluorescent protein properties*. 2015; Available from: http://nic.ucsf.edu/FPvisualization/.
124. Wootton, L.L. and F. Michelangeli, *The effects of the phenylalanine 256 to valine mutation on the sensitivity of sarcoplasmic/endoplasmic reticulum Ca2+ ATPase (SERCA) Ca2+ pump isoforms 1, 2, and 3 to thapsigargin and other inhibitors.* The Journal of biological chemistry, 2006. **281**(11): p. 6970-6.
125. Michelangeli, F. and J.M. East, *A diversity of SERCA Ca2+ pump inhibitors.* Biochemical Society transactions, 2011. **39**(3): p. 789-97.
126. Palmer, A.E., et al., *Design and application of genetically encoded biosensors.* Trends in biotechnology, 2011. **29**(3): p. 144-52.
127. Zhang, J.H., T.D. Chung, and K.R. Oldenburg, *A Simple Statistical Parameter for Use in Evaluation and Validation of High Throughput Screening Assays.* J Biomol Screen, 1999. **4**(2): p. 67-73.
128. Lam, A.J., et al., *Improving FRET dynamic range with bright green and red fluorescent proteins.* Nature methods, 2012. **9**(10): p. 1005-12.
129. Addgene. *Fluorescent Protein Guide: Biosensors*. 2015; The nonprofit plasmid repository]. Available from: https://www.addgene.org/fluorescent-proteins/biosensors/.
130. Koushik, S.V., et al., *Cerulean, Venus, and VenusY67C FRET reference standards.* Biophysical Journal, 2006. **91**(12): p. L99-L101.
131. Palmer, A.E. and R.Y. Tsien, *Measuring calcium signaling using genetically targetable fluorescent indicators.* Nature protocols, 2006. **1**(3): p. 1057-65.
132. Palmer, A.E., et al., *Bcl-2-mediated alterations in endoplasmic reticulum Ca2+ analyzed with an improved genetically encoded fluorescent sensor.* Proceedings of the National Academy of Sciences of the United States of America, 2004. **101**(50): p. 17404-9.
133. Scientific, H., *Signal to Noise Ratio Explained.* 2015.
134. Thomsen, V., D. Schatzlein, and D. Mercuro, *Limits of detection in spectroscopy.* Spectroscopy, 2003. **18**(12): p. 112-114.
135. Zhang, L., et al., *Spectral wide-field microscopic fluorescence resonance energy transfer imaging in live cells.* Journal of biomedical optics, 2015. **20**(8): p. 86011.

136. Larson, J.M., *The Nikon C1si combines high spectral resolution, high sensitivity, and high acquisition speed.* Cytometry. Part A : the journal of the International Society for Analytical Cytology, 2006. **69**(8): p. 825-34.
137. Mustafa, S., et al., *Quantitative Forster resonance energy transfer efficiency measurements using simultaneous spectral unmixing of excitation and emission spectra.* Journal of biomedical optics, 2013. **18**(2): p. 26024.
138. Schaaf, T.M., et al., *High-Throughput Spectral and Lifetime-Based FRET Screening in Living Cells to Identify Small-Molecule Effectors of SERCA.* Journal of biomolecular screening, 2016.
139. Li, J., et al., *Structural and functional dynamics of an integral membrane protein complex modulated by lipid headgroup charge.* Journal of molecular biology, 2012. **418**(5): p. 379-89.
140. Dong, X. and D.D. Thomas, *Time-resolved FRET reveals the structural mechanism of SERCA-PLB regulation.* Biochemical and biophysical research communications, 2014. **449**(2): p. 196-201.
141. Meijer, M., et al., *Comparison of plate reader-based methods with fluorescence microscopy for measurements of intracellular calcium levels for the assessment of in vitro neurotoxicity.* Neurotoxicology, 2014. **45**: p. 31-7.
142. Honarnejad, K., et al., *FRET-based calcium imaging: a tool for high-throughput/content phenotypic drug screening in Alzheimer disease.* Journal of biomolecular screening, 2013. **18**(10): p. 1309-20.
143. Ogikubo, S., et al., *Intracellular pH sensing using autofluorescence lifetime microscopy.* J Phys Chem B, 2011. **115**(34): p. 10385-90.
144. Avezov, E., et al., *Lifetime imaging of a fluorescent protein sensor reveals surprising stability of ER thiol redox.* J Cell Biol, 2013. **201**(2): p. 337-49.
145. Bleeker, N.P., et al., *A Novel SERCA Inhibitor Demonstrates Synergy with Classic SERCA Inhibitors and Targets Multidrug-Resistant AML.* Mol Pharm, 2013.
146. Lockamy, E.L., et al., *Functional and physical competition between phospholamban and its mutants provides insight into the molecular mechanism of gene therapy for heart failure.* Biochemical and biophysical research communications, 2011.
147. Ha, K.N., et al., *Controlling the Inhibition of the Sarcoplasmic Ca2+-ATPase by Tuning Phospholamban Structural Dynamics.* The Journal of biological chemistry, 2007. **282**(51): p. 37205-14.
148. Gruber, S.J., S. Haydon, and D.D. Thomas, *Phospholamban mutants compete with wild type for SERCA binding in living cells.* Biochemical and biophysical research communications, 2012. **420**(2): p. 236-40.
149. Smolin, N. and S.L. Robia, *A structural mechanism for calcium transporter headpiece closure.* J Phys Chem B, 2015. **119**(4): p. 1407-15.
150. Schaaf, T.M., et al., *Spectral Unmixing Plate Reader: High-Throughput, High-Precision FRET Assays in Living Cells.* Journal of biomolecular screening, 2016.

151. Muretta, J.M., et al., *The structural kinetics of switch-1 and the neck linker explain the functions of kinesin-1 and Eg5.* Proceedings of the National Academy of Sciences of the United States of America, 2015. **112**(48): p. E6606-13.
152. Muretta, J.M., et al., *Direct real-time detection of the structural and biochemical events in the myosin power stroke.* Proceedings of the National Academy of Sciences of the United States of America, 2015. **112**(46): p. 14272-7.
153. Li, J., et al., *Structural and functional dynamics of an integral membrane protein complex modulated by lipid headgroup charge.* J Mol Biol, 2012. **418**(5): p. 379-89.
154. Mueller, B., et al., *Direct detection of phospholamban and sarcoplasmic reticulum Ca-ATPase interaction in membranes using fluorescence resonance energy transfer.* Biochemistry, 2004. **43**(27): p. 8754-65.
155. Rogers, T.B., et al., *Use of thapsigargin to study Ca2+ homeostasis in cardiac cells.* Bioscience reports, 1995. **15**(5): p. 341-9.
156. Bartolommei, G., et al., *Clotrimazole inhibits the Ca2+-ATPase (SERCA) by interfering with Ca2+ binding and favoring the E2 conformation.* The Journal of biological chemistry, 2006. **281**(14): p. 9547-51.
157. Cherednichenko, G., et al., *Triclosan impairs excitation-contraction coupling and Ca2+ dynamics in striated muscle.* Proceedings of the National Academy of Sciences of the United States of America, 2012. **109**(35): p. 14158-63.
158. Seidler, J., et al., *Identification and prediction of promiscuous aggregating inhibitors among known drugs.* Journal of medicinal chemistry, 2003. **46**(21): p. 4477-86.
159. Guzman, C., C. Oetken-Lindholm, and D. Abankwa, *Automated High-Throughput Fluorescence Lifetime Imaging Microscopy to Detect Protein-Protein Interactions.* Journal of laboratory automation, 2016. **21**(2): p. 238-45.
160. Svensson, B., et al., *FRET-based trilateration of probes bound within functional ryanodine receptors.* Biophys J, 2014. **107**(9): p. 2037-48.
161. Colson, B.A., et al., *Site-directed spectroscopy of cardiac myosin-binding protein C reveals effects of phosphorylation on protein structural dynamics.* Proceedings of the National Academy of Sciences of the United States of America, 2016. **113**(12): p. 3233-8.
162. Iram, S.H., et al., *ATP-Binding Cassette Transporter Structure Changes Detected by Intramolecular Fluorescence Energy Transfer for High-Throughput Screening.* Mol Pharmacol, 2015. **88**(1): p. 84-94.
163. Lewis, A.K., et al., *Open and closed conformations of the isolated transmembrane domain of death receptor 5 support a new model of activation.* Biophys J, 2014. **106**(6): p. L21-4.
164. Simeonov, A., et al., *Fluorescence spectroscopic profiling of compound libraries.* J Med Chem, 2008. **51**(8): p. 2363-71.
165. Piatkevich, K.D. and V.V. Verkhusha, *Guide to red fluorescent proteins and biosensors for flow cytometry.* Methods in cell biology, 2011. **102**: p. 431-61.